2021-04-14

Investigation of Gas Adsorption in Shale Reservoir

Yu, Xinran

UNIVERSITY OF CALGARY

Investigation of Gas Adsorption in Shale Reservoirs

by

Xinran Yu

A THESIS

SUBMITTED TO THE FACULTY OF GRADUATE STUDIES

IN PARTIAL FULFILMENT OF THE REQUIREMENTS FOR THE

DEGREE OF DOCTOR OF PHILOSOPHY

GRADUATE PROGRAM IN CHEMICAL AND PETROLEUM ENGINEERING

CALGARY, ALBERTA

APRIL, 2021

Abstract

Unlike conventional reservoirs, there is a considerable amount of gas stored as an adsorbed phase in most shale reservoirs in North America. Injection of CO_2 into shale formations is found to be a promising method for extraction of hydrocarbons and CO_2 can be also stored as an adsorbed phase in shale reservoirs, which can mitigate the global warming issue. Therefore, it is necessary to understand rock wettability and water contact angles of shale reservoirs under reservoir conditions and obtain accurate adsorption isotherms for estimation of the total gas-in-place (GIP), and determination of the proportions of free gas and adsorbed gas, which can help understand gas transport behavior and predict gas production from shale reservoirs. In this thesis, we present an investigation of water/brine contact angles as functions of temperature, pressure, salinity, ion types, and gas contents by Molecular Dynamics (MD) simulations. It is found that temperature has profound effects on water contact angles below a critical temperature at an intermediate pressure and a CO_2-water-shale organic matter system turns from a neutrally-wet state to a CO_2-wet state at the critical pressure of CO_2. Only a slight increase in water contact angles is observed with increasing salinity, and an increase in the CO_2 fraction of gas mixtures can increase water contact angles at the same pressure and temperature. Moreover, we use Grand Canonical Monte Carlo (GCMC) simulation to investigate suitable experimental conditions to obtain an accurate void volume of pores by helium expansion tests and provide a method that can be used to obtain an adsorbate-based pore volume for estimation of adsorption isotherms. Considering an economic effect and measurement accuracy, determining a void volume by helium expansion tests within a moderate pressure range at 500 K is suggested. Additionally, by using a CH_4-based volume for calculating excess adsorption amounts, a negative excess adsorption amount of methane at high

pressure is not observed. Kerogen swelling in shale formations can be induced by gas adsorption, which further results in changes in pore volumes and influences determination of adsorption isotherms. Gas adsorption in kerogen and the corresponding sorption-induced swelling are also investigated by hybrid GCMC/MD simulations in this thesis. A unified relationship between volumetric strain and an absolute adsorption amount is developed for different adsorbates and a theoretical model for calculating excess adsorption isotherms coupling swelling is also proposed. Excess adsorption isotherms generated by our model are consistent with excess adsorption data calculated by a variable pore volume, which shows a large discrepancy compared to that determined using constant volumes, especially at high pressures.

Acknowledgement

I would like to express my deepest gratitude to my supervisor, Dr. Zhangxing (John) Chen, who gave me encouragement and supervision in the Department of Chemical and Petroleum Engineering at the University of Calgary. I also want to thank Dr. Jing Li and Dr. Keliu Wu for their patience, advice and supervision during my Ph.D. study. Without their excellent guidance, technical discussions, paper revisions, and great patience, I could not complete my research work and thesis on time.

I also would like to thank the supervisory committee: Dr. Hemanta Sarma, Dr. Hassan Hassanzadeh, from Department of Chemical and Petroleum Engineering, Dr. Robert Marroitt from Department of Chemistry at the University of Calgary and Dr. Jingen Deng from the China University of Petroleum in Beijing for serving on my candidacy and dissertation committees.

Moreover, I want to appreciate all our group members in the Reservoir Simulation Group in the Department of Chemical and Petroleum Engineering at the University of Calgary. I am truly grateful to our group members for their open communications and encouragement during my study and life at the University of Calgary. My appreciation is also extended to the Advanced Research Computing (ARC) cluster at the University of Calgary and Compute Canada, which provides me with the platform to run the MD simulations.

I would not come this far with endless love and support from my beloved family members throughout my life - my husband Mr. Linyang Zhang, my parents Mr. Qian Yu and Mrs. Xiaoqing Zhang, and my parents-in-law Mr. Feng’e Zhang and Mrs. Lihua Ji.

Table of Contents

List of Tables

List of Figures

Chapter 1 Introduction

A significant increase in production from unconventional reservoirs has been witnessed in the world energy market recently due to the advanced horizontal drilling and hydraulic fracturing technologies. The great success of shale gas exploration and development in North America has attracted more attention from several countries such as China and India. China, Argentina, Algeria, the USA, and Canada are reported to be the top five countries with technically recoverable shale gas reserves [1]. As reported by Canada's natural gas industry, fifteen potential shale gas formations have been discovered, five of which including Basal Banff/Exshaw, Duvernay, Muskwa, North Nordegg, and Wilrich can contain up to 1,291 trillion cubic feet (TcF) of GIP [2]. CO_2 has been injected into shale formations for extraction of light hydrocarbons such as CH_4 and C_2H_6, and it can be securely stored in these formations, which can further reduce greenhouse gas emissions [3–5]. Therefore, CO_2 sequestration-enhanced gas recovery (CS-EGR) is a promising method that can not only satisfy the growing global energy consumption demands but also mitigate the global warming issue [6,7].

Up to 50% to 60% of the total GIP in several major shale formations in North America is stored in the form of adsorbed gas [8,9]. Therefore, it is important to understand the mechanisms of methane adsorption in shale reservoirs in order to estimate the total GIP of methane and the proportions of the free and adsorbed gas. Furthermore, determination of the proportions of free gas and adsorbed gas is of great significance to understand gas transport behavior and predict gas production from shale reservoirs [10]. The depth of the shale reservoir is generally large, and its pressure and temperature are also high compared to the coalbed reservoir. For the Lower Silurian

and Lower Cambrian shales in the Sichuan Basin, southwest China, the burial depth range of shale formations corresponds to 2000-4000 m [11]. We assume that the hydrostatic pressure gradient is 0.01 MPa/m and the normal geothermal gradient is 3 °C/100 m, sequentially [11]. Therefore, the temperature of shale reservoirs ranges from 60 to 120 °C and the reservoir pressure ranges from 20 to 40 MPa, respectively. Thus, it is necessary to investigate high-pressure or high-temperature methane adsorption [9]. Many scholars use both experimental and simulation approaches to understand the adsorption behavior and obtain adsorption isotherms [12–14]. Unfortunately, a negative excess adsorption phenomenon was found in methane adsorption at high pressure by many scholars: the excess adsorption amount became negative at high pressure, which made the adsorption isotherms lose their physical meaning [14,15]. Wrong estimation of adsorption isotherms results from the use of an improper void volume for isotherms calculations. Therefore, determination of an accurate void volume for adsorbates is of great importance for appropriate adsorption isotherms.

Additionally, gas adsorption can lead to the deformation of a pore structure in shale reservoirs [16–19]. However, the adsorption isotherms in previous studies were calculated by assuming that the pore structure was fixed, and a pore volume was constant. Kerogen swelling happens in experiments and a pore volume is variable during adsorption, which cannot be determined at any moment. Therefore, a fixed pore volume measured by volumetric gas such as helium and argon under certain experimental conditions is used in calculations of an adsorption amount. For molecular simulations, freezing a kerogen structure will ignore the dynamic nature of pores and an interplay between a pore structure and gas molecules, which is not appropriate [20]. Moreover, pore structure deformation can result in high porosity and thus an accessible pore volume can

become larger [16]. Therefore, it is not appropriate to use a constant pore volume to calculate an excess adsorption amount under different conditions and an adsorption amount should be determined coupling the sorption-induced swelling.

This thesis consists of nine chapters. Chapter 1 introduces the research topic, major challenges and research objectives. Chapter 2 reviews important characteristics of shale reservoirs, and mechanisms and models for adsorption. Chapter 3 gives a brief introduction to MD and Monte Carlo methods. In Chapters 4, 5, 6 and 7, four peer-reviewed publications are shown, including investigations of rock wettability of a shale formation and gas adsorption in shale reservoirs using MD simulations. Primary conclusions and recommendations are displayed in Chapter 8.

The major aim of this thesis is to investigate gas adsorption behavior and understand the adsorption mechanisms in shale formations. To achieve this aim, a comprehensive and systematic study is conducted by molecular simulations and a theoretical method. The specific objectives are:

1. To understand interactions between adsorbates (such as CH_4 and CO_2) and shale formations by MD simulations, which can be described by parameters of rock wettability and water contact angles;
2. To investigate suitable experimental conditions to obtain an accurate void volume of pores by helium expansion tests;
3. To provide a method that can be used to obtain an adsorbate-based pore volume for estimation of adsorption isotherms;
4. To investigate adsorption mechanisms in organic pores such as kerogen pores in shales in addition to simple carbon-slit pores coupling the sorption-induced swelling;

5. To develop and validate an adsorption model, which can capture adsorption isotherm characteristics and describe the adsorption behavior in shales.

Chapter 2 Literature review

2.1 Shale gas reservoirs

Shale gas is one of the most important sources of energy supply due to the advanced multistage hydraulic fracturing technologies [21–23]. Shale gas resources are abundant and widely distributed across the world, and the estimated recoverable shale gas resources are up to 7795 Tcf under current technical and economic conditions, which is about one-third of total natural gas resources [24]. **Figure 2.1** shows the shale gas resources around the world.

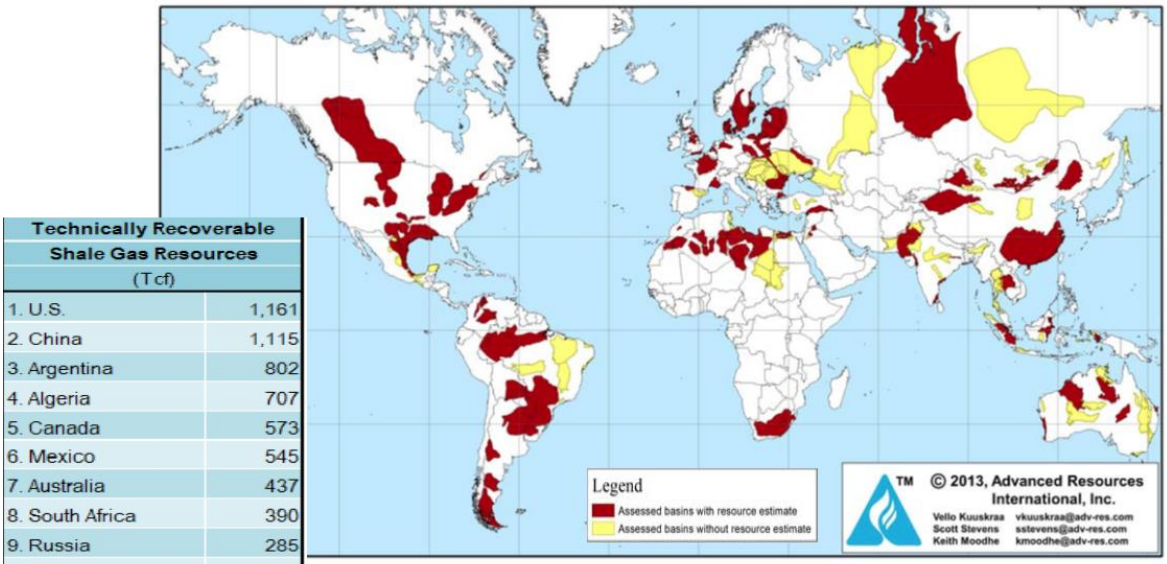

Technically Recoverable Shale Gas Resources (Tcf)	
1. U.S.	1,161
2. China	1,115
3. Argentina	802
4. Algeria	707
5. Canada	573
6. Mexico	545
7. Australia	437
8. South Africa	390
9. Russia	285
10. Brazil	245
11. Others	1,535
TOTAL	7,795

Figure 2. 1 Assessed world shale gas resources [25]**.**

Shale gas reservoirs are different from conventional reservoirs in many aspects, such as their geological location, geological characteristics, and geological framework [26]. Essential elements in the conventional reservoirs include source rock, reservoir rock, seal rock, overburden rock, and

trap formation, which are involved in the process of the generation-migration-accumulation [27]. However, unlike conventional reservoirs, shale rocks act as source rock, trap, and reservoirs in the shale gas reservoir system [28,29].

Shale rocks can be classified into different types based on their different deposition environment. Black shales, as the most common shales in the world, act as source rock in most of the oil and gas reservoirs. The fine particles of organic matter in black deposit with mud and form black shales. For grey shales and red shales, they are containing calcium fraction or minerals, and goethite, respectively [30]. Based on the organic matter content, they can also be divided into light and dark shales. The light shales are always poor in organic fractions, while the dark shales are rich in organic matters [31].

2.1.1 Organic matter

Organic matter, denoted by the total organic carbon (TOC) content, can be used for signifying the organic carbon which can produce hydrocarbon and cannot be transformed into hydrocarbon [32]. Based on the presence of hydrocarbons, TOC contents in a source rock are classified into three types, which are organic carbon reserved in the hydrocarbons, organic carbon that can generate hydrocarbons, and the residual organic part that is unable to produce hydrocarbons [32–34]. The organic matter in shales is mainly composed of kerogen with pores in the nanometer range. Kerogen consists of carbon, hydrogen, oxygen, nitrogen, and smaller amounts of sulphur, in which the amount of hydrogen is a significant factor for the determination of the amount of gas formation [35]. Depending on its composition and type of produced hydrocarbon, kerogen is divided into the following types [36]:

Type I: This type generally consists of the most organic matter rich in hydrogen, which is often structureless alginite. It is commonly generated from lacustrine and marine settings. A large fraction of type I kerogen can be transformed into petroleum thermally, and thus it is rarely regarded as thermally mature or postmature rocks.

Type II: It is predominately generated from marine but not restricted to marine settings. This type of kerogen is composed of the hydrogen-rich maceral exinite and it is slightly less hydrogen-rich compared to type I. Oil and gas can be produced from type II kerogen by continuous heating and maturation.

Type III: The composition of type III kerogen is vitrinite which is a maceral transformed from land plant wood. As with type II kerogen, it is also commonly generated from but not restricted to paralic marine settings. Although this type of kerogen contains sufficient hydrogen, it is gas prone and not enough to be oil-generative.

Besides TOC content and kerogen type, thermal maturity is an important factor for organic content in shales. Three levels of transformation are found in kerogen, including immature stage (diagenesis), mature stage (metagenesis) and post-mature stage (catagenesis). Kerogen is stable and cannot transform at the immature stage. For kerogen at the mature stage, oil and gas can be produced and oil cracking starts occurring. At this stage, oil is initially generated from hydrocarbon. When the post-mature stage is reached, gas is the main product from kerogen and most oil cracking happens. At last, oil trapped in shale gas reservoirs is replaced by gas and over-mature organic matter.

Organic matter in shales provides many advantages for gas adsorption, such as low density, source rocks and varying wettability [13]. The effects of organic matter content on methane adsorption are controversial. Some studies show that methane adsorption capacity on shales is closely associated with the TOC content [37]. Low organic content can result in lower adsorption capacity [38]. However, there are also a few studies reporting that no correlation is found between the TOC content and methane adsorption capacity [39].

2.1.2 Mineral component

Shale rocks are composed of up to 59% of clay minerals including illite, chlorite, smectite and kaolinite, and approximately 40% non-clay minerals including quartz, chert and feldspar [40]. The amounts of clay and non-clay minerals in shales are various, which is dependent on rock types and climate [41]. Pulsed neutron spectroscopy techniques and X-ray diffraction are generally used for the estimation of semi-quantitative mineralogy. For Marcellus shales, the fraction of quartz varies from 40 to 80% and the fraction of clay is approximately 20 to 60% [42]. A higher clay fraction is reported in Bossier shale in some studies [43]. Fine pores, mostly micropores, are detected in clay minerals and these characteristics can help methane adsorption in shales [44,45]. Compared to shales with high non-clay content, the large internal surface area in these shales is of great importance to methane adsorption capacity [46]. However, high clay content in shales always results in low traceability, then leading to low production of shale gas [47,48].

2.1.3 Pore system

The pore system of shales is composed of matrix and fractures, which is more complex than that of conventional reservoirs. In the shale matrix, micropores (< 2 nm) and mesopores (2-50 nm) are prevalently classified by IUPAC. Based on this classification, micropores are divided into super-

micropores (1.4-2.0 nm), micropores (0.7-1.4 nm) and ultra-micropores (<0.7 nm) [49]. **Figure 2.2** shows the pore size distribution of six shale samples from the Longmaxi Formation. It is obvious that the peak radius falls between 1 and 3 nm, indicating that micropores are dominant in shales. In porous natural rocks, micropores of different shapes can be detected, such as slit-type pores, circle-type pores, triangle-type and square-type pores (**Figure 2.3**). Some of these pores are closed and blind, which are difficult to access and preventing fluids from moving through the pores. Additionally, the larger internal surface area in the micropores contributes to gas adsorption and storage in reservoirs. Compared to micropores, macropores and mesopores have a smaller internal surface area but they provide a connected pathway for fluids to flow through micropores and play an important role in establishing pore networks of shale matrix and fracture systems.

Moreover, Loucks et al. classified the pores into interparticle pores, intraparticle pores and organic-matter pores [50]. The interparticle pores are usually between particles and crystals, while intraparticle pores are located within particles. These two kinds of pores belong to the mineral matrix. Organic-matter pores are intraparticle pores located in organic matters [50]. Unlike intraparticle mineral pores, interparticle mineral pores are of great significance in the effective pore network because they are always interconnected. Though organic pores are intraparticle, they are also important parts of an interconnected network due to their interconnectivity.

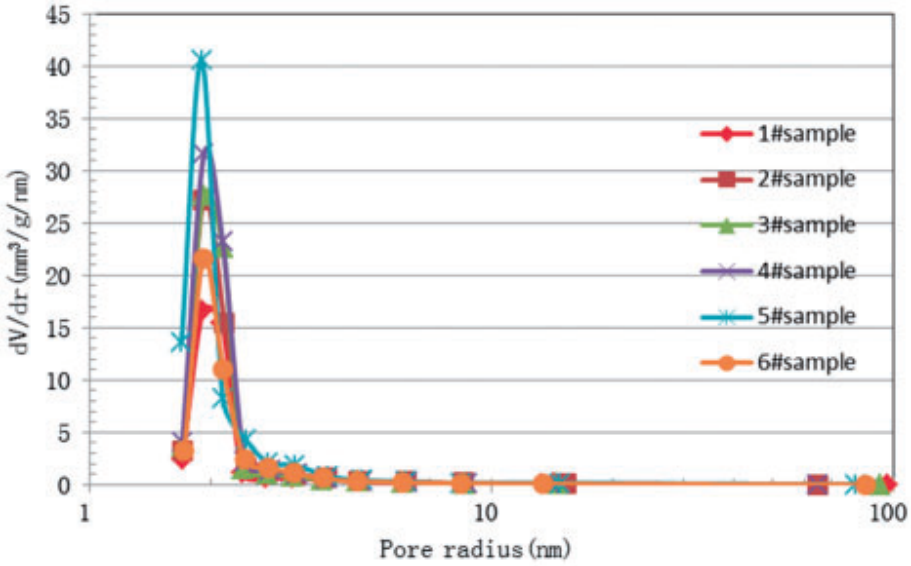

Figure 2. 2 Pore size distribution of six shale samples from the Longmaxi formation [51]**.**

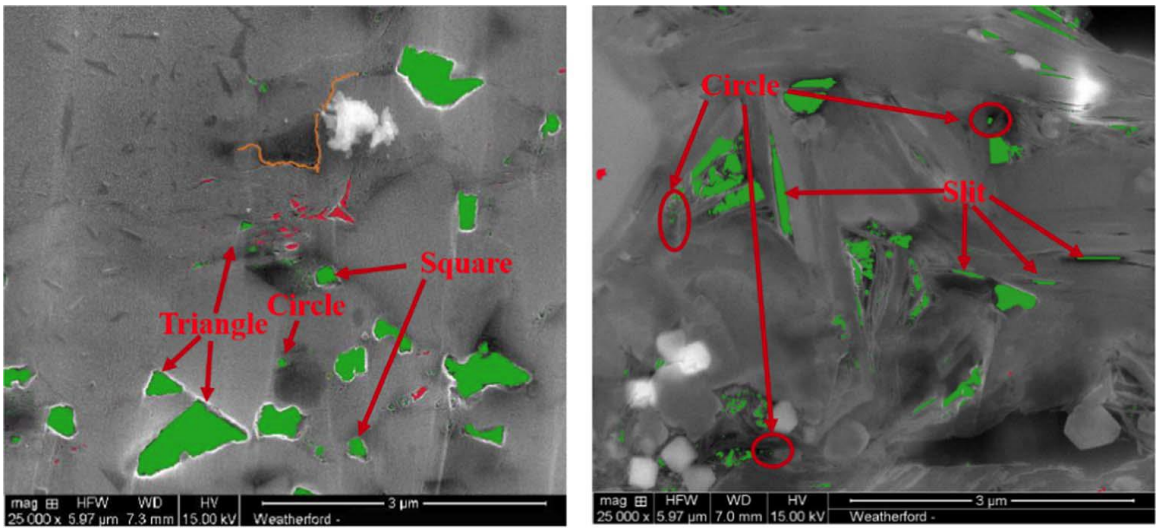

Figure 2. 3 SEM images of shales: (a) Eagle Ford shale, (b) Marcellus shale. Pores in green are organic pores, and pores in red are inorganic pores [52]**.**

2.1.4 Rock wettability and water contact angle

As key parameters describing interactions between CO_2, CH_4, brine, and shale formations in the CS-EGR (CO_2 sequestration-enhanced gas recovery) processes, rock wettability and water contact

angle have a strong influence on the capillary pressure, relative permeability and fluid distribution in shale reservoirs [53–55]. The wettability in a CO_2-brine-shale system was investigated by many scholars [56–58]. The surfaces of inorganic pores in shale were found to be water wet and they can turn to be mixed-wet at higher pressures [56,59]. As expected, Lan et al. reported that organic-rich shales were oil-wet in the environment of hydrocarbons [60]. The brine contact angles on organic shales are also influenced by the total organic carbon (TOC) contents and organic thermal maturity. Higher thermal maturity and TOC contents can contribute to an increasing brine contact angle, and the organic matter becomes more oil-wet as maturity increases [61]. Arif et al. also investigated the effect of TOC contents on the wettability of organic-rich shales, and their results showed that water contact angles increased with TOC contents and a system tended to be CO_2-wet with an ultrahigh TOC content [62]. However, Guiltinan et al. found little variation in the measured contact angle on Barnett shale samples with different TOC contents and thermal maturities, and a shale surface remained water-wet regardless of TOC contents and thermal maturities [63]. Although oil-wet or mixed-wet pores in organic pores of shales cannot constrain the buoyant CO_2 by a capillary force due to spontaneous imbibition of CO_2 [64], it can still store CO_2 through other mechanisms such as sorption [65]. Moreover, the effects of pressure, temperature, salinity, and ion types on CO_2 wettability in organic-rich shale have been investigated by advancing and receding brine contact angle measurements [58], and results displayed that an increase in pressure and salinity or a decrease in temperature can result in a higher brine contact angle.

For CH_4-brine-shale systems, there is limited research about the brine contact angles though it is of great significance to shale gas production [66,67]. Many researchers assumed that a shale surface had a similar wettability in the atmospheres of CO_2 and CH_4 under the reservoir conditions,

and CH_4 was used as an analogy to estimate CO_2 storage capacities [68,69]. This is not strictly true due to differences in chemical and physical properties between CO_2 and CH_4 at both micro- and macro scales. Brine contact angles for CH_4-brine-shale systems were found to be lower compared with those in CO_2-brine-shale systems [58]. Unlike CO_2-brine-shale systems, the brine salinity also has no significant effects on the brine contact angles in CH_4-brine-shale systems. When CO_2 and CH_4 densities are similar to each other, a shale surface was found to have the same wettability in the atmospheres of CO_2 and CH_4 [58,70]. Furthermore, the effects of gas mixtures of CO_2 and CH_4 on shale wettability are still open to answer and there are few studies about this topic. Some scholars measured the interfacial tensions of CH_4/brine or CH_4/water with the presence of CO_2 and their results showed that the interfacial tensions were reduced with an increase in the mole fraction of CO_2 under a fixed experimental condition [71,72]. By adding 20% CH_4, the brine contact angle for a CO_2-brine-silica system was increased by 8% [73]. Therefore, it is of great significance to have a better understanding of the wetting process in the environment of gas mixtures containing CO_2 and CH_4 to aid the prediction of CO_2 storage capacity and the production of shale gas.

2.2 Adsorption

2.2.1 Definition of adsorption

Adsorption can be defined as the adhesion of gas molecules to a solid surface [74–76]. **Figure 2.4** displays the gas adsorption in nano-slits. An adsorbed phase, affected by the potential field of solid walls, is an accumulation of gas molecules on a surface, taking up a certain volume V_a in the pore. The bulk phase in the pore is not affected by the potential field and occupied the rest of the pore volume V_b. The total volume V_t can be written as

$$V_t = V_a + V_b \tag{2.1a}$$

If the amounts of gas in both bulk N_b and adsorbed phase N_a, and the bulk density ρ_b and averaged density of the adsorbed phase ρ_a are known, the total volume of the pore is expressed as below,

$$V_t = {N_a \cdot M}/{\rho_a} + {N_b \cdot M}/{\rho_b} \tag{2.1b}$$

where M is the molar mass of gas. The bulk phase density can be obtained from GCMC simulation at a specific temperature and pressure, NIST database or calculated by the equation of state (EOS).

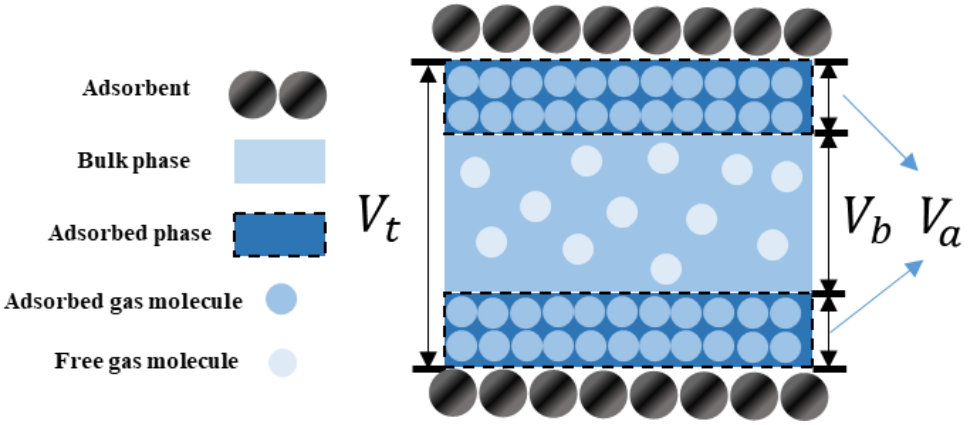

Figure 2. 4 Gas adsorption in a nano-slit.

An absolute adsorption amount is the gas amount within an adsorbed layer that takes up a certain volume. When the pores are extremely small in the structure, the total loading amount of an adsorbent can be regarded as an absolute adsorbed amount. Due to the limitation of the experiment measurement, the volume occupied by the adsorbed phase cannot be determined. By considering an ideal dividing surface without any volume on the basis of the Gibbs assumption, the excess adsorption amount N_e is used for calculating adsorption amount [77]. It is a surface excess amount,

which is calculated by subtracting the amount of gas in the bulk density from the total loading amount N_t:

$$N_e = N_t - {V_t \cdot \rho_b}/{M} \quad (2.2)$$

2.2.2 Adsorption in shales

Due to micro-ultra-micro pore structures and a large internal surface area in shale reservoirs, up to 50% to 60% of the total GIP in several major shale formations in North America is stored in the form of adsorbed gas [8,78,79].

Investigation of gas adsorption in shales has been conducted by many scholars. Organic matter is found to be a key parameter that can contribute to gas adsorption capacity in shales. The parameter of TOC content is reported to be related positively to methane adsorption capacity for shales rich in organic matter [80–83]. However, due to the smectite's contribution, a negative relationship between TOC content and adsorption capacity is also witnessed [39,84]. As addressed before, besides TOC content, thermal maturity, kerogen type are also key parameters that can influence the gas adsorption capacity. Higher adsorption capacities are found in high-mature shales than immature shales, which is due to large amounts of micropores, decreasing heterogeneity and kerogen-induced aromaticity during the process of thermal maturation [13,80,85,86]. Additionally, gas adsorption amount in type III kerogen is reported to be higher than that in type I and II kerogens [13]. Some literature also illustrated that clay minerals also play an important role in gas adsorption for shales rich in clay due to their large inner surface area. Clay minerals, such as illite and montmorillonite can adsorb considerable amounts of gas, and effects of different components on adsorption are also investigated by some molecular simulations [8,80,87–90]. Montmorillonite has

the highest gas adsorption capacity, followed by illite/smectite mixed layer, kaolinite, chlorite, and illite [91].

Another key parameter related to gas adsorption is the moisture in shales. Recent experimental work reported that both organic matter and clay minerals are originally moisture equilibrated at the reservoir conditions [92]. Moreover, the moisture content is increased by injecting water-based fluid during the hydraulic fracturing process. Generally, interactions between water and shales are attributed to physical sorption on polar surfaces and chemical sorption on mineral surfaces, and most of the moisture content is related to clay minerals [86]. Despite negative effects on adsorption capacity, the precipitation of minerals that may block pore throats is avoided because the moisture can maintain the brine concentration. Krooss et al. [93] performed high-pressure adsorption measurements of methane on both dry and moisture-equilibrated Pennsylvanian coals and found that gas adsorption capacity was reduced because moisture contents tended to fill the narrow pores throats and take adsorption sites for gas [93]. The effects of moisture on gas capacity also depend on its microscopic distribution in the pore system, but few investigations of this topic have been conducted [94,95].

2.2.3 Negative excess adsorption phenomenon

An excess adsorption amount can become negative at high pressure because of improper use of a void volume for calculation of an excess adsorption isotherm and this phenomenon is defined as a negative excess adsorption phenomenon. A negative excess adsorption phenomenon was found in methane adsorption at high pressure by many scholars, which made the adsorption isotherms lose their physical meaning. Vidal et al. [15] first observed that there was negative excess adsorption in methane adsorption on activated carbons when the gas pressure approached 200 MPa.

Additionally, negative excess adsorption of methane on illite was also detected by Zhang et al. [96] with gas pressure up to 32 MPa. As Chen et al. [97] illustrated, when the total pore volume used in an excess adsorption amount calculation was obtained by multiplying the *x*- and *y*-dimensions and pore size, negative excess amounts were observed.

An adsorption amount obtained in experimental conditions (e.g., via a volumetric method) is known as a surface excess adsorption amount, which is determined by mass balance with a total gas amount introduced into an adsorption cell excluding the gas amount as the bulk phase left in the adsorption cell (i.e., n_T-$V_T \cdot \rho_g$) [98]. Generally, compared to the measurement of a void volume, determinations of the total gas amount and the bulk density are relatively accurate based on accurate measuring pressure and temperature, and equation of state, separately. Therefore, the main reason that leads to a negative excess adsorption amount lies in the measurement of a void volume of an adsorption cell. Traditionally, a void volume determined by helium expansion tests is always used for calculating an adsorption amount by mass balance, which is based on an assumption that helium does not adsorb under any conditions [99]. However, this assumption is not strictly true, and appreciable helium adsorption was found by many scholars in different materials, such as carbon black and zeolite [100–102]. Maggs et al. [100] focused on the helium adsorption effect on the determination of densities of different types of carbon within a broad temperature from 77 to 580 K, and they found that the apparent dead volume decreased with an increase in temperature. As noted by Suzuki et al.[101], a volume of zeolite determined by helium expansion tests was overestimated at room temperature and, therefore, the density of Y zeolite was underestimated. Moreover, Malbrunot et al. [103] calculated the excess isotherms by a void volume measured at 673 K and the isotherms were found always positive. Keller et al. [104]

reported that the deviation was about 2 % at room temperature when measuring a void volume by a helium pycnometer with pressure up to 120 KPa. Some scholars suggested that a volume was measured at either high temperatures or low pressures or using other methods (e.g., mercury porosimetry) [105–107]. However, these conditions are not always available; for example, some adsorbents such as polymers cannot tolerate such a high-temperature range. More recently, Lorenz et al. [108] proposed an algorithm based on kinetic data by using the Rubotherm magnetic suspension balance to deal with a helium sorption issue. All the previous studies mentioned above imply that helium adsorption in traditional helium expansion tests can significantly influence measurements of sample volumes. An adsorbed methane amount in adsorbents is underestimated when calculated using a void volume measured by helium tests, which is incorrect for the determination of gas resources in coal and the prediction of gas production [78,94,95,109]. Knowledge about helium adsorption is of great necessity and importance for accurate volume measurements and calculations of adsorption amounts.

Another reason for the negative excess adsorption phenomenon of methane is an improper use of a helium-based void volume rather than a methane-based one [46,110]. Helium atoms can penetrate small pores while methane molecules cannot probe, and helium atoms can also approach a surface more closely due to their small size, further resulting in an overestimation of a pore void volume. Therefore, a void volume of pores is dependent on an adsorbate [99] and the void volume tested by helium is always overestimated. To obtain accurate adsorption isotherms of methane, a methane-based volume is of great significance.

Recently, some studies have been published dealing with an estimation of a void volume based on an adsorbate. The distance of the closest approach of adsorbates to adsorbents was considered by

many scholars, which depended on the form of a solid-fluid potential [111,112]. Some scholars thought that an accessible volume to adsorbates was the region where the solid-fluid potential was negative [112,113]. However, this was proved too restrictive because molecules can also penetrate a region where the solid-fluid potential is positive due to high temperature [114]. Some scholars also used nitrogen as a probe molecule to determine a pore volume for methane adsorption calculations due to their similar molecular size (the kinetic dimensions for nitrogen and methane are 0.36 and 0.38 nm, respectively) [115]. Besides, a theoretical variable of an adsorbate accessible volume proposed by Li et al. [77] was applied for calculations of excess adsorptions of methane.

2.2.4 Sorption-induced swelling

Gas adsorption can lead to the deformation of the pore structure in shale reservoirs[16–19]. However, the adsorption isotherms in previous studies were calculated by assuming that the kerogen structure was fixed, and a pore volume was constant. The kerogen swelling happens in experiments and the pore volume is variable during adsorption, which cannot be determined at any moment. Therefore, a fixed pore volume measured by volumetric gas such as helium and argon under certain experimental conditions is used in calculations of an adsorption amount. For molecular simulations, freezing the kerogen structure will ignore the dynamic nature of kerogens and the interplay between a pore structure and gas molecules, which is not appropriate [20]. There are limited studies discussing kerogen swelling and its effect on adsorption amounts [16,19,20,116]. As indicated by Ho et al. [16], a kerogen volume increased with the adsorbed gas amount, and the maximum swelling of kerogens was approximately 5.4% and 11% for CO_2 and CH_4 at 19.5 MPa and 300 K, respectively. A volumetric strain increase as a function of pressure was observed by Sui and Yao before reaching a maximum [117]. A similar phenomenon was

witnessed by Wang et al. [116] that the volumetric strain increased to a maximum with an increase in pressure and further decreased gradually as pressure increases. Moreover, it was reported that the sorption-induced volumetric strain in coal and shale was related to an adsorbed CH_4 amount [118–121]. The kerogen swelling was also affected by adsorbate molecules and it decreases with an increase in the molecule size of an adsorbate (CO_2 > CH_4 > C_2H_6 > C_3H_8) [17]. Additionally, the kerogen swelling can lead to high porosity and thus an accessible pore volume can become larger [16].

However, it is very difficult and time-consuming to measure the adsorption-induced volume strain for kerogen in experiments because its deformation is small and extraction of kerogen from shale samples is complex [18]. Thus, it is of great importance to use a theoretical model for the description of kerogen swelling. In previous studies, theoretical models were proposed by many scholars to investigate coal swelling. A Langmuir-type model was proposed by Levine to fit the sorption-induced volumetric strain in coal and was validated by adsorption experiments of bituminous coal from Illinois [122]. Afterwards, Pan and Connell developed a theoretical model for the description of sorption-induced coal swelling under equilibrated conditions using an energy balance [123]. In their method, it was assumed that the change in the surface energy was equal to the change in the elastic energy of the solid phase [123]. Liu and Harpalani also proposed a theoretical technique for modeling the volumetric strain in coal matrix by using parameters including elastic properties, physical properties of coal, and sorption parameters, which also had an excellent agreement with laboratory data [124].

2.2.5 Adsorption models

Several adsorption models have been proposed to model gas adsorption phenomena by some researchers [125–129], including the Langmuir model, Henry's model, BET model, and pore-filling model. A literature review of these models is discussed as follows.

Langmuir model

Langmuir model, which can be used for monolayer adsorption, is written as,

$$N_a = \frac{N_0 K_0 P}{1+K_0 P} \tag{2.3}$$

where N_a is the adsorbed amount under an equilibrium condition, N_0 refers to the maximum adsorbed capacity, P is the pressure, and K_0 represents the Langmuir constant.

K_0 is a function of temperature and it is shown in the following form,

$$K_0 = A_0 e^{\frac{E_0}{RT}} \tag{2.4}$$

where A_0 represents the prefactor, E_0 is the binding energy of the adsorption site, R is the universal gas content, T represents the temperature.

When the pressure is extremely low, Henry's model can be obtained,

$$N_a = \lim_{P\to 0} \frac{N_0 K_0 P}{1+K_0 P} = K_H P \tag{2.5}$$

where K_H is Henry's constant, which is also a function of the binding energy and temperature.

The excess adsorption amount can be derived from the equation (2.3),

$$N_e = \frac{N_0 K_0 P}{1+K_0 P}\left(1 - \frac{\rho_b}{\rho_a}\right) \tag{2.6}$$

where N_e is the excess adsorption amount, ρ_b represents the density of the bulk phase, and ρ_a represents the density of the adsorbed phase. According to some experimental and simulation data, the Langmuir model can be used for description of the adsorption in shale and coal under the reservoir conditions.

An empirical parameter *k* has been introduced in the Langmuir model by some scholars to improve its accuracy to model the adsorption under high-pressure conditions [130], and the equation (2.6) can be written in the following forms,

$$N_e = \frac{N_0 K_0 P}{1+K_0 P}\left(1-\frac{\rho_b}{\rho_a}\right) + kP \tag{2.7a}$$

$$N_e = \left(\frac{N_0 K_0 P}{1+K_0 P} + kP\right)\left(1-\frac{\rho_b}{\rho_a}\right) \tag{2.7b}$$

The equations above can be only used for one type of adsorption site. However, two or more types of adsorption sites with different characteristic energies exist in real adsorbents [131,132]. Then the single-site Langmuir model can be extended to a dual-site model by introducing a coefficient α,

$$N_a = N_0\left[(1-\alpha)\frac{K_1 P}{1+K_1 P} + \alpha\frac{K_2 P}{1+K_2 P}\right] \tag{2.8}$$

$$\theta = \frac{N_a}{N_0} = (1-\alpha)\frac{K_1 P}{1+K_1 P} + \alpha\frac{K_2 P}{1+K_2 P} \tag{2.9}$$

where K_1 and K_2 are equilibrium constants, which can be calculated by the equation (2.4), α is a coefficient for description weights of each type of adsorption sites ($0<\alpha<1$), and θ represents the surface coverage. Additionally, the excess adsorption amounts for dual-sites adsorption can be shown as,

$$N_e = N_0 \left[(1-\alpha)\frac{K_1 P}{1+K_1 P} + \alpha \frac{K_2 P}{1+K_2 P}\right](1-\frac{\rho_b}{\rho_a}) \quad (2.10)$$

BET model

On the basis of the multilayer adsorption assumption, the BET model is developed. This model can be applied for interpretation of Type II isotherms and the reversible part of Type IV isotherms [127]. It is shown as,

$$N_a = \frac{1}{\frac{1}{N_0 C}+\frac{C-1}{N_0 C P_0}P}\frac{1}{\frac{P_0}{P}-1} \quad (2.11)$$

where N_a represents the adsorbed amount at relative pressure P/P_0, N_0 is the monolayer adsorption capacity, P_0 is the gas saturation pressure, P is the equilibrium pressure, and C is a constant exponentially linked with the monolayer adsorption energy,

$$C = Ae^{\frac{\Delta E}{RT}} \quad (2.12)$$

where A is the prefactor, ΔE is the adsorption energy.

The equation (2.11) can only describe adsorption isotherms under the relative pressure ranging from 0.05 to 0.4 P/P_0 [133]. Therefore, it is modified to be used to a wide pressure range, which is known as Dent's model [134],

$$N_a = \frac{N_0 C_1 \frac{P}{P_0}}{1-C_2\frac{P}{P_0}+C_1\frac{P}{P_0}}\frac{1}{1-C_2\frac{P}{P_0}} \quad (2.13)$$

where C_1 and C_2 are constants for the primary and secondary adsorption sites and can be calculated using the equation (2.12).

The equations (2.11) and (2.13) cannot be used for modeling supercritical gas adsorption behavior where the saturation pressure doesn't exist [128,135,136]. Therefore, the BET model can be rarely used to describe methane adsorption in shales or coal but can be used for water vapor adsorption in wood or some geomaterials [86,133,134].

Pore-filling model

On the basis of the Polanyi adsorption potential theory, the pore-filling model is developed, such as the Dubinin-Astakhov (D-A) equation, and the Dubinin-Radushkevich (D-R) equation.

The D-A equation can be shown as,

$$N_a = N_0 exp\left\{-\left[\frac{RT}{\beta E} ln\left(\frac{P_0}{P}\right)\right]^n\right\} \quad (2.14)$$

And the D-R equation can be obtained when *n* equals 2 in the equation (2.14)

$$N_a = N_0 exp\left\{-\left[\frac{RT}{\beta E} ln\left(\frac{P_0}{P}\right)\right]^2\right\} \quad (2.15)$$

where N_a is the absolute adsorbed amount, N_0 is the volume of pores, β is the coefficient for sorbate affinity, E represents the characteristic energy, R is the universal gas constant, P_0 is the saturation pressure of the bulk gas, T is the temperature, and P is the equilibrium pressure.

The excess adsorption amount can be obtained,

$$N_e = N_0 exp\left\{-\left[\frac{RT}{\beta E} ln\left(\frac{P_0}{P}\right)\right]^n\right\}\left(1 - \frac{\rho_b}{\rho_a}\right) \quad (2.16)$$

$$N_e = N_0 exp\left\{-\left[\frac{RT}{\beta E} ln\left(\frac{P_0}{P}\right)\right]^2\right\}\left(1 - \frac{\rho_b}{\rho_a}\right) \quad (2.17)$$

To improve the fitting performance, an empirical constant *k* is introduced in the equations (2.16),

$$N_e = N_0 exp\left\{-\left[\frac{RT}{\beta E} ln\left(\frac{P_0}{P}\right)\right]^n\right\}\left(1-\frac{\rho_b}{\rho_a}\right) + kP \quad (2.17)$$

$$N_e = N_0 exp\left\{-\left[\frac{RT}{\beta E} ln\left(\frac{P_0}{P}\right)\right]^n\right\}\left(1-\frac{\rho_b}{\rho_a}\right) + kP\left(1-\frac{\rho_b}{\rho_a}\right) \quad (2.18)$$

Even though the D-A and D-R equations can be applied for modeling adsorption behavior in shales and coals, some problems are still existing:

1. They can only be used to predict isotherms at a certain temperature, because of different characteristic isothermal curves for the D-R and D-A fitting at different temperatures [137].
2. Empirical equations are used for calculation of the saturation pressure for supercritical gas (P_0), which is controversial [128,136].
3. The semiempirical value for the adsorbed density is used to fit the adsorption isotherms by the D-R and D-A equations [128,130].

Generally, the excess adsorption model is a function of temperature and pressure or the density of adsorbate. Therefore, we can replace the pressure (P, P_0) with the density of adsorbate (ρ_b, ρ_a), and the equations are summarized in **Table 2.1**.

Table 2. 1 Summarization of different adsorption models [10,130]**.**

Style	No.	Fitting model	Assumption	Ref
Langmuir-style model	1	$\boldsymbol{N_e = \frac{N_0 K_0 \rho_b}{1+K_0\rho_b}(1-\frac{\rho_b}{\rho_a})}$	ρ_a = 420 kg/m^3, ρ_b is variable.	
	2	$\boldsymbol{N_e = \frac{N_0 K_0 \rho_b}{1+K_0\rho_b}\left(1-\frac{\rho_b}{\rho_a}\right) + k\rho_b}$	ρ_a = 420 kg/m^3, ρ_b is variable.	[130]
	3	$\boldsymbol{N_e = (\frac{N_0 K_0 \rho_b}{1+K_0\rho_b} + k\rho_b)\left(1-\frac{\rho_b}{\rho_a}\right)}$	ρ_a = 420 kg/m^3, ρ_b is variable.	
	4	$\boldsymbol{N_e = N_0\left[(1-\alpha)\frac{K_1P}{1+K_1P} + \alpha\frac{K_2P}{1+K_2P}\right](1-\frac{\rho_b}{\rho_a})}$	ρ_a is an unknown constant, P is variable.	[138]

	5	$N_e = N_0 exp\left\{-\left[\frac{RT}{\beta E} ln\left(\frac{\rho_b}{\rho_a}\right)\right]^n\right\}\left(1-\frac{\rho_b}{\rho_a}\right)$	ρ_a = 420 kg/m^3, ρ_b is variable.	
D-A style model	6	$N_e = N_0 exp\left\{-\left[\frac{RT}{\beta E} ln\left(\frac{\rho_b}{\rho_a}\right)\right]^n\right\}\left(1-\frac{\rho_b}{\rho_a}\right) + k\rho_b$	ρ_a = 420 kg/m^3, ρ_b is variable.	
	7	$N_e = N_0 exp\left\{-\left[\frac{RT}{\beta E} ln\left(\frac{\rho_b}{P}\right)\right]^n\right\}\left(1-\frac{\rho_b}{\rho_a}\right) + k\rho_b\left(1-\frac{\rho_b}{\rho_a}\right)$	ρ_a = 420 kg/m^3, ρ_b is variable.	[139]

Chapter 3 Mathematical modeling and computation techniques

With the development of high-performance computing during the last few decades, molecular simulation technology has been applied in all parts of science. MD and Monte Carlo (MC) methods are introduced to molecular simulation in many physical models, which can help predict and understand some behaviors of those molecular systems. This is of advantage for those systems which are not experimentally available. Therefore, molecular simulation can be referred to as numerical experiments. It provides a straightforward method for analyzing a system in both microcosm and macrocosm, including the details such as interactions between atoms, topological structures of molecules, thermodynamic properties. In the study of interactions between fluids and shale matrix, molecular simulation also plays an important role.

3.1 Monte Carlo Method

Monte Carlo methods are a kind of computational algorithms by repeating random sampling to solve problems, which have a probabilistic interpretation. According to the law of large numbers, the empirical mean of some independent samples of the variable can be used as the approximation of the expected value of a random variable. A Markov chain Monte Carlo (MCMC) sampler is useful if the probability distribution of the variable is parametrized [140,141]. Based on the prescribed stationary probability distribution, a new sample will be generated. In the limit, the newly generated sample will be samples from the target distribution.

3.1.1 GCMC Method

In this study, the GCMC method is employed for investigation of the adsorption behavior of different gases in the shale reservoirs. The system involved has constant chemical potential (μ), volume (V), and temperature (T) [142]. This system consists of a reliable adsorbent structure and some adsorbate particles, which is determined by the fixed μ and T. The particles are randomly deleted, inserted, displaced or rotated under the conditions GCMC permits. This move is accepted according to a probability depending on the energy difference between new and old system configuration [143]. The density and energy in the system will fluctuate until the targeted condition is achieved. In the Metropolis sampling scheme [140], the random displacement is accepted with a probability

$$p_{move} = \min\left[1, \exp\left(-\frac{\Delta U}{k_B T}\right)\right] \tag{3.1}$$

The acceptance probability of insertion is

$$p_{insertion} = \min\left[1, \frac{V}{\Lambda^3 (N+1)} \exp\left(\frac{\mu - \Delta U}{k_B T}\right)\right] \tag{3.2}$$

Similarly, the acceptance probability of deletion is

$$p_{deletion} = \min\left[1, \frac{\Lambda^3 N}{V} \exp\left(\frac{\Delta U - \mu}{k_B T}\right)\right] \tag{3.3}$$

in which $\Delta U = U_{new} - U_{old}$ is the potential energy difference between new and old system configuration, V is the volume of the system, k_B is the Boltzman constant, Λ is the thermal de Broglie wavelength, and N is the number of particles. The acceptance probability is only dependent on the current configuration. In the simulation, the chemical potential μ can be substituted by

pressure and the fugacity coefficient of the ideal gas reservoir. More details of this method are explained by Metropolis et al. [140]. The adsorption isothermal is plotted as the total uptake of particles adsorbed versus pressure.

3.2 Molecular Dynamics

MD simulation is of a huge advantage to investigate the behavior of materials at a molecular level. Especially for adsorption processes, the adsorption selectivity and diffusion can be understood at a molecular scale. The aim of MD simulations is to develop a bridge that can connect the macroscopic thermodynamic world with the world at the microscopic level.

3.2.1 Governing equations

With the known initial configuration of the MD simulation system and some governing equations, particles' evolution with time can be calculated by MD simulation. The force (*F*) exerting on each atom can be described as the negative gradient of the potential energy *U(r)* between two atoms with a distance *r*:

$$F = -\nabla U(r) \tag{3.4}$$

The total force acting on each atom is numerically determined by Newton's equation of motion for classical mechanics. Newton's second law is given as:

$$F_i = m_i a_i = m_i \frac{d^2 q_i}{dt^2} \tag{3.5}$$

in which F_i represents the force vector acting on particle *i*, m_i is the mass of particle *i*, a_i represents the acceleration, q_i is the position vector and *t* represents time.

We can introduce to the velocity vector v_i, and then the equation (3.5) can be written as:

$$F_i = m_i \frac{v_i}{t} \tag{3.6}$$

$$v_i = \frac{dq_i}{dt} \tag{3.7}$$

3.2.2 Integration of equations of motion

By integrating the equations of motions, we can get the time evolution of the system, the momentum and the position of each atom at each time step, and the steps are shown in short:

1. Calculate the force exerting on each particle in the system according to its position relative to other particles.
2. Get and update the position of each particle at the time of $t+\delta t$ by integrating the equations of motions.

There are several integration algorithms, which can be used for advancing the system, such as the Verlet algorithm and the Leapfrog algorithm. The most common algorithms are the Verlet algorithm and it will be derived in this section. Similar to other algorithms using the finite difference methods, properties including positions, velocities, and accelerations of atoms can be approximated by Taylor expansions. We take the approximation of positions as an example here, and the positions at the time of $t\pm\delta t$ can be written as:

$$q_i(t+\delta t) = q_i(t) + (\frac{dq_i}{dt})_t \delta t + \frac{1}{2}\left(\frac{d^2 q_i}{dt^2}\right)_t (\delta t)^2 + \frac{1}{6}\left(\frac{d^3 q_i}{dt^3}\right)_t (\delta t)^3 + O(\delta t)^4 \tag{3.8}$$

$$q_i(t-\delta t) = q_i(t) - \left(\frac{dq_i}{dt}\right)_t \delta t + \frac{1}{2}\left(\frac{d^2 q_i}{dt^2}\right)_t (\delta t)^2 - \frac{1}{6}\left(\frac{d^3 q_i}{dt^3}\right)_t (\delta t)^3 + O(\delta t)^4 \tag{3.9}$$

By integrating the equation (3.8) with (3.9), the equation (3.8) can be expressed as:

$$q_i(t+\delta t) = 2q_i(t) - q(t-\delta t) + \left(\frac{d^2 q_i}{dt^2}\right)_t (\delta t)^2 + O(\delta t)^4 \quad (3.10)$$

This equation is the Verlet method and $O(\delta t)^4$ represents the truncation error of this method, which is the difference between the true function and the approximated Taylor expansions. A small timestep can increase the accuracy of the approximation. The timestep is often set to be 1 femtosecond (10e-15 seconds) in the molecular simulations.

The velocity term is obtained using finite difference methods:

$$v_i(t) = \frac{q_i(\delta t) - q_i(t-\delta t)}{2\delta t} \quad (3.11)$$

Knowing the current position $q_i(t)$ and velocity $v_i(t)$ and the position $q_i(t-\delta t)$ at the previous timestep, we can calculate the new position $q_i(t+\delta t)$ at the next timestep for all particles in the system by the Velert algorithm.

3.2.3 Periodic boundary

Figure 3.1 displays a simulation box, which represents an MD simulation system. Six surfaces of the simulation box are open and the particles start to interact and traject when the simulation starts. Some of the particles may cross the boundaries and move out of the box due to interaction with surrounding atoms. Under this condition, the total number of particles in the system is not constant and the density will change at different times. We apply the periodic boundary conditions (PBC) to deal with the issue and make the system periodic.

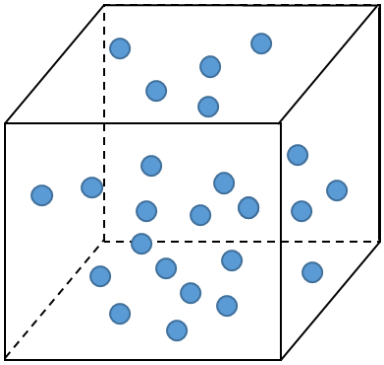

Figure 3. 1 Schematic of a simulation box.

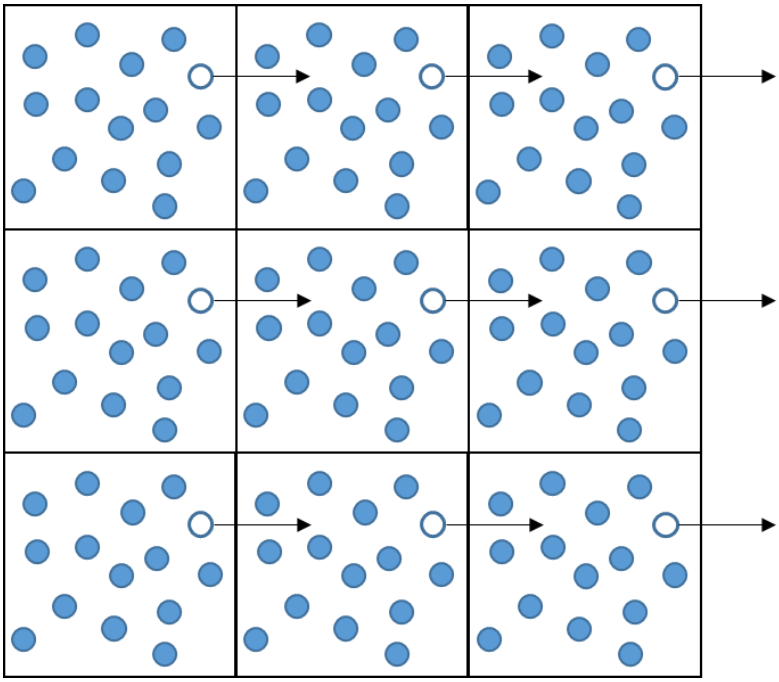

Figure 3. 2 Principles of Periodic Boundary Conditions displayed in two dimensions.

As shown in **Figure 3.2**, the atom will enter again from one side of the box when it moves out on the other side. These nine boxes all have the same movement and the number of each box can be maintained. Use of Periodic Boundary Conditions in the system can keep the density of the system constant in the simulation, and it can simulate a large infinite bulk with few atoms, which increases the simulation efficiency.

3.2.4 Force Fields

Force fields are used for describing the basic parts of inter- and intramolecular forces and they are a collection of equations with related constants to describe the molecular geometry and structures. Bond stretching, angle bending, torsion around bond and non-bonded interactions are important components of intramolecular terms. Intermolecular forces consist of van der Waals (vdW) and electrostatic interactions. In the system, each atom is described by a set of force field parameters and a suitable force field is of great significance to the simulation results. The total potential energy in a system is composed of bonded interaction and non-bonded interactions, and we will discuss them in the following part.

Bonded interactions

The bonded interaction which is also called intramolecular interaction can be written as:

$$U_{bonded} = U_{bond} + U_{angle} + U_{dihedral} + U_{impropers} \quad (3.12)$$

These bonded energy terms are used for the description of the required energy to deform covalently bonded atoms.

The first term U_{bond} refers to the potential energy of bond stretching. As shown in **Figure 3.3**, two balls representing two atoms are connected with a spring. The spring is an analogy to the chemical bond and the bond length between two atoms changes because of vibrations. We use Hooke's Law to calculate this term:

$$U_{bond} = k_{bond}(r - r_0)^2 \quad (3.13)$$

where k_{bond} is the force constant, r represents the distance between two atoms' center, and r_0 is the equilibrium bond length. In some force fields, the chemical bonds are treated as rigid, and it means that these bonds cannot stretch and will keep constant with time.

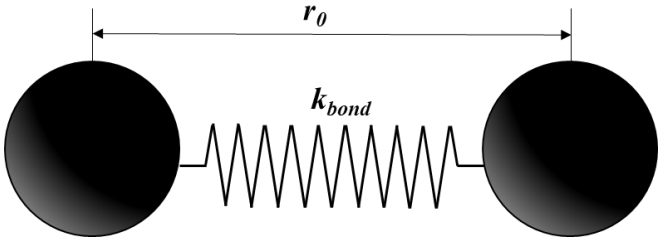

Figure 3. 3 Schematic of bond stretching between two atoms.

The angle formed by three atoms varies with time due to vibration, which is similar to the bond length (**Figure 3.4**). The potential energy required to bend the angle can also be written with a harmonic function:

$$U_{angle} = k_{angle}(\theta - \theta_0)^2 \quad (3.14)$$

where k_{angle} is constant, θ is the angle formed by three atoms, and θ_0 is the equilibrium angle.

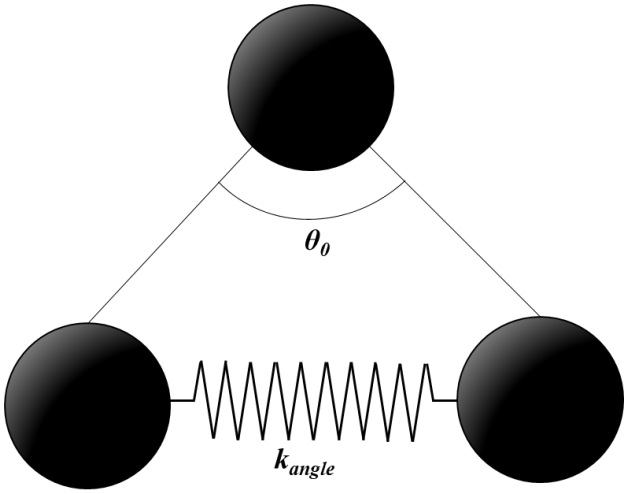

Figure 3. 4 Schematic of angle bending between three atoms.

The interactions between four bodies including dihedral and improper are also important to be considered for molecules with long chains. The dihedral terms can be considered as harmonic type or charmm type:

$$U_{dihedral} = k_{dihedral}[1 + dcos(n\phi)] \quad \text{(harmonic)} \quad (3.15)$$

where $k_{dihedral}$ is constant, d equals to ±1, n is a non-negative integer, ϕ is the angle between plane A and B (**Figure 3.5**), and plane A and B is defined by 1-2-3 and 2-3-4, separately.

$$U_{dihedral} = k_{dihedral}[1 + cos(n\phi - d)] \quad \text{(charmm)} \quad (3.16)$$

where $k_{dihedral}$ is constant, d is an integer in the unit of degree, and n is a non-negative integer.

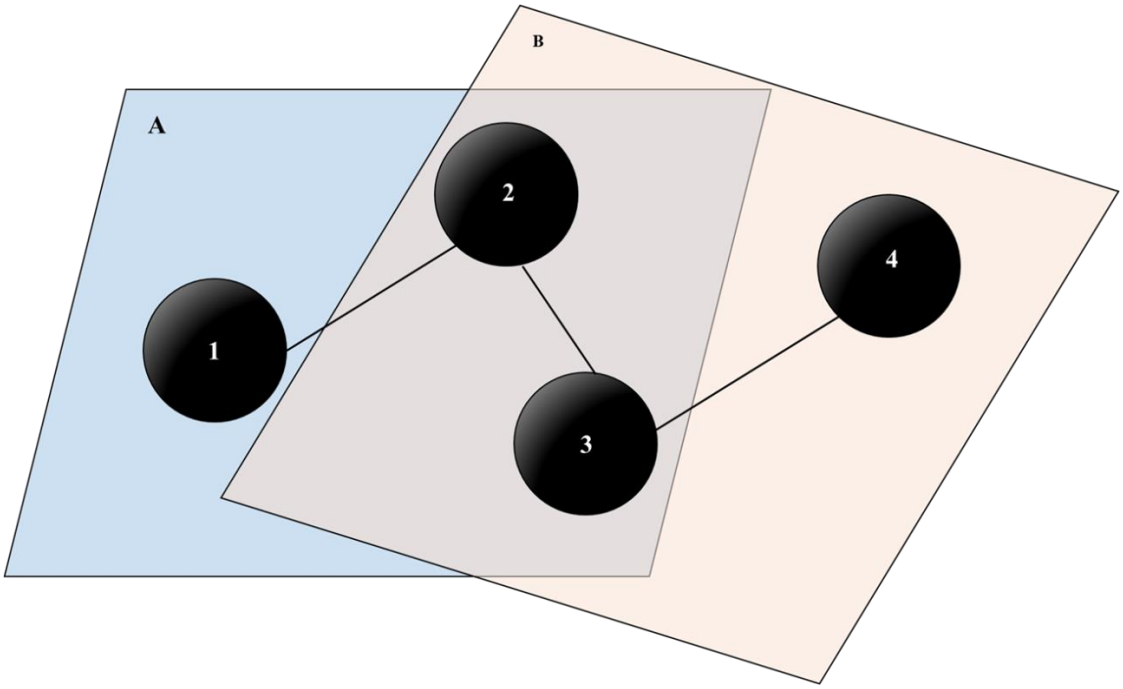

Figure 3. 5 Schematic of dihedrals between four bodies.

The improper term is the least common potential in intramolecular interactions and it is used for the description of the energy associated with the displacement of atoms out of their equilibrated plane (**Figure 3.6**). It can be expressed as:

$$U_{improper} = k_{improper}(\chi - \chi_0)^2 \quad (3.17)$$

where $k_{improper}$ is constant, χ is the angle between two planes shown in **Figure 3.6**, and χ_0 is the equilibrium angle between these two planes.

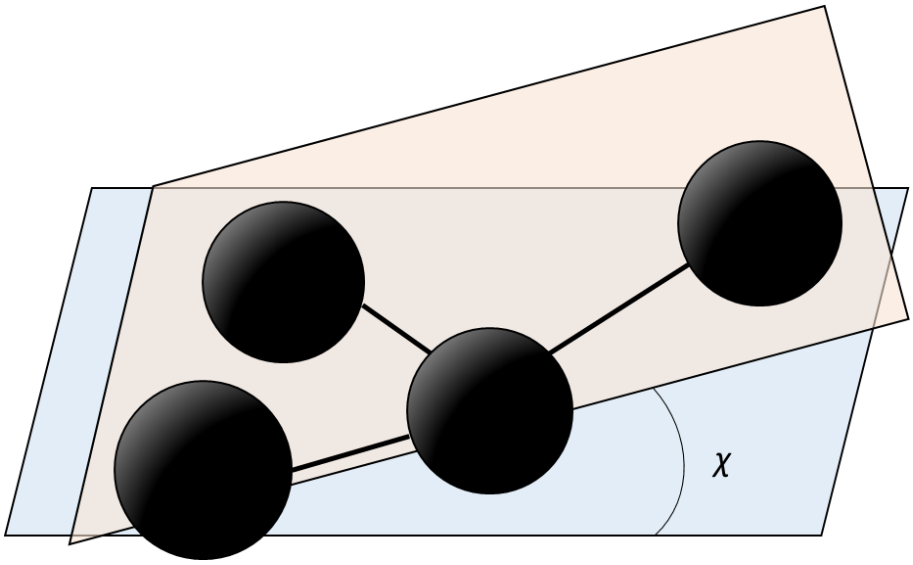

Figure 3. 6 Schematic of improper (out of plane) term for four atoms.

Non-bonded interactions

The non-bonded interactions include van der Waals and electrostatic forces, and can be expressed as:

$$U_{non-bonded} = U_{electrostatic} + U_{vdW} \tag{3.18}$$

Van der Waals forces are typically short-range interactions and include Keesom forces, Debye forces, and London dispersion forces. The Lennard-Jones 12-6 potential is the most common model to describe the short-range van der Waals force:

$$U(r_{ij}) = \begin{cases} 4\varepsilon_{ij}\left[\left(\frac{\sigma_{ij}}{r_{ij}}\right)^{12} - \left(\frac{\sigma_{ij}}{r_{ij}}\right)^{6}\right] & r_{ij} \le r_{cutoff} \\ 0 & r_{ij} > r_{cutoff} \end{cases} \tag{3.19}$$

where r_{ij} represents the intersite distance between atoms i and j, ε_{ij} is the well depth of the L-J potential, σ_{ij} is the L-J size parameter, and r_{cutoff} is a cutoff radius, beyond which the interaction is negligible. Cross interaction parameters for unlike pairs are determined by the Lorentz-Berthelot combining rule:

$$\sigma_{ij} = \frac{1}{2}\left(\sigma_{ii} + \sigma_{jj}\right) \tag{3.20}$$

$$\varepsilon_{ij} = \sqrt{\varepsilon_{ii}\varepsilon_{jj}} \tag{3.21}$$

Figure 3.7 displays the potential profile generated by the Lennard-Jones 12-6 potential. Based on the equation (3.19), the repulsive forces are contributed by the term $1/r^{12}$ and the attractive forces increase with the term $1/r^{6}$. The repulsion happens when the distance between two molecules is smaller than a specific value at which the force between molecules is zero, and it is caused by the overlapping of the electron clouds of two molecules.

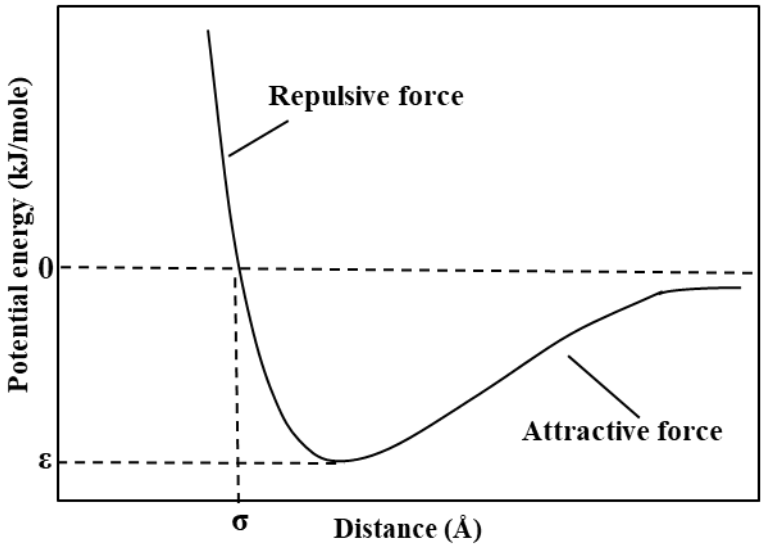

Figure 3. 7 Potential profile generated by the Lennard-Jones 12-6 potential.

The electrostatic interactions are considered as strong forces, which are typically long-range forces. The partial charges of each atom are generally obtained according to electronegativity differences and quantum mechanics, which can replicate the dipole moment of molecules. To simplify the calculation of electrostatic forces, the electrostatic interaction can be treated as simple point charge interaction, and we can use Coulomb's Law to calculate the electrostatic force between two atoms:

$$U_{Coul} = \frac{e^2}{4\pi\varepsilon_0}\sum_{i\neq j}\frac{q_i q_j}{r_{ij}} \tag{3.22}$$

where q_i and q_j represent the charge of particle *i* and *j* with the unit of *e*, respectively. ε_0 is the permittivity of free space (ε_0 = 8.8543e-12 *F/m*).

3.2.5 Cut-off radius

A cut-off radius is used in molecular simulations to save the computational time for calculating the short-range vdW forces. The vdW force decreases a lot and can be neglected when two molecules go apart and it can be neglected after the cut-off radius, which has a small effect on the total non-bonded interactions. However, use of a cut-off radius can lead to discontinuity and energy disturbance. A cut-off which is in the range of 8 to 12 Å can usually mitigate these effects [144].

3.2.6 Long-range interactions

The electrostatic interactions do not decrease as fast as the vdW forces when two molecules go apart (see equations 3.19, 3.22) [145]. For the long-range electrostatic interactions, use of a cut-off radius in the calculation is not a good idea, which can result in lost information and inaccurate

computed interactions. To save the computational time, the Ewald Summation Method and Particle Particle Particle Mesh (PPPM) are applied for dealing with long-range electrostatic interactions.

In the Ewald Summation Method, the long-range interaction is divided into a short-range contribution and a long-range contribution. For the short-range contribution, it is calculated in real space, while the long-range contribution is calculated via the Poisson law with a Fourier transform. In order to get an accurate result of the electrostatic interaction, the charge of the molecular system is required to be neutral. This method can ensure a rapid convergence for the calculation of electrostatic interactions and is of great advantage. By dividing the particle charges into mesh grids, the PPPM can solve the Poisson equation and calculate out the Fourier part more efficiently compared to the Ewald Summation Method [146]. A large mesh grid can reduce the computation time but lead to less accurate electrostatic forces.

3.2.7 Ensembles

In a system, the thermodynamic properties of all the atoms contained should meet certain constraints of the ensemble. These constraints could be the number of particles, volume, temperature, pressure or combinations of them. In a specific ensemble, we need to understand which variable is fixed and which one is allowed to change around a certain value. The movement of an individual particle in the system is regarded to be meaningful when the properties of the ensemble are consistent with the set constraints.

There are four common ensembles, including microcanonical ensemble, canonical ensemble, grand canonical ensemble, isothermal-isobaric ensemble.

Microcanonical ensemble (NVE)

In NVE ensemble, the number of particles, the volume and the total energy of the system are kept constant during the simulation time. The temperature is allowed to fluctuate with the kinetic energy of the system. However, it is very difficult to calculate the total energy of a system in the experiments, and thus the microcanonical ensemble is not realistic, which can be only achieved in the molecular simulation.

Canonical ensemble (NVT)

The total number of particles, the volume and the temperature in the system are fixed in this ensemble. The kinetic energy of the system will change and the total energy in the system will exchange with an external imagined heat bath. This ensemble is always used when comparing with the experimental results because the temperature and the volume can be easily controlled in the experiments.

Grand canonical ensemble (μVT)

The total number of particles and the heat are allowed to exchange with a reservoir. Then the chemical potential, the volume and the temperature are kept at a constant average. This ensemble is usually applied for GCMC simulation and modelling the adsorption phenomenon.

Isothermal-isobaric ensemble (NPT)

The total number of particles, the pressure, and the temperature are kept fixed with a fluctuating system volume. This ensemble can be used in some chemical reactions which are conducted under a constant-pressure condition. Additionally, for model systems in which the evaluation of the virial

expansion cannot be carried out, this ensemble is of great use to measure the equation of state in these systems.

3.2.8 Temperature control

In some ensembles discussed in 3.2.7, it is necessary to keep the temperature constant. Several methods are introduced to control the temperature in the system, such as the Berendsen thermostat, and the Nosé-Hoover thermostat.

The temperature of the system can be related to the average kinetic energy:

$$E_{ki} = \frac{3}{2} N k_B T = \frac{1}{2} \sum_i^N m_i \langle v_i^2 \rangle \quad (3.23)$$

where N is the particle number, k_B is the Boltzman constant, T is the temperature, m_i is the mass of particle i, v_i is the velocity of particle i.

The Berendsen thermostat

In the Berendsen thermostat, the system is coupled to an external hypothetical heat bath with a constant T_0 [147]. The velocities are scaled at each timestep and the temperature changes according to this equation:

$$\frac{dT(t)}{dt} = \frac{1}{\tau}(T_0 - T(t)) \quad (3.24)$$

in which τ is the coupling parameter determining how the system is affected by the heat bath. This parameter should be chosen with care. When $\tau \rightarrow \infty$, the Berenden thermostat doesn't work and the system acts like a microcanonical ensemble. The targeted temperature will not be reached for a canonical ensemble. If τ is too small, unrealistic low-temperature fluctuations will be caused.

This thermostat is easy to implement and can help a non-equilibrated system achieve equilibrium, but it cannot generate a correct canonical ensemble.

The Nosé-Hoover thermostat

To probe a correct canonical ensemble, the Nosé-Hoover thermostat was introduced by Nosé [148] and then improved and simplified by Hoover [149]. An external heat bath is introduced to regulate the system temperature and gives the atoms an extra degree of freedom. Heat is exchanged between the heat bath and system, and the total energy of the system is changed. The details of the algorithm for the Nosé-Hoover thermostat will not be discussed here and they can be found in this literature [149].

Though this thermostat is not fast compared to the Berendsen thermostat, it can maintain a canonical ensemble, which is considered as a reliable tool for simulation in an equilibrated system and predictions for thermodynamic properties.

3.2.9 Pressure control

Two common barostats are used for controlling the pressure in the system for an isothermal-isobaric (NPT) ensemble, which is the Berendsen barostat and the Nosé-Hoover barostat. By calculating the virial pressure, the volume of the simulation box is allowed to adjust and then the pressure in the system is controlled.

3.3 Software

In this study, we use the Large-scale Atomic/Molecular Massively Parallel Simulator (LAMMPS) to conduct our simulation work, which is a widely-used software with molecular dynamics code [150]. It is developed by the Sandia National Laboratories and focusing on the simulation of

inorganic and organic molecules, polymers, metal, and biomolecules. The software OVITO and VMD are used and help us visualize the molecular dynamics, which can give us a straight understanding of the world at a microscopic level [151,152].

Chapter 4 Molecular dynamics computations of brine-CO_2/CH_4-shale contact angles

4.1 Introduction

The rock wettabilities and water contact angles which can reflect interactions between CO_2, CH_4, brine and shale formations are of great significance to CO_2 sequestration and enhanced gas recovery processes. However, water contact angles on the surfaces of shale organic matter in the atmospheres of CO_2 and CH_4 under reservoir conditions are not well-understood. In this chapter, we present an investigation of water/brine contact angles as functions of temperature, pressure, salinity, ion types, and gas contents by MD simulations, and compare results with data from literature. It is found that temperature has profound effects on water contact angles below the critical temperature at an intermediate pressure. Meanwhile, water contact angles increase with pressure before reaching 180° at high pressure and the CO_2-water-shale organic matter system turns from a neutrally-wet state to a CO_2-wet state at the critical pressure of CO_2. We also demonstrate that salinity and ion types have minor impacts on the brine contact angles in the CO_2-brine-shale system. Only a slight increase in water contact angles is observed with increasing salinity, and an increase in brine contact angles caused by the divalent cations Mg^{2+} and Ca^{2+} is larger than that by the monovalent cations Na^{+} at the same salinity. Additionally, an increase in the CO_2 fraction of gas mixtures can increase water contact angles at the same pressure and temperature. The surfaces of shale organic matter have a stronger affinity for CO_2 than CH_4, which contributes to a higher CO_2 adsorption capacity and improves the displacement efficiency of CH_4.

The remainder of this chapter is organized as follows: In Section 4.2, the computational methods including the model configuration, force field, and MD simulation details are introduced. In Section 4.3, we illustrate the effects of temperature at both low and high gas pressures on the brine contact angles, and some other important influencing parameters such as pressure, gas content, salinity and ion types are also investigated. Additionally, implications for CO_2 sequestration in depleted shale gas reservoirs and shale gas production with the aid of CO_2 injection are explained. In Section 4.4, some key findings are summarized.

4.2 Computational methods

A graphene model has been successfully used to represent an organic pore surface in shale by many scholars [153,154]. Gas adsorption and transport in organic nanopores have been investigated at the molecular scale, which can also match with experimental results [38,93,154–157]. To increase the computational efficiency and avoid the surface roughness on the determination of a contact angle, a graphene surface is chosen as a proxy for an organic pore surface in shale. Though the surface roughness is not considered in our study, water contact angles in CO_2-brine-quartz/calcite systems were found to decrease with an increase in roughness [55,158,159].

Intermolecular interactions are calculated by a pairwise additive Lennard-Jones (LJ) 12-6 function, and the Lorentz-Berthelot mixing rule is used to calculate cross interaction parameters for unlike pairs. The interaction between the charged sites is calculated by equation (3.22). Water molecules are modeled using the SPC/E model (**Table 4.1**). The bond lengths and the angles of water molecules are constrained by the SHAKE algorithm. The CVFF (consistent valence force field) is applied to model CO_2 and CH_4 molecules, which has been shown to successfully describe their

interactions with a graphene surface [160,161]. Parameters for ions including Na^+, Ca^{2+}, Mg^{2+} and Cl^- are shown in **Table 4.1** [162].

Table 4. 1 Lennard-Jones parameters employed in the simulations [160–162]**.**

Site	ε (kcal mol^{-1})	σ (Å)	q (e)
C (graphene)	0.148	3.617	0.0
C (methane)	0.161	3.475	-0.4
H (methane)	0.038	2.461	0.1
C (carbon dioxide)	0.148	3.617	0.574
O (carbon dioxide)	0.228	2.860	-0.287
H (water)	0.1553	3.166	0.4238
O (water)	0	0	-0.8476
Na^+	0.04681	2.450	1.0
Ca^{2+}	0.45	2.361	2.0
Mg^{2+}	0.875	1.398	2.0
Cl^-	0.15	4.100	-1.0

We have performed simulations for water droplets adsorbed on an organic surface as a function of temperature, gas pressure, gas contents and salinity using simulation cells with dimensions (x, y, z) = (100, 70, 100) Å^3. Periodical boundary conditions are applied in the plane of the graphene slab, except the z-direction. A soft repulsive potential wall is set to ensure that motions of molecules are confined in the upper part of the simulation box [163]. The configuration for simulations of contact angles consists of an organic surface, a half-cylindrical droplet containing 1000 water molecules, and CO_2 or CH_4 molecules with different amounts (**Figure 4.1**). Unlike a

spherical water droplet, the use of a half-cylindrical geometry can lead to a straight contact line between water and substrate [164,165]. Therefore, the radius of the contact line is infinite and there is no contribution of the line tension due to curvature. As a consequence, the contact angle measured at the nanoscale can match that measured at the macroscale. The amounts of CO_2 and CH_4 molecules are adjusted to simulate different gas pressures (0-40 MPa) with various gas contents. The existence of protons, HCO_3^- and CO_3^{2-} resulting from the dissolution of CO_2 in water is neglected in the simulation [163]. The NVT ensemble is used in the simulation and the system temperature is controlled by a Nosé-Hoover thermostat. Newton's equations of motion are solved by the Verlet algorithm. Each simulation is conducted for 5 ns with a timestep of 1 fs. We use the first 3 ns to achieve an equilibrated state in the system and another 2 ns to collect data, such as density profiles. All the MD simulations are conducted via the software LAMMPS [150].

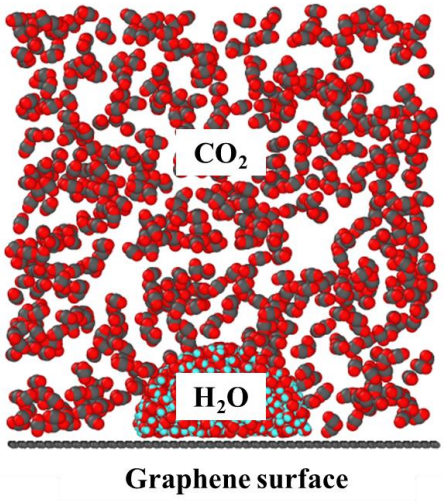

Figure 4. 1 Snapshot of a representative configuration of a water/CO_2/graphene system at 323K with CO_2 pressure of 5 MPa for simulation of contact angles and the graphene surface is perpendicular to the *z*-axis.

4.3 Results and discussion

Brine contact angles on graphene substrates are calculated by 2D density profiles of water, and the average positions of the carbon atoms in a graphene surface are regarded as a baseline. The density contours of the water droplets in the environment of CO_2 or CH_4 are fitted to a circle as shown in **Figure 4.2**. In **Figure 4.2(a)**, a schematic for calculations of a contact angle θ is illustrated, and we can obtain:

$$\theta + \gamma = \pi \tag{4.1}$$

$$\alpha + \beta = \alpha + \gamma = \frac{\pi}{2} \tag{4.2}$$

Therefore, we see that

$$\theta + \beta = \pi \tag{4.3}$$

$$\cos\beta = \cos(\pi - \theta) = \frac{h-R}{R} \tag{4.4}$$

Then the contact angle θ can be generated based on the following equation [166–168]:

$$\cos\theta = 1 - h/R \tag{4.5}$$

where R is the radius of the fitting circle in the dashed line and h is the maximum height of the water droplets.

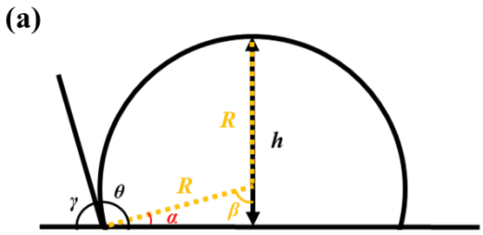

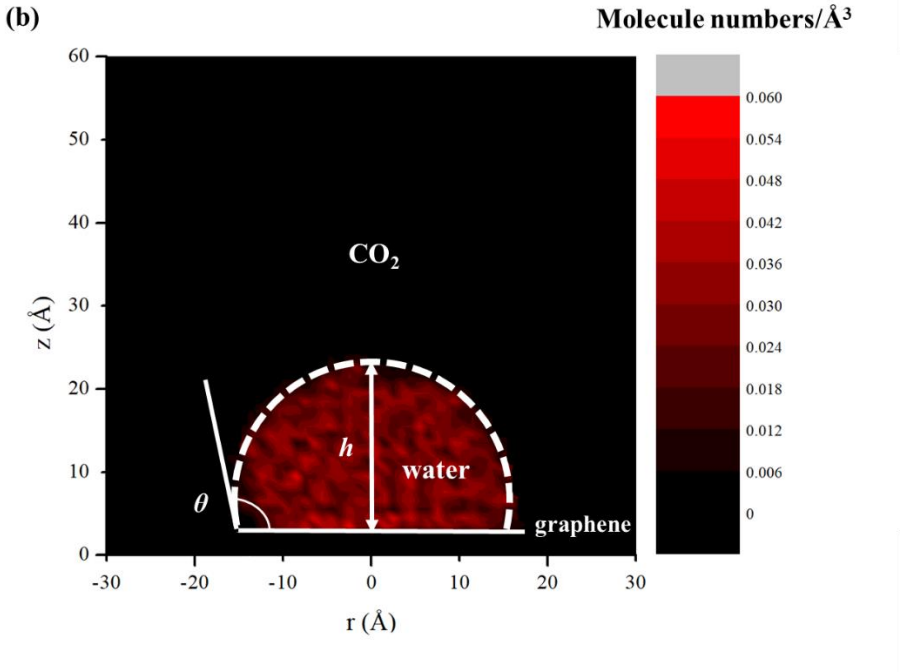

Figure 4. 2 (a) A schematic for calculating the contact angle; (b) density contours of a water droplet on the graphene surface in the environment of CO_2 at 292 K with CO_2 pressure of 5 MPa.

To validate the accuracy of the simulation set-up, a water contact angle on the graphene surface is also determined at ambient pressure. The water contact angle on a monolayer of graphene is within the range from 91° to 95° reported by other researchers and the determined contact angle in our simulation is approximately 92°, which is consistent with the data from the literature [169–171].

4.3.1 Water contact angles as a function of temperature with intermediate and high CO_2 pressures

To investigate the effects of temperature, we conduct MD simulations to obtain water contact angles at 292, 298, 313, 323 and 343 K with CO_2 pressure of 5 and 20 MPa, and the water droplets on the graphene surface at different temperatures with CO_2 pressure of 5 MPa are shown in **Figure 4.3**.

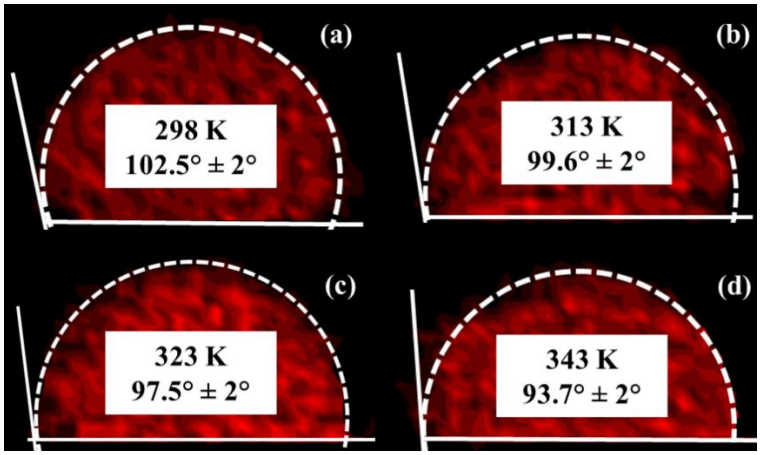

Figure 4. 3 The water droplets on the graphene surface at different temperatures (298, 313, 323, and 343 K) with CO_2 pressure of 5 MPa.

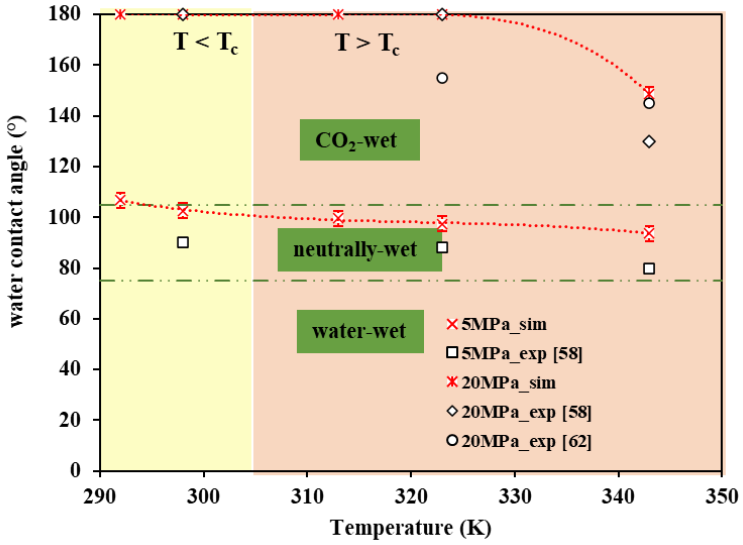

Figure 4. 4 Water contact angles on the shale surface at CO_2 pressure of 5 and 20 MPa as a function of temperature determined from MD simulation and experiments [58,62]**.**

Figure 4.4 displays the water contact angles determined from MD simulation at CO_2 pressures of 5 and 20 MPa as a function of temperature with the comparison of data from experiments [58,62]. Water contact angles data on a graphene surface in the atmosphere of CO_2 are not available in the literature, so we compare our simulation data with those obtained from experiments in organic-

rich shale. At an intermediate CO_2 pressure of 5 MPa, the water contact angle at 292 K increases by 13° compared to that at 343 K, which reveals a transition from a neutrally wet behavior at a high temperature toward a moderately CO_2-wet condition at a low temperature. Note that the relationship between wetting behaviors and contact angles in this study is based on the classification proposed by Fanchi (2005) [172]. This phenomenon is also observed in QMD (quantum MD) simulation of wetting behaviors of water nanodroplets on graphene [173]. The wettability of the graphene surface is weakened by a decreasing temperature [173]. Additionally, it is consistent with the effects of temperature on water contact angles in other CO_2-water-solid systems, such as quartz, mica, and sandstone [59,159,163,174]. When the temperature is below CO_2 critical temperature (304.13 K), an increase in contact angle with temperature is greater than that above the critical temperature, indicating that temperature has a more significant effect on the water contact angle below the critical temperature at an immediate pressure. These findings can also be quantified through the density profiles displayed in **figures 4.5** and **4.6**. The main peak of water molecules in the density profiles is enhanced with increasing temperature while the main peak of CO_2 molecules decreases. The initial configuration of the water droplets is redistributed more evenly along the *z*-axis at a low temperature, resulting in a larger contact angle. At a high pressure of 20 MPa, water contact angles reach 180° for temperature below 323 K, i.e., a completely CO_2-wet condition. Under this condition, water droplets float freely above the graphene surface in the atmosphere of CO_2. Obviously, the temperature has a stronger effect on water contact angles at immediate pressure [163]. The interactions between CO_2 and the graphene surface are strengthened by a decreasing temperature at CO_2 pressure of 5 and 20 MPa, leading to the sorption of CO_2 on the graphene and even a completely CO_2-wet condition.

There are variations between contact angles determined from MD simulation and experimental works although effects of temperature on the contact angles are found to be consistent. This is attributed to the TOC contents of shale samples in the experiments. A graphene surface is chosen to represent a shale surface in our simulation and it is 100% carbon. However, the shale samples have a much lower TOC content compared to the graphene surface. Thus, the contact angles in our simulation are larger than those obtained through experiments [61,175]. As mentioned before, some experiments showed that the water contact angle in CO_2-water-quartz systems increased with an increase in temperature [176]. This can be caused by the uncertainty in measuring the contact angles by experiments. Some important factors such as cleanliness and the degree of roughness of solid surfaces can result in the difficulty in measurement of water contact angles. However, a solid surface in the MD simulation is well established and is not affected by these uncertainties. By investigating the interactions between fluid and solid as a function of temperature, results can be provided with more confidence.

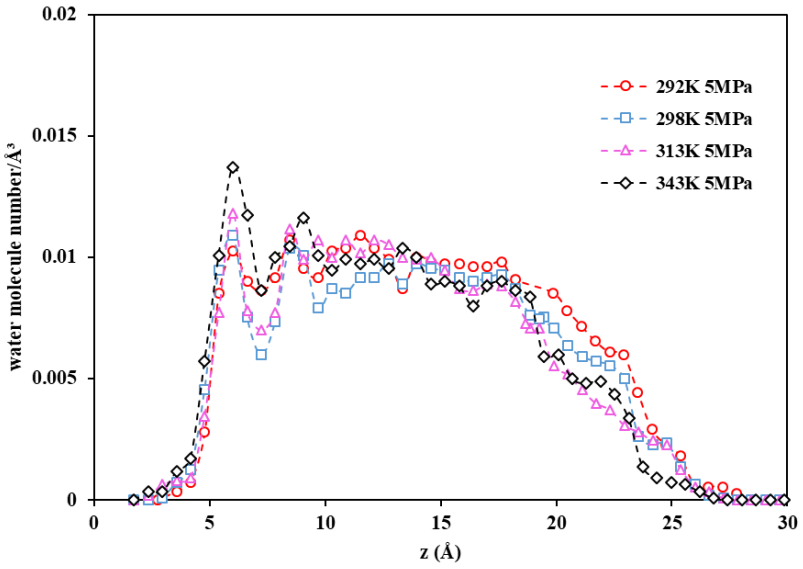

Figure 4. 5 Density profiles of water molecule number per Å³ along the *z*-axis with CO_2 pressure of 5 MPa at various temperatures.

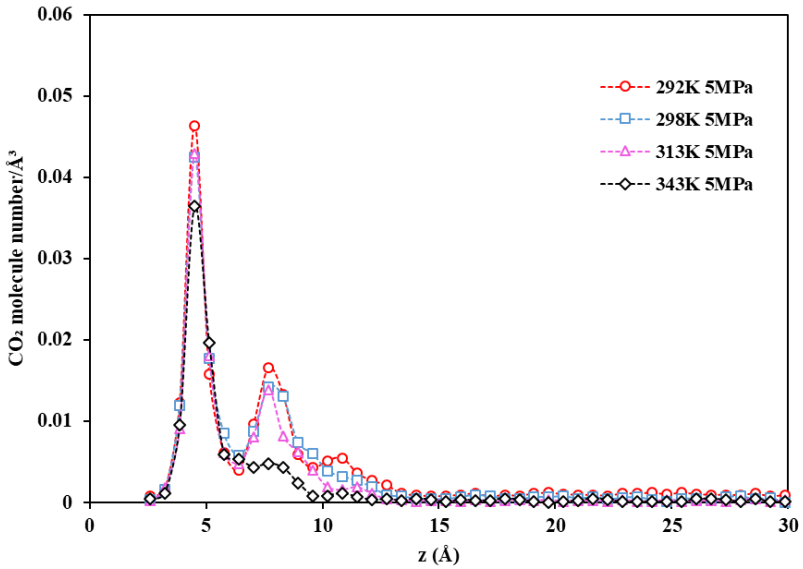

Figure 4. 6 Density profiles of CO_2 molecule number per Å³ along the *z*-axis with CO_2 pressure of 5 MPa at various temperatures.

4.3.2 Water contact angles as a function of CO_2 pressure at a reservoir temperature

Water contact angles on shale are determined at a reservoir temperature as a function of CO_2 pressure and results are compared with experimental data in **Figure 4.7** [58,62]. The water contact angle is determined as 97.5° ± 2° at a CO_2 pressure of 5 MPa and increases with pressure before the contact angle approaches 180° at 20 MPa. There is a discrepancy between our simulation data and experimental data, which is attributed to different TOC contents of the organic shale. However, the same trend is obtained that water contact angles increase with an increase in pressure. Additionally, both the experiment and simulation results show that the wettability behavior of the CO_2-water-shale system turns from a neutrally-wet state to a CO_2-wet state at the pressure value that corresponds to the critical pressure of CO_2. This implies that the subcritical and supercritical conditions are of great importance for the determination of water contact angles. When CO_2 is at

a supercritical condition, it acts like both liquid and vapor and its density difference from water is becoming smaller [70]. Therefore, influencing factors such as the strong intermolecular interactions between CO_2 and solids, and a small density difference from water contribute to a CO_2-wet condition in the system. The same trend of the brine contact angles in the CO_2-brine-quartz system was observed in both experiments and molecular dynamic simulations [163,177].

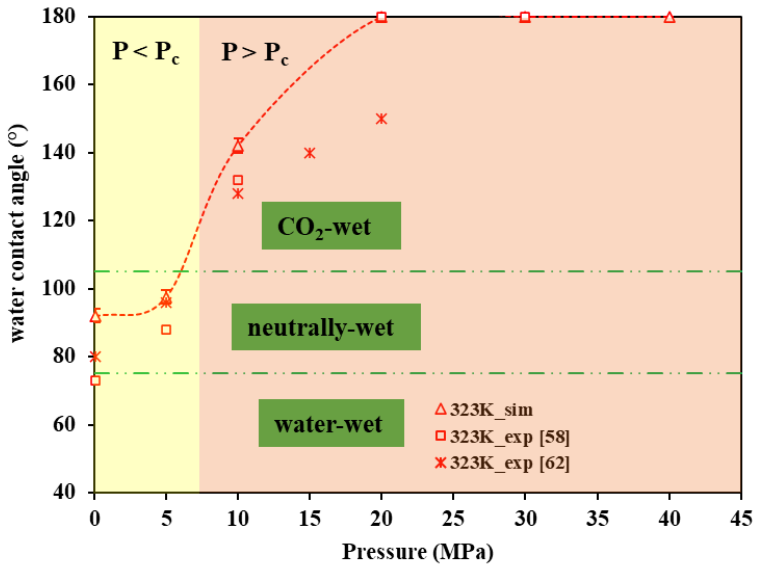

Figure 4. 7 Water contact angles on the graphene surface as a function of pressure at 323 K compared with experimental data [58,62]**.**

It is interesting to find that the absolute adsorption amount of CO_2 on organic matters in shale such as kerogen rises to a maximum value when gas pressure is around 7.37 MPa, which corresponds to the critical pressure of CO_2 [178]. When gas pressure increases beyond the critical pressure value, the adsorption amount remains almost constant. This is attributed to changes in the affinity between CO_2 and organic matters around the critical pressure. A strong affinity can not only contribute to a more CO_2-wet system but also a large adsorption amount of CO_2. However, there

is no direct relationship between CO_2-wettability of organic matters in shale and CO_2 adsorption amount. It can still be observed that a CO_2-wet condition in the system favors adsorption of CO_2 on organic matters in shale. As is known, low pressure contributes to a secure residual and structural trapping of CO_2 in a saline aquifer [177]. However, the adsorption mechanism plays a significant role in CO_2 sequestration of a depleted shale reservoir. The adsorption amount is also strongly influenced by pressure, and high pressure can enhance the adsorption amount to some extent. Therefore, pressure should be determined with consideration in terms of security of trapping and storage capacity.

4.3.3 Brine contact angles as a function of salinity and ion types

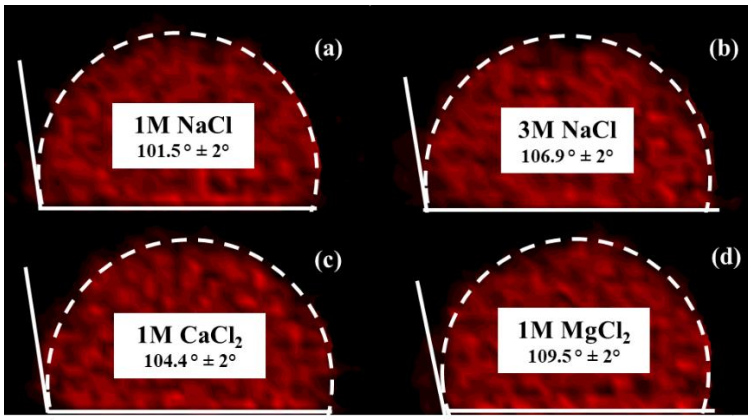

Figure 4. 8 The brine droplets on the graphene surface with different salinity or ion types at 323 K and 5 MPa.

The effects of salinity and ion types on brine contact angles on the graphene surface are investigated by considering brine droplets with the salinity of 1M NaCl, 3M NaCl, 1M $CaCl_2$ and 1M $MgCl_2$. The contact angles increase slightly from 97.5° ± 2° to 101.5° ± 2° and 106.9° ± 2° for 1M NaCl and 3M NaCl aqueous solutions, respectively (**Figure 4.8**). As expected, the main peak of water molecules in the density profile along the *z*-axis is weakened by an increase in the salinity

and a marginal increase in the height of the droplets along the *z*-axis can be observed in **figures 4.9** and **4.10**. This finding is similar to results in the literature: the water contact angles on quartz, shale, mica and other minerals in the CO_2 atmosphere increase with an increase in brine salinity [58,66,179,180].

The ion types also have a minor impact on the brine contact angle in the CO_2-brine-shale system. The contact angle for droplets with $MgCl_2$ is larger than those for droplets with $CaCl_2$ and NaCl. Additionally, the divalent cations such as Mg^{2+} and Ca^{2+} increase the brine contact angle compared to the monovalent cations Na^+ for the same salinity. As shown in **figures 4.9, 4.11** and **4.12**, the ions are accumulating inside the droplets instead of adsorbing directly on the surface. Mg^{2+} ions can approach the surface closer than Na^+ and Ca^{2+}, and the ion density for Mg^{2+} is the highest close to the surface among these three types of ions. This indicates that Mg^{2+} ions have a stronger affinity for a shale surface than Na^+ and Ca^{2+}, which is confirmed by some literature data [181–184]. With the adsorption of ions on a solid surface, the surface charge of the solid becomes more positive, which induces a more positive zeta potential of the solid [181]. Stronger adsorption of Mg^{2+} on the shale surface is determined by some experiments, and the zeta potential for Mg^{2+} is more positive than that for Na^+ and Ca^{2+} [183,184]. Experiments also illustrate that the zeta potential can turn from negative to positive at a low concentration of Mg^{2+} [184]. In contrast, a higher salinity is required to achieve a non-positive zeta potential for Ca^{2+}. For Na^+, the effects of ions on the brine contact angles are not obvious due to its low ionic strength and weak adsorption ability on a shale surface [185,186]. A similar phenomenon is also observed in a CO_2-brine-quartz system in MD simulations: brine contact angles increase with the increasing ionic strength and the quartz surface becomes less water-wet [187,188].

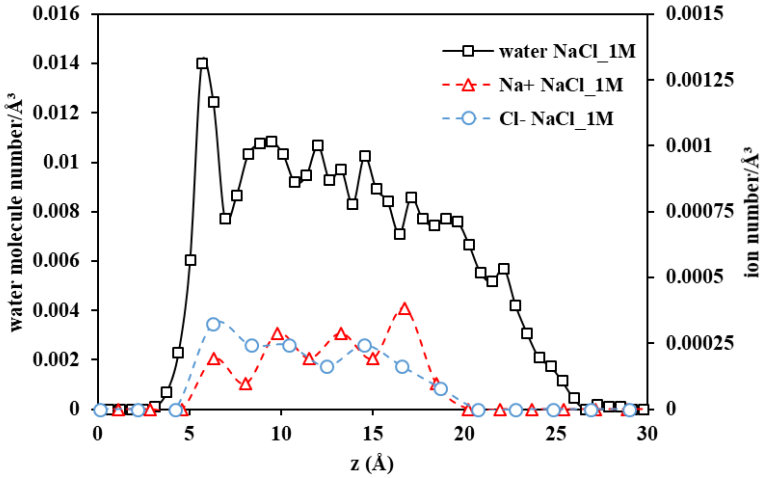

Figure 4. 9 Density profiles of water molecule number and ion number per Å³ along the *z*-axis at 323K and 5 MPa for brine droplets of 1M NaCl.

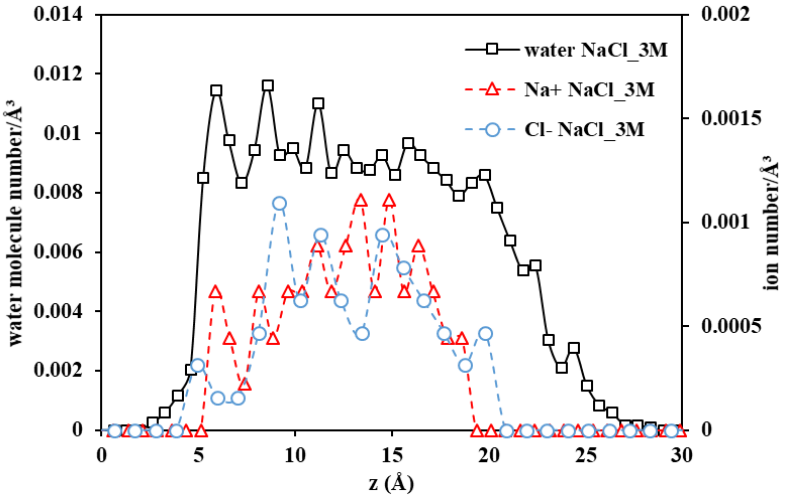

Figure 4. 10 Density profiles of water molecule number and ion number per Å³ along the *z*-axis at 323K and 5 MPa for brine droplets of 3M NaCl.

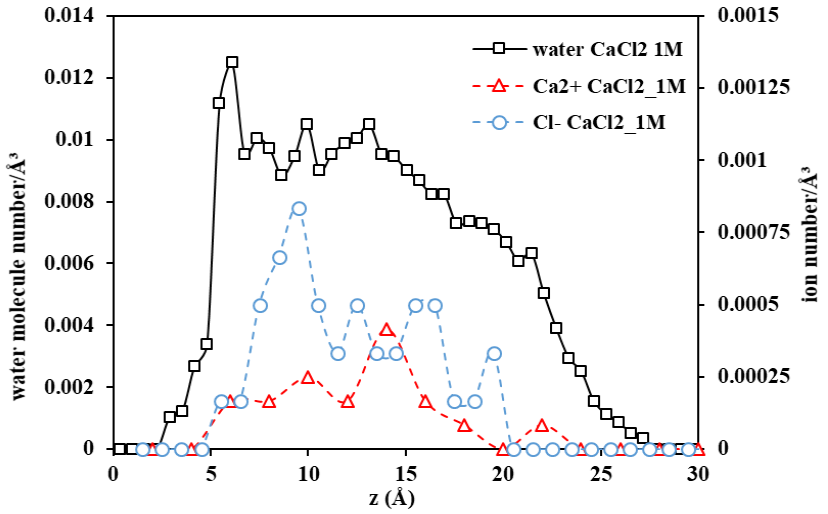

Figure 4. 11 Density profiles of water molecule number and ion number per Å³ along the *z*-axis at 323K and 5 MPa for brine droplets of 1M $CaCl_2$.

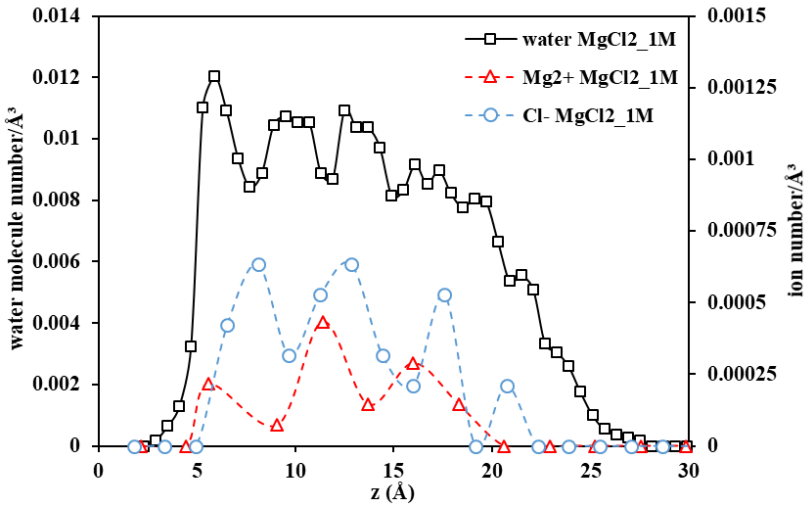

Figure 4. 12 Density profiles of water molecule number and ion number per Å³ along the *z*-axis at 323K and 5 MPa for brine droplets of 1M $MgCl_2$.

4.3.4 Water-CH_4/CO_2-shale organic matter contact angles

The rock wettability in the atmospheres of CO_2 and CH_4 mixtures is also of great significance for CO_2 storage and enhanced gas recovery in shale gas reservoirs. By varying the numbers of CO_2 and CH_4 molecules in the simulation box, we obtain gas mixtures with different CH_4 fractions and

maintain the gas pressure at 20 MPa. As shown in **Figure 4.13**, the water contact angle decreases with an increase in the mole fraction of CH_4. The graphene is completely CO_2-wet at 323 K and 5 MPa. However, the water contact angle decreases to 133.5° ± 2° in the environment of CH_4, and the wettability turns to a moderately gas-wet condition.

The reduction of the water contact angle with an increasing CH_4 mole fraction is consistent with simulation data on Q^3 silica [73]. Additionally, according to some experiment results [58], water contact angles in CH_4-brine-shale systems are lower than those in CO_2-brine-shale systems. The interfacial tensions of gas/water are also influenced by a mole fraction of CH_4, and values of interfacial tensions increase with the increasing mole fraction of CH_4 [71,72]. Based on Young's equation, an increase in the water contact angle is caused by the interplay of the interfacial tension difference between gas-solid and water-solid with the gas-water interfacial tension:

$$\cos\theta = \frac{\gamma_{gas-solid} - \gamma_{water-solid}}{\gamma_{gas-water}} \tag{4.6}$$

where $\gamma_{gas\text{-}solid}$ is the interfacial tension of solid-gas, $\gamma_{water\text{-}solid}$ is the interfacial tension of solid-water, $\gamma_{gas\text{-}water}$ is the interfacial tension of water-gas, and θ is the water contact angle.

Generally, a graphene surface is hydrophobic [169–171], and thus the $\gamma_{gas\text{-}solid}$ - $\gamma_{water\text{-}solid}$ is negative. As more CH_4 is added into pure CO_2, the interfacial tension between gas mixtures and water increases. It is because the attractive force between CH_4 and water is smaller than that between CO_2 and water, and the added CH_4 will decrease the attractions between gas mixtures and water, leading to a higher apparent interfacial tension. We note that the interfacial tension between water and solid $\gamma_{water\text{-}solid}$ can be assumed constant and the interfacial tensions between gas-solid

do not vary too much for CO_2/CH_4 gas mixtures [163,189,190]. Therefore, the value of cos θ increases and the water contact angle decreases correspondingly.

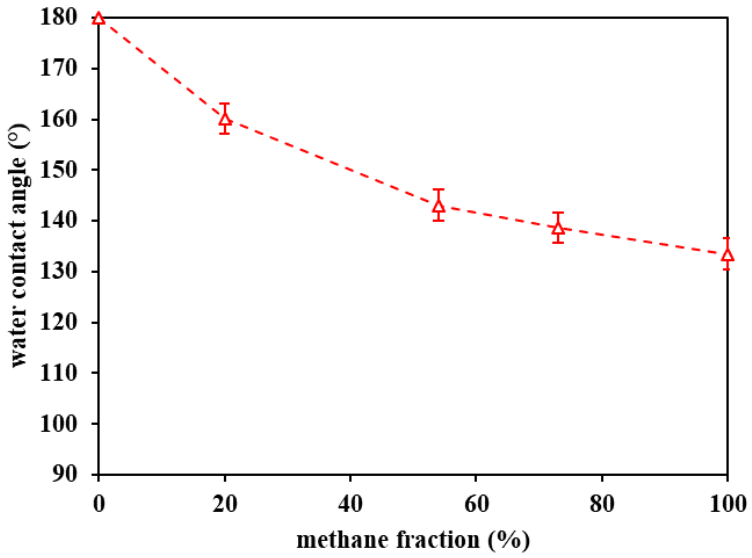

Figure 4. 13 Water contact angles as a function of CH_4 fraction at 323 K and 20 MPa.

Figure 4.14 displays the density profiles of CO_2 and CH_4 molecule numbers per Å^3 along the *z*-axis at 323K and 20 MPa. In a system with pure CO_2 or CH_4, gas molecules accumulate close to the solid surface and form a peak in the density profiles. The maximum molecule number per Å^3 for CO_2 is around 0.037 which is about 1.3 times that for CH_4. In a system containing CO_2 and CH_4 with a nearly even mole fraction, the maximum CO_2 molecule number per Å^3 is approximately 2.7 times that for CH_4. Based on **Figure 4.14**, the graphene surface is found to have a stronger affinity for CO_2 than CH_4 and the organic matter in shale is more CO_2-wet. Some scholars investigated the competitive adsorption of CO_2/CH_4 in shale or coal bed and found that the CO_2/CH_4 adsorption selectivity on shale or coal bed is 1.1-9.1, which is dependent on factors such as pressure, temperature and the content of organic matters in minerals [93,157,178,191,192]. As

a wetting phase in organic matters in shale, CO_2 usually takes up small pores in reservoirs and it is more uniformly distributed in the micropores in shale reservoirs. Then the displacement of CH_4 towards a production well is improved [191]. Therefore, the adsorbed CH_4 in shale reservoirs can be easily displaced by CO_2, and a larger amount of CO_2 can be stored as the adsorbed phase in the meanwhile.

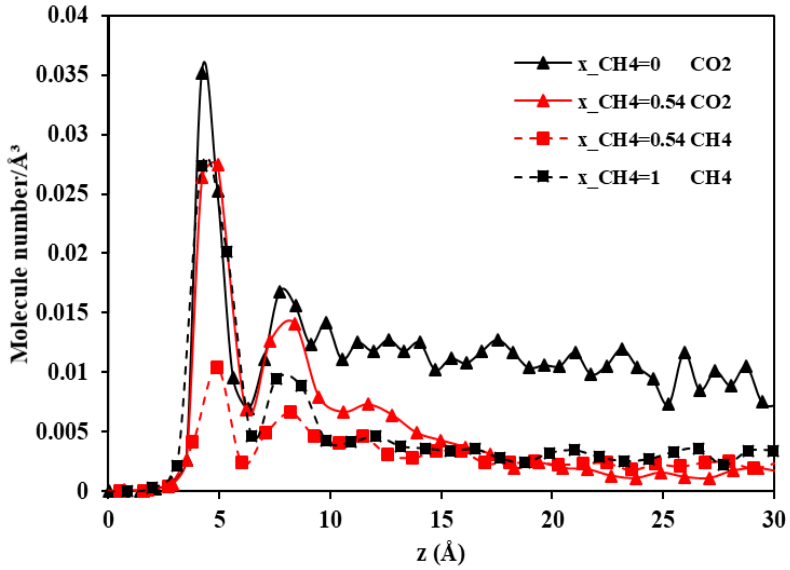

Figure 4. 14 Density profiles of CO_2 and CH_4 molecule number per Å³ along the *z*-axis at 323K and 20 MPa with different CH_4 fractions.

4.3.5 Implications and limitations

Implications for CS-EGR

In this chapter, the effects of temperature, pressure, salinity, and gas contents on water/brine contact angles in the CO_2/CH_4-shale systems are investigated, which has a significant impact on the CS-EGR processes in shale formations. The implications for CS-EGR will be discussed in this section.

According to our results, the water contact angles on an organic pore surface of shale are larger than 90° and CO_2 is a wetting phase in the system, which is unfavorable for structural and residual trapping of CO_2 [177]. Note that we use a graphene film to represent the surface of organic matters in shale in our simulation, but a shale surface in a formation has a lower TOC and it is more hydrophilic. However, the effects of temperature and pressure illustrated in this study can still be applied to the surfaces of organic matters in a shale reservoir. The system becomes more CO_2-wet as pressure increases to a critical pressure value or temperature decreases, which indicates a stronger interaction between CO_2 and shale. As described before, the adsorption amount of CO_2 increases to a maximum value and reaches a plateau when pressure rises to a value around the critical value (7.37 MPa) [178]. Moreover, the adsorption amount is also strengthened at low temperatures. Therefore, both the trapping and adsorption mechanisms should be considered by optimizing the pressure and temperature when CO_2 is stored in a depleted shale reservoir. While structural and residual trapping mechanisms are pertinent to CO_2 sequestration in carbonates or sandstones, the dominant storage mechanism in shales is adsorption trapping and the same applies to coals [75,109,178,191,193,194].

Additionally, the water contact angle on a shale surface in the atmosphere of CO_2 is larger than that in the atmosphere of CH_4, and thus the shale surface has a strong affinity for CO_2 and the CO_2 adsorption capacity is higher than CH_4 adsorption capacity. As a wetting phase in a reservoir, CO_2 is distributed more evenly in micropores in shale reservoirs and the displacement efficiency of CH_4 is improved. Moreover, the CO_2/CH_4 adsorption selectivity on shale is influenced by factors including pressure, temperature and the content of organic matters in minerals [93,157,178,191,192]. The contents of organic matters are determined by minerals in the

reservoirs, and the injecting timing of CO_2 and temperature of injected CO_2 can be optimized to improve the displacement efficiency.

Limitations

A graphene sheet is used to represent the surface of organic matters in shale without considering the effects of the TOC contents and the surface roughness. High TOC contents in shale can result in an increase of water contact angles and a system tends to be CO_2-wet with an ultrahigh TOC content [62]. Additionally, the surface roughness also has an effect on the water contact angle and a water contact angle was found to decrease with an increase in roughness in CO_2-brine-quartz/calcite systems [17,20,32]. Thus, these impacting factors are significant for investigation of wettability in reservoirs.

4.4 Summary

In this chapter, we have investigated the water/brine contact angles in the CO_2/CH_4-shale organic matters systems at the reservoir conditions using MD simulation. The effects of temperature, pressure, brine salinity, ion types and gas contents on the water contact angles have been explained in detail and the implications for CO_2 sequestration and enhance gas recovery have also been clarified. Based on our simulation results, some conclusions are reached as follows:

1. When temperature is below CO_2 critical temperature, an increase in contact angle with temperature is greater than that above the critical temperature. Additionally, temperature has a more significant effect on the water contact angle under an intermediate-pressure condition than a high-pressure condition.

2. The water contact angles increase as pressure grows until approaching 180°. The wettability behavior of a CO_2-water-shale organic matter system turns from a neutrally-wet state to a CO_2-wet state approximately at the critical pressure of CO_2. Changes in the affinity between CO_2 and organic matters around the critical pressure lead to a more CO_2-wet condition and a large CO_2 adsorption capacity in the system.
3. The salinity and ion types have a minor impact on the brine contact angle in a CO_2-brine-shale system. A slight increase in the water contact angle is observed with increasing salinity. Additionally, an increase in the brine contact angle caused by the divalent cations such as Mg^{2+} and Ca^{2+} is larger compared to the monovalent cations Na^{+} with the same salinity. A high ionic strength and strong adsorption ability of ions can result in large brine contact angles.
4. The water contact angle decreases with an increase in the CH_4 mole fraction of a CO_2/CH_4 mixture. The organic matter in shale has a stronger affinity for CO_2 than CH_4 which contributes to a more CO_2-wet system and a higher CO_2 adsorption capacity than CH_4. Furthermore, the displacement of efficiency of CH_4 is improved by injection of CO_2.

Chapter 5 Suitable experimental conditions for determination of void volume by helium expansion tests

5.1 Introduction

A void volume, which is measured by helium expansion tests and used in the calculation of methane adsorption amounts, is always overestimated due to helium adsorption. In this study, by comparing void volumes of carbon nanopores determined under different temperatures and pressures using GCMC simulation, suitable experimental conditions for helium expansion tests are obtained. Five volumes, including one apparent volume V_{app}, three referred volumes V_{ref} and one physical volume V_{phy}, are recognized. The apparent volume V_{app} corresponds to the volume directly determined under traditional experimental conditions, while three referred volumes are determined at 500 K with different pressure ranges (low, moderate, high). The physical volume is calculated by multiplying a pore width and a surface area. Besides, a volume determined by using a helium probe is named an accessible volume V_{acc} and used as a criterion for a determined volume through mass balance. It is found that use of a void volume determined under traditional experimental conditions or a physical volume leads to negative excess adsorption amounts at high pressures. Considering an economic effect and measurement accuracy, determining a void volume by helium expansion tests within a moderate pressure range at 500 K is suggested. Excess isotherms of methane calculated by the suggested volume are more appropriate and of great physical meanings for further investigation of adsorption mechanisms.

The remainder of this chapter is organized as follows: In Section 5.2, six volumes determined under various conditions are defined. In Section 5.3, we illustrate the pore model, force field and methodology in our GCMC simulation. The local density profiles of helium and methane in pores are compared and then the bulk and total densities of helium are investigated in Section 5.4. We also investigate both helium and methane adsorption in carbon nano-slit pores with various pressures and temperatures and demonstrate the effects of an overestimation of a void volume on adsorption isotherms. In Section 5.5, some key findings and implications are summarized.

5.2 Definition of volumes

The total void volume of pore for calculating the excess adsorption amount is always measured by helium expansion tests. We conduct GCMC simulations for helium adsorption in nanopores to simulate a helium expansion experiment in this chapter and we use the equation (2.2) to calculate the excess adsorption amount in nano-slits. Helium is regarded as non-adsorbed gas and there will be no excess adsorption under any conditions. Then we can obtain the total void volume determined by helium expansion tests:

$$V_t' = N_t \cdot M/\rho_b \tag{5.1}$$

where M is the molar mass of gas, N_t is the total loading amount which can be determined in GCMC simulation, and ρ_b is the bulk density.

However, as described before, helium adsorption has been detected in carbon and has an effect on determining the total void volume. To investigate the adsorption effect on the total void volume determination, we combine the equations (2.1b) and (5.1) and obtain the deviation:

$$\delta V_t = V_t' - V_t \tag{5.2a}$$

$$\delta V_t = {N_a \cdot M}/{\rho_b} - {N_a \cdot M}/{\rho_a} \quad (5.2b)$$

$$\delta V_t = {N_a(\rho_a - \rho_b)M}/{(\rho_a \cdot \rho_b)} \quad (5.2c)$$

Under any conditions, δV_t is positive as the density of the bulk phase is always smaller than the adsorbed density. When δV_t approaches zero, the adsorbed phase density is comparable to the bulk phase density and the adsorption effect on the volume determination can be neglected. Under this circumstance, a void volume can be obtained by the equation (5.1) with high accuracy and all the gas molecules in pores can be treated as the bulk phase. To obtain the suitable experimental conditions for helium expansion tests, the total density ρ_t is compared with the bulk phase density. The total density can be given by

$$\rho_t = {N_t}/{V_t} \quad (5.3a)$$

$$\rho_t = {(\rho_a \cdot V_a + \rho_b \cdot V_b)}/{(V_a + V_b)} \quad (5.3b)$$

$$\rho_t = {\rho_b \cdot (\frac{\rho_a}{\rho_b} V_a + V_b)}/{(V_a + V_b)} \quad (5.3c)$$

These three density values are almost the same ($\rho_a \approx \rho_t \approx \rho_b$, $\rho_a > \rho_t > \rho_b$) under desired conditions, which is suitable for helium expansion tests.

Table 5. 1 Various conditions for the void volume determination of carbon slits by helium expansion tests.

Volume	Temperature (K)	Pressure (MPa)
V_{app}	300	0.69 to 15
V_{ref_L}	500	0.1 to 1

V_{ref_M}	500	1 to 10
V_{ref_H}	500	≥ 200

In this chapter, we use various pore void volume values to calculate excess isotherms. An apparent volume value V_{app} is determined under the traditional experimental conditions [195,196]. Three referred volume values (V_{ref_L}, V_{ref_M}, $V_{ref\_H)}$ are obtained under the conditions shown in **Table 5.1**. We also obtain an accessible void volume V_{acc} by Poreblazer developed by Sarkisov and Harrison [197] using a helium probe (46104.65 $Å^3$). Additionally, a physical void volume of pores V_{phy} is obtained by simply multiplying the pore width H and surface area A (53973.6 $Å^3$).

5.3 Methodology and model

A configuration of helium and methane adsorbing in nanometer slit-like pores is adopted since slit-shaped pores are one of the main components in the nanoscale pore systems of shales [198]. The adsorbents in the system are composed of two parallel graphite walls (**Figure 5.1**) and the adsorbates will fill this pore. Three-dimensional periodical boundary conditions are applied in the simulation cell. The dimensions of the simulation box in the x and y directions are 51.6 Å and 52.3 Å, respectively. A distance of 20 Å between the inner surfaces of the pore walls in the z-direction is defined as the pore width. The inter-pore interactions are assumed to be negligible [199].

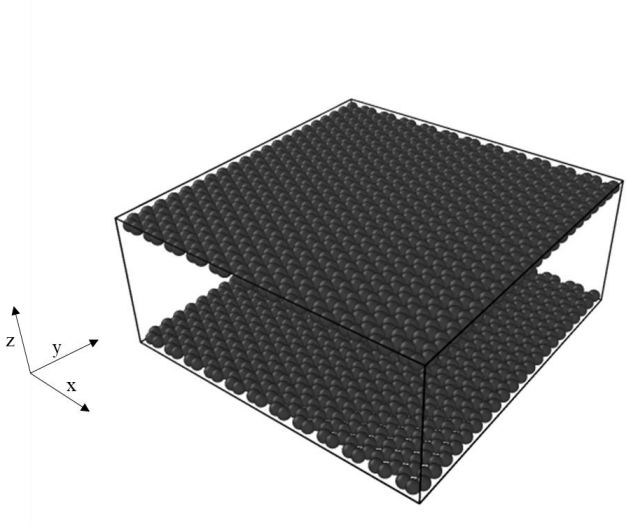

Figure 5. 1 Schematic of a carbon slit pore.

In an adsorption system, adsorption is controlled by adsorbate-adsorbent interactions and adsorbate-adsorbate interactions, and the van der Waals force and Coulomb force play important roles. Intermolecular interactions are calculated by a pairwise additive Lennard-Jones (LJ) 12-6 function, and the Lorentz-Berthelot mixing rule is used to calculate cross interaction parameters for unlike pairs. The interaction between the charged sites is calculated by equation (3.22).

The parameters for calculating interactions between helium atoms are obtained from Hirschfelder et al. [200] and consistent valence force-field (CVFF) is used to describe the interactions between methane [160]. To reduce the simulation time, nano-slit pores and adsorbates are treated as rigid structures.

GCMC simulations are performed for helium at the temperatures of 100, 300 and 500 K and the pressure ranges from 0.01 to 1000 MPa, respectively. Additionally, methane adsorption on nano-slit pores is investigated at 323 K on a 20 Å nano-slit pore with pressure ranging from 0.1 to 60 MPa. We conduct a total of 5e+6 GCMC moves in each GCMC simulation. The system

temperature is controlled by a Nosé-Hoover thermostat, and the Verlet algorithm is used for solving Newton's equations of motion. Each simulation is conducted for 10 ns with a timestep of 1 fs. We use the first 5 ns to achieve an equilibrated state in the system and another 5 ns to calculate excess adsorption amounts.

5.4 Results and discussion

In this section, density distributions of helium atoms in nano-slits at various temperatures and pressures are first introduced, and effects of temperature and pressure on a local density profile are clarified. Then we compare a bulk density in our simulation with the values from the NIST database to validate the accuracy of the simulation method. We also determine a void volume of pores with different temperatures and pressures by GCMC simulation to achieve suitable experimental conditions for helium expansion tests. Helium adsorption isotherms calculated by different void volumes are compared and the effects of using an overestimated void volume on methane adsorption are discussed.

5.4.1 Density distribution in nano-slits pores

A helium distribution in the center of a carbon slit pore at 100 K with the gas pressure from 1 to 1000 MPa is shown in **Figure 5.2**. It is obvious that the efficiency of molecular packing in the pore is improved with a pressure increase and this is consistent with findings by Do et al. [99]. At very high pressures, the degree of clustering of helium atoms is also very high, which is almost comparable to the helium distribution near the pore walls.

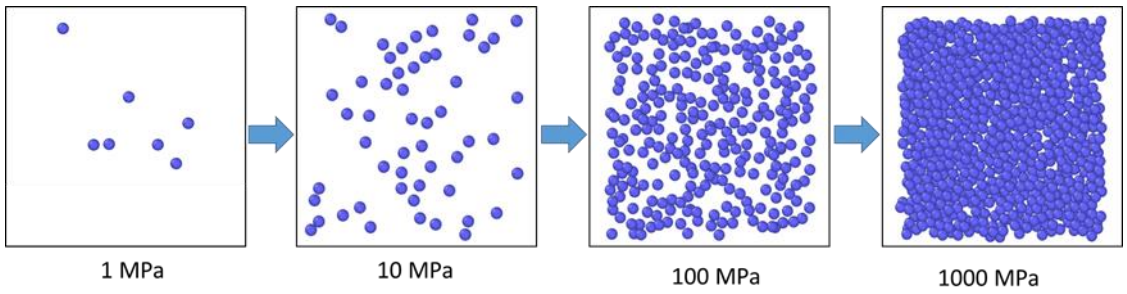

Figure 5. 2 Snapshots of helium distribution in the center of carbon slit pore at 100 K with pressure ranging from 1 to 1000 MPa.

The typical one-dimensional fluid density profiles along the *z*-direction in a carbon slit pore and the corresponding bulk density at 100, 300 and 500 K at various pressures are plotted in **figures 5.3, 5.4** and **5.5**, respectively. Taking the local density profile at 100 K as an example, the following observations can be made: (1) several peaks are presented in the pore. The closer to a pore wall, the higher a peak is. It indicates that helium atoms prefer accumulating near a pore wall, which is a consequence of stronger interactions between the pore wall and helium atoms compared to the interactions between helium atoms themselves. (2) The width of each peak and the distance between two neighboring peaks roughly correspond to one kinetic diameter of helium atoms. (3) At 10 MPa, there are only two distinct peaks near the pore walls and the density near the center of the pore fluctuates around the value of the bulk density. It turns out that helium atoms fall into the bulk phase because of the weak attraction from the pore walls in the center of the pore at low pressures. High pressure can enhance the organization and alignment of helium atoms in the pore as more peaks can be packed at 1000 MPa. (4) The local density in the pore is not always larger than the bulk density. The adsorbed layer is assumed as the combined space of the closest peak and valley to a pore wall, and the valley part below the bulk density is smaller at 100 MPa and almost vanishes at 10 MPa, so the averaged density of the adsorbed phase is larger than the bulk

density. However, the valley parts between the peaks are enhanced at a higher pressure, and then the peak part above the bulk density at 1000 MPa makes up for the valley part, resulting in the adsorbed density comparable to the bulk density.

To investigate the effects of temperature on a local density distribution in the pore, the local density profiles at 1000 MPa are plotted with various temperatures in **Figure 5.6**. Generally, the density in the pore decreases as temperature increases. At a higher temperature, the particles have more kinetic energy and then move faster, leading to a decrease in density. In addition, a higher thermal motion of particles at high temperatures makes helium atoms less organized and aligned, which is in accordance with the effects of temperature on CO_2 adsorption on carbon-slit pores [153]. The density distribution in the center of a pore is far from uniform at 100 K, while helium atoms are more uniformly distributed in the center at 300 and 500 K.

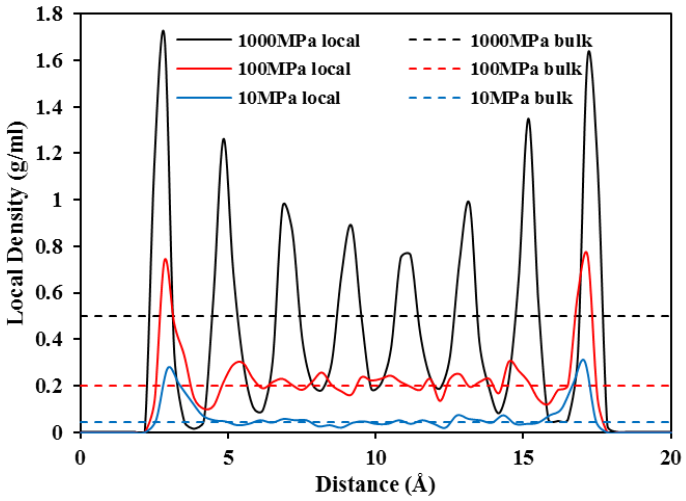

Figure 5. 3 Local density profile versus distance at 100 K with pressure ranging from 10 to 1000 MPa.

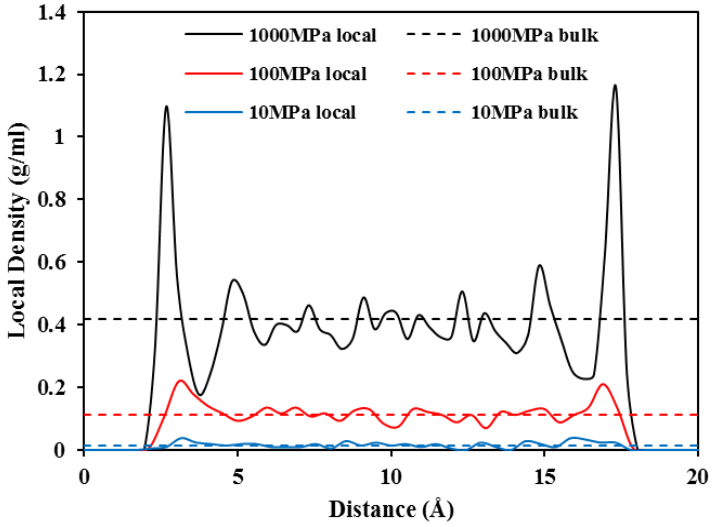

Figure 5. 4 Local density profile versus distance at 300 K with pressure ranging from 10 to 1000 MPa.

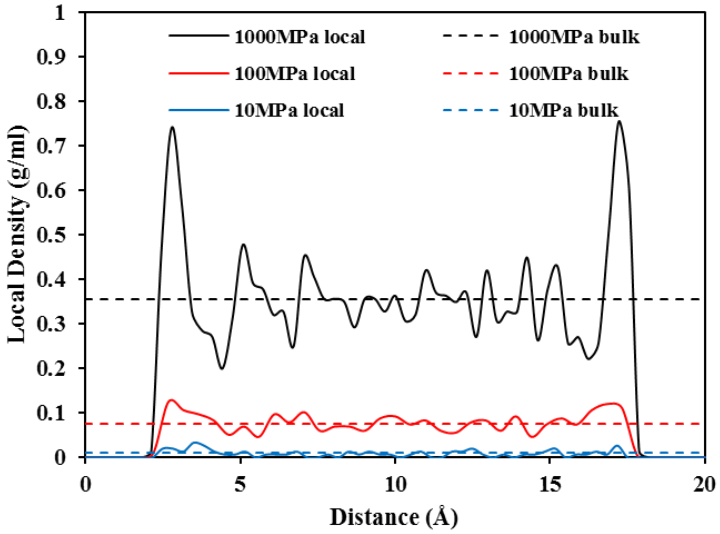

Figure 5. 5 Local density profile versus distance at 500 K with pressure ranging from 10 to 1000 MPa.

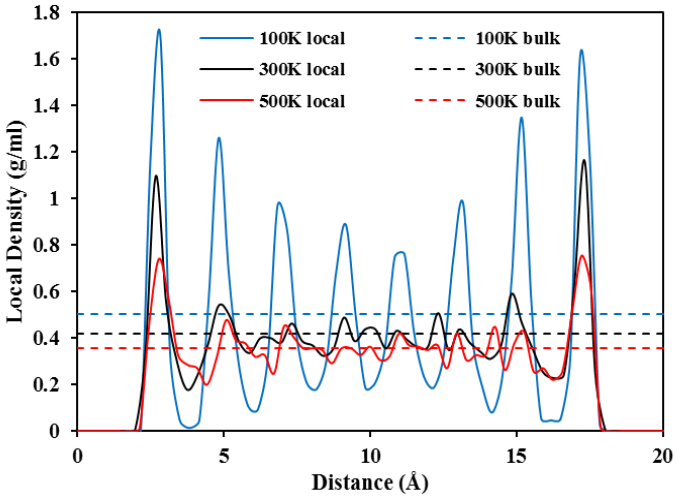

Figure 5. 6 Local density profile versus distance at 1000 MPa at different temperatures.

5.4.2 Void pore volume calculation

Total density and bulk density

The accessible void volume of a pore is employed for calculating the total density by the equation (5.3a). **Figure 5.7** shows the total and bulk densities as a function of pressure in our simulation and compares the bulk density values with the NIST database within the pressure ranging from 0 to 100 MPa. The discrepancy between the bulk and total densities is also shown in **Figure 5.7**. Generally, the simulated bulk density shows an excellent agreement with the NIST values. For 300 K, the bulk density and the total density almost overlap around 1.60e-05 and 0.418 g/ml when the gas pressure is as low as 0.01 MPa and as high as 250 MPa. The discrepancy between the bulk and total densities becomes manifest for the pressure ranging from 0.02 MPa to 250 MPa. According to equations (5.2) and (5.3), the adsorption effect on the volume determination can be only negligible when the total density is comparable to the bulk phase density. Thus, the suitable pressure for void volume determination at 300 K lies in an extremely low or high-pressure range.

Under these conditions, the adsorption effect on the determination of a void volume can be mitigated and the accuracy of this determination can be improved. A similar trend to that at 300 K for the bulk and total densities has been observed at 500 K. Unlike 300 K, these two densities almost coincide at a lower pressure value of 1 MPa, which suggests a wider suitable pressure range for void volume determination at 500 K. The low-pressure range which is suitable for void volume determination cannot be witnessed at 100 K due to the strong adsorption effect even at a pressure of 0.01 MPa. The bulk density curve merges with the total density curve when the gas pressure reaches up to 300 MPa. The density difference between 100, 300 and 500 K is getting smaller with an increase in the gas pressure.

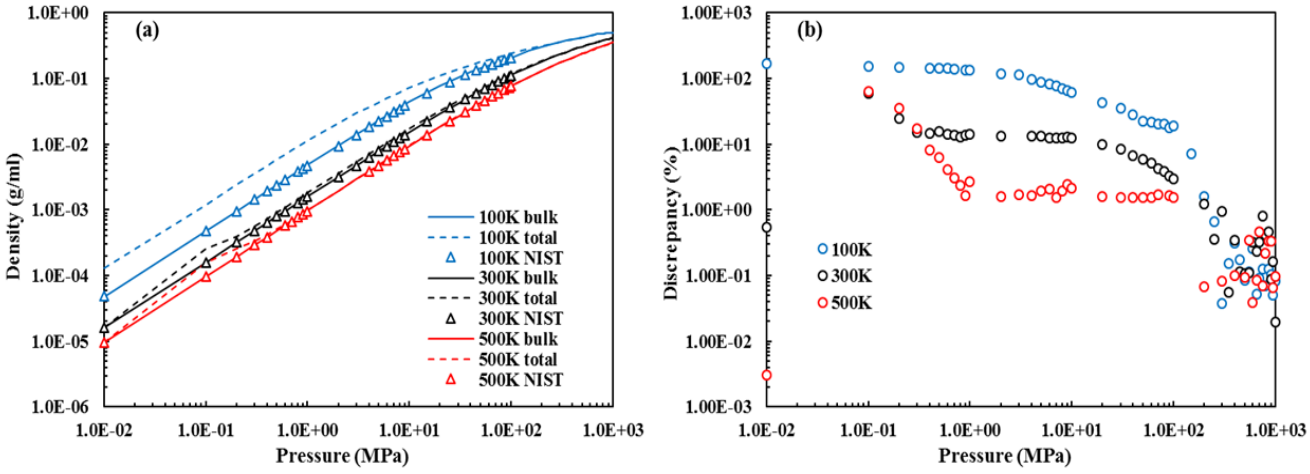

Figure 5. 7 The bulk density and total density of helium in a carbon slit pore at 100, 300 and 500 K compared with the NIST database as a function of pressure (a); the discrepancy between the bulk and total densities as a function of pressure (b).

Void volume measurement

The calculated void volume of a carbon slit pore by the equation (5.1), where helium is assumed to be non-adsorbed gas, and the relative error between the calculated value and accessible void

volume are illustrated in **Figure 5.8**. At 100 K, the determined void volume value decreases with the increasing pressure as the bulk and total density difference is getting smaller, and finally stabilizes around 46160.87 $Å^3$ when pressure is above 300 MPa. At 300 K, the calculated void volume values are more accurate at a pressure of 0.01 MPa or higher than 250 MPa. When the gas pressure is higher than 0.1 MPa, the accuracy of obtaining a void volume increases with pressure, and the relative error is rather small as the gas pressure approaches 250 MPa. The volume plot at 500 K generally shows the same trend as at 300 K, but the calculated volume value reaches a plateau at a lower pressure.

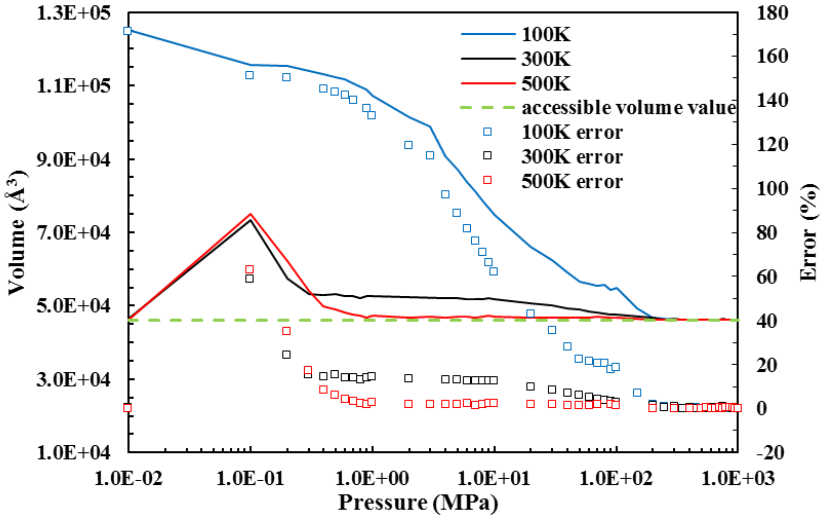

Figure 5. 8 Comparison of the accessible volume and the calculated void volume of a carbon slit pore as a function of pressure at 100, 300 and 500 K.

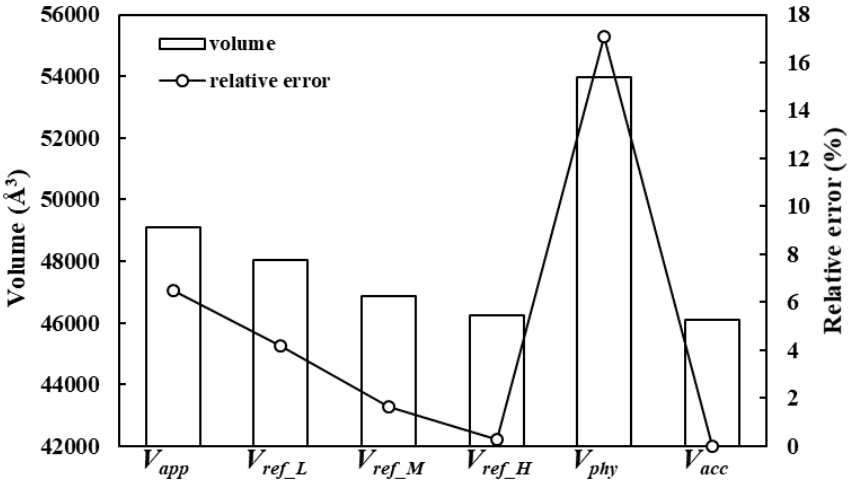

Figure 5. 9 Comparison of void volumes determined under various conditions.

Table 5. 2 Void volumes of carbon slits determined under various conditions.

Type	Description	Volume (Å^3)
V_{app}	Determined by helium tests at 300 K, 0.69 to 15 MPa	49094.32
V_{ref_L}	Determined by helium tests at 500 K, 0.1 to 1 MPa	48041.05
V_{ref_M}	Determined by helium tests 500 K, 1 to 10 MPa	46853.43
V_{ref_H}	Determined by helium tests at 500 K, ≥ 200 MPa	46232.62
V_{phy}	$H \cdot A$	53973.6
V_{acc}	determined by a helium probe	46104.65

Four volumes determined under various conditions including one apparent volume and three referred volumes are compared with an accessible volume in **Figure 5.9**, and the physical volume is also investigated. The apparent volume V_{app} determined under the traditional experimental conditions is 49094.32 Å^3 (**Table 5.2**), which is 6.5 % larger than the accessible void volume. Some scholars suggested measuring a volume at high temperatures, which can improve the measurement accuracy [103,105,106], while enough attention has not been paid to pressure

conditions at a high temperature. The referred volume determined at the gas pressure higher than 200 MPa V_{ref_H} is 46232.62 Å^3 and the relative error to the accessible value is only 0.28 %. As a suitable pressure range for void volume determination at 300 K is too high, conducting helium expansion tests under this condition consumes too much helium and is not economical. The referred volume V_{ref_L} determined at 500 K within the pressure ranging from 0.1 to 1 MPa (e.g., 0.6 MPa) is 48041.05 Å^3, which is 4.20 % larger than the accessible volume. However, V_{ref_M} obtained at 500 K within a moderate pressure range (e.g., 20 MPa) is 46853.43 Å^3, and it is more accurate than V_{ref_L}. Though V_{ref_M} still has a larger relative error compared to V_{ref_H}, the determination of a void volume under this condition is less helium-consuming and more economical. The physical void volume is always larger than the calculated pore volume value by the equation (5.1) due to the finite size of helium atoms [46,201]. Overall, it can be found that determining a void volume of carbon slit pores by a helium expansion test within a moderate pressure range (1 to 10 MPa) at 500 K is a better choice in view of the economic effect and measurement accuracy.

5.4.3 Helium adsorption analysis

In order to validate our simulation methods, the total loading amounts and the excess loading amount at 300 K in our simulation are compared with the simulation results from the literature in **Figure 5.10**. Helium adsorption on graphite nano-channels was investigated using dual control volume grand canonical molecular dynamic (DCV-GCMD) simulation [202]. The comparison shows that our adsorption data are of the same order of the magnitude and match well with the simulation data from the literature.

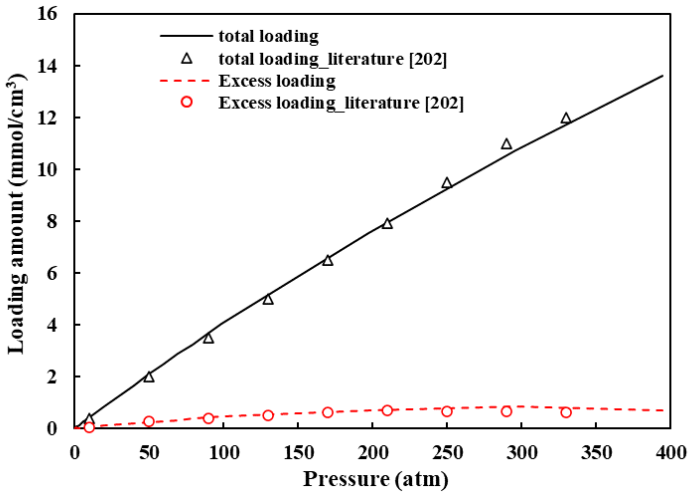

Figure 5. 10 Comparison of helium adsorption amounts with data from the literature [202]**.**

Figure 5.11 shows the total loading amount of helium at 100, 300 and 500 K with the gas pressure ranging from 0 to 1000 MPa in both the linear scale and semi-log scale. The total loading amount increases monotonically with pressure and the increasing rate becomes smaller at very high pressure. Initially, an increase in pressure can improve the possibility of the particles striking on a pore wall and then the adsorption amount is raised. When the gas pressure approaches a certain value, it will reach a point when the pressure has no effect on the adsorption rate as all the adsorption sites in the pore wall are occupied. A high temperature can decrease the total loading amount in a carbon slit pore. On one hand, helium atoms in the adsorbed phase get a sufficient amount of energy at a high temperature and detach from a pore wall. On the other hand, high temperatures can enhance the movement of helium atoms, which reduces the density of the bulk phase. At a pressure of 1000 MPa, the total loading amount of helium is 117.67, 98.27, 82.95 mmol/cm^3 for the temperature of 100, 300 and 500 K, sequentially.

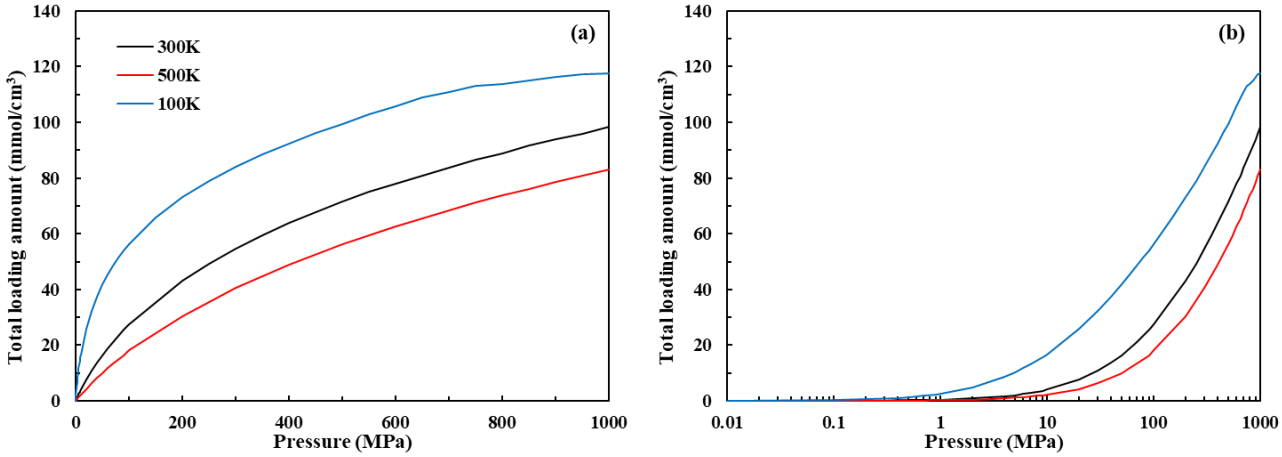

Figure 5. 11 Total loading amount at 100, 300 and 500 K with the gas pressure from 0 to 1000 MPa. (a) Linear scale; (b) semi-log scale.

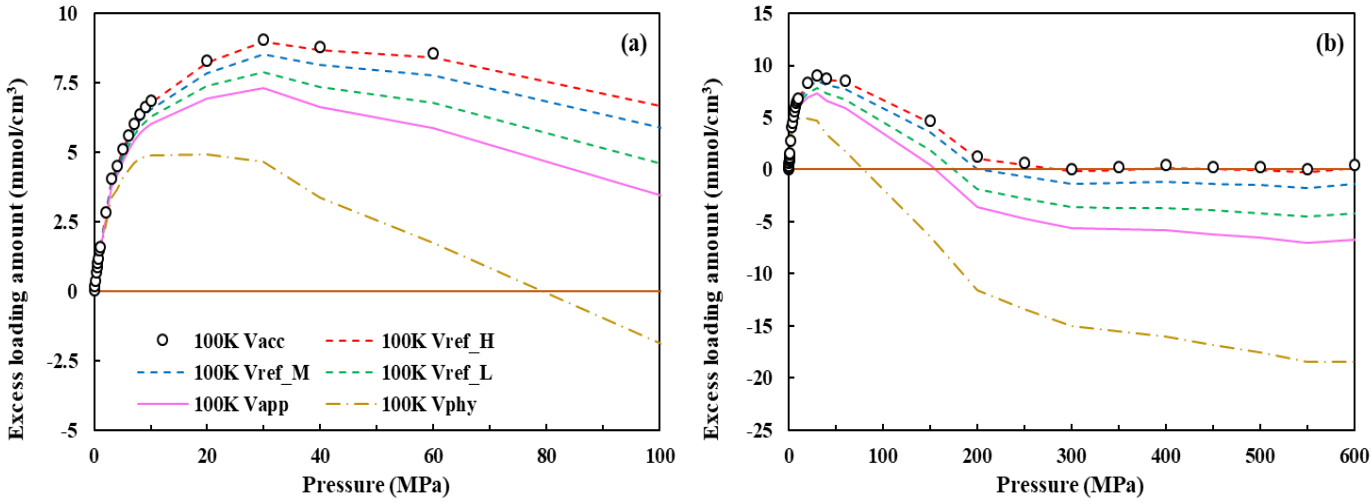

Figure 5. 12 Excess adsorption isotherms at 100 K with (a) narrow range pressure; (b) wide range pressure.

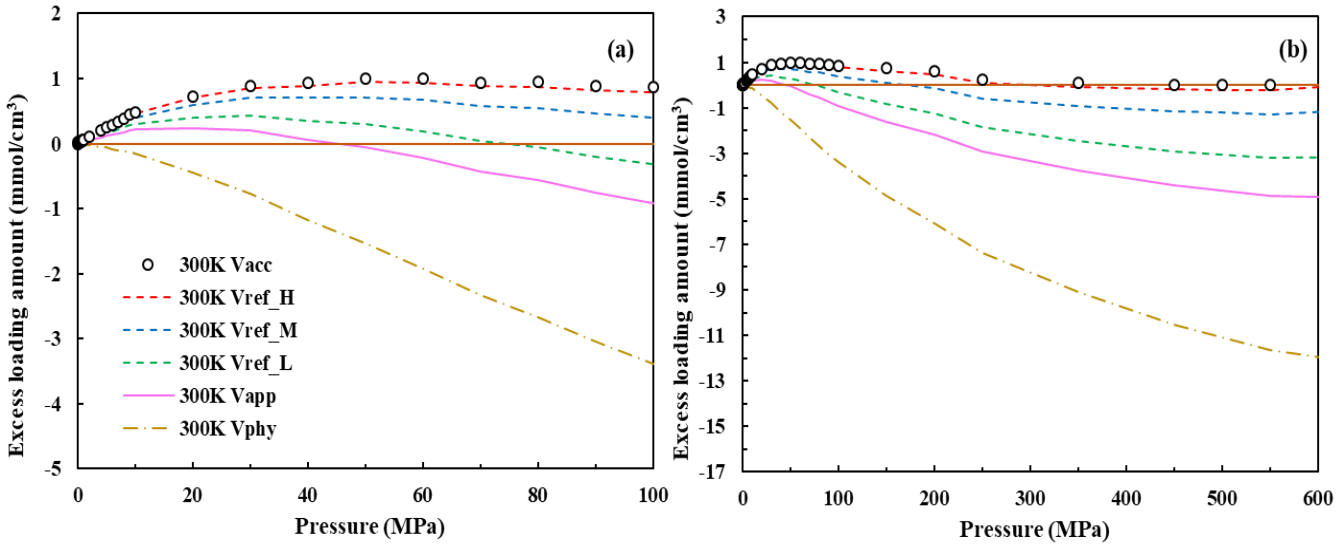

Figure 5. 13 Excess adsorption isotherms at 300 K with (a) narrow range pressure; (b) wide range pressure.

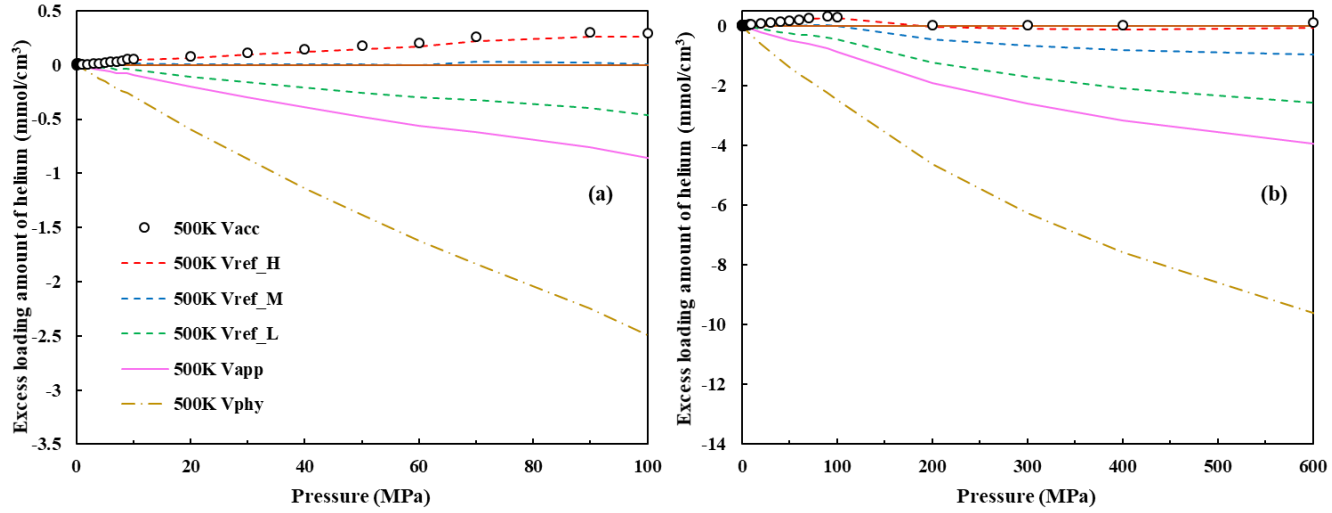

Figure 5. 14 Excess adsorption isotherms at 500 K with (a) narrow range pressure; (b) wide range pressure.

We use the six void volumes defined in Section 5.2 to calculate the excess adsorption isotherms in a carbon slit pore by the equation (2.2). The calculated excess isotherms are plotted in **figures 5.12** to **5.14** at 100 K, 300 K and 500 K versus both narrow and wide pressure ranges, respectively. In

general, an excess amount also decreases with temperature. It is not monotonically increasing with pressure and a maximum can occur when the pressure changes. Taking excess adsorption isotherms at 100 K as an example, it can be found that excess amounts remain positive except the one calculated by the physical pore volume within a narrow pressure range. The isotherm determined by the physical pore volume becomes negative when the gas pressure approaches 80 MPa. The isotherms calculated by V_{ref_H} and V_{acc} show a good agreement for both wide and narrow pressure ranges due to a small relative error between these two volumes. For a wide pressure range, the negative phenomenon is observed except the isotherm calculated by the accessible volume. The larger the estimated volume is, the earlier the negative excess adsorption happens. The isotherm calculated by the accessible volume is always positive even at extremely high pressures. Due to the additional attractive pore-wall potential, the density of the adsorbed phase is always larger than the bulk phase density to keep the equilibrium of chemical potential between the bulk and adsorbed phases. The excess isotherm is always positive if it is calculated by an appropriate pore volume (as illustrated in equations (2.1b) and (2.2). Though the relative error between V_{acc} and V_{ref_M} is 1.63 %, the excess amount turns to be negative at 250 MPa due to an overestimation of the void volume.

The shape of isotherms is more sensitive to a volume used for calculations at a high temperature. Compared to 100 K, the discrepancy between isotherms calculated by V_{ref_M} and V_{acc} becomes larger at 300 and 500 K. As the total loading amount is small at a high temperature, even though the overestimation of a void volume results in a small error in calculating gas amount in the bulk phase, the difference between the total loading amount and the gas amount in the bulk phase, which is the excess adsorption amount as defined, is significantly affected. Therefore, an accurate

estimation of a void volume is more important to generate excess isotherms at a higher temperature.

By comparison of the excess adsorption isotherms, it can be found that V_{ref_H} is the best candidate by which the calculated excess isotherms are close to the actual ones determined by an accessible volume. The isotherms determined by V_{ref_M} may not be that accurate but the physical characteristics can still be maintained at relatively low temperatures. However, the calculated isotherms for an apparent volume, a referred volume at low pressure, and a physical volume show a great discrepancy from the actual ones. In consideration of both the economic effect and the measurement accuracy, V_{ref_M} which is determined at 500 K within a moderate pressure is proposed to use for calculations of excess adsorption isotherms for helium in nano-slits.

5.4.4 Effects on methane adsorption

Methane adsorption isotherms at 323 K calculated by four different volumes are displayed in **Figure 5.15.** The total loading amounts in the 20 Å shale nano-slit and the bulk density are constant in GCMC simulations when the temperature and pressure are given. According to the equation (2.2), the excess adsorption amount is dependent on the void volume and an overestimated volume results in an underestimation of excess adsorption. Compared to the accessible volume and the referred volume determined at 500 K within a moderate pressure, using the physical volume and the apparent volume to calculate leads to a significantly smaller excess adsorption amount. The excess adsorption amounts calculated by the apparent volume become negative as the pressures approach about 54 MPa, and the isotherms calculated by the physical volume decrease to be negative at a smaller pressure value of 33 MPa.

The local density profile of methane in a nano-slit with a pore size of 20 Å is shown in **Figure 5.16**. Close to the pore walls, two peaks are displayed, which are much higher than the density in the pore center. The local gas density in the pore center fluctuates around the bulk density. Apparently, adsorption does happen in the pore at 60 MPa and the excess adsorption amount should be positive as well. The negative excess adsorption amounts calculated by the physical volume and the apparent volume are contradictory to the local density profile in **Figure 5.16**. Therefore, helium adsorption in the determination of the void volume can have a significant impact and contributes to the wrong calculation of excess adsorption isotherms. The use of the void volume determined at 500 K within the moderate range rather than the void volume determined under traditional experimental conditions is reasonable for further adsorption analysis.

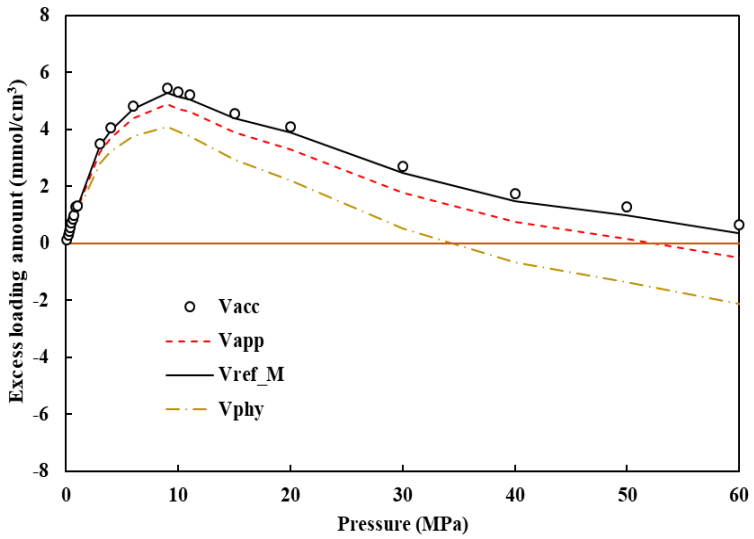

Figure 5. 15 Excess adsorption isotherms of methane on nanoslits of 20 Å at 323 K.

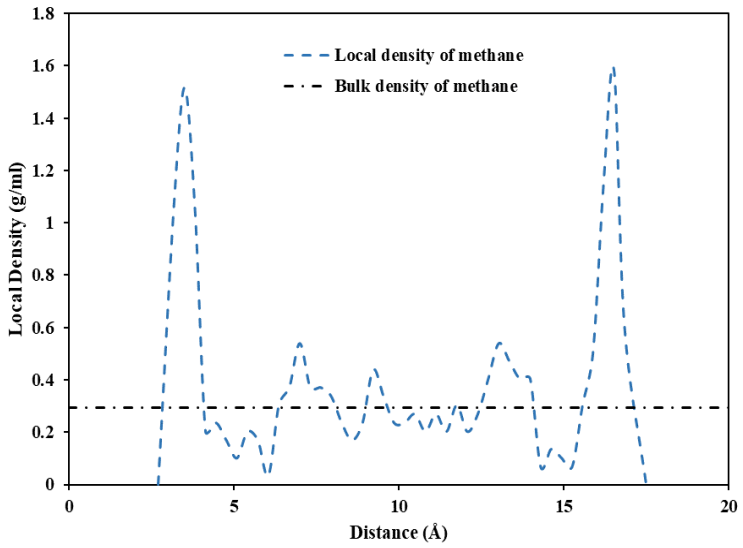

Figure 5. 16 Local density profile of methane in a nano-slit of 20 Å at 60 MPa.

5.5 Summary

Helium adsorption in traditional helium expansion tests results in an overestimation of a void volume, leading to significant errors in the calculation of methane adsorption isotherms. In this chapter, we have used GCMC simulations in LAMMPS to determine the void volume of a nano-slit and obtained suitable experimental conditions under which helium adsorption effect can be mitigated. Additionally, helium adsorption and a local density of helium atoms in a pore have been investigated. The excess adsorption isotherms calculated by volumes determined under various conditions have been also compared. From our microscopic analysis, some conclusions can be made as follows:

1. Helium adsorption effects on the void volume determination can be reduced but not totally eliminated. A void volume determined under the traditional experimental conditions (0.69 to 15 MPa, 300 K) is 6.2 % larger than an accessible one according to our results. A

physical void volume is always larger than the calculated pore volume value due to the finite size of helium atoms and the relative error is up to 17.06 %.

2. The density of an adsorbed phase can be rather close to but never smaller than the bulk density at extremely high pressure due to the existence of a strong interaction between a pore wall and adsorbates. Therefore, the isotherms calculated by an accessible volume of the same adsorbate are positive everywhere even at extremely high-pressure conditions.
3. A negative excess amount is observed at high pressures when the isotherms are calculated by overestimated void volumes and a larger overestimation leads to an earlier appearance of the negative excess adsorption phenomenon.
4. The shape of isotherms at a higher temperature is more sensitive to a volume used for calculations. Due to a small total loading amount at a high temperature, even though the overestimation of a void volume leads to a small error in calculating the amount of gas molecules in the bulk phase, the excess adsorption amount is significantly influenced.
5. A void volume determined under a moderate-pressure condition at 500 K is a reasonable candidate for excess isotherms calculation and adsorption mechanism investigation. The excess adsorption amounts calculated by the appropriate volume can result in an accurate estimation of reservoir reserves and help with establishing a practical and scientific development strategy.

Chapter 6 Methane-based volumes for methane adsorption

6.1 Introduction

An adsorbed gas amount obtained from excess adsorption isotherms is of great importance to an estimation of reservoir reserves and prediction of gas production in shale reservoirs. Generally, excess adsorption amounts are calculated by a void volume of an adsorbent measured by helium expansion tests. However, helium atoms can closely approach a pore wall and get into small pores due to their small size. Therefore, a helium-based volume is always larger than the accessible volume for a specific adsorbate. In this chapter, we use GCMC simulation to investigate methane adsorption on shale with pore sizes of 10, 20 and 30 Å at a temperature of 323 K. Five void volumes, including an apparent volume determined by helium expansion tests, a helium-probed volume, a simulated methane-based volume, an analytical methane-based volume, and a physical volume, are recognized. Use of a physical volume and a helium-based volume leads to negative excess adsorption at high pressure, which is not consistent with local density profiles at such pressure. It is thus necessary to calibrate a physical volume or use a methane-based volume as a theoretical value for calculating excess isotherms. Excess isotherms determined by a calibrated volume or methane-based volume are more accurate and keep positive even at high pressure. Appropriate calculations of excess isotherms also influence an estimation of proportions of excess adsorbed and free gas amounts in shale gas reservoirs, further having a great impact on the determination of a development strategy.

The remainder of this chapter is organized as follows: In Section 6.2, five volumes determined under various conditions are defined. In Section 6.3, we illustrate a pore model, force field and

methodology in our GCMC simulation. Finally, local density profiles at different pressures in carbon-slit pores are displayed and effects of pore size on density profiles are also investigated in Section 6.4. The excess adsorption amounts calculated by the five volumes defined in Section 6.4 are compared to obtain excess adsorption isotherms with a physical meaning. Methods for calibration of methane adsorption isotherms and its effect on estimations of proportions of free and adsorbed gas in shale reservoirs are also discussed in Section 6.5. In Section 6.6, we finally summarize some important findings and conclusions.

6.2 Definition of volumes

6.2.1 Simulated methane-based volume

Traditionally helium expansion tests are used for determining a void volume. However, due to the smaller collision size of helium atoms compared to methane molecules, the void volume determined by helium tests is always overestimated. In this chapter, we conduct GCMC simulations for methane adsorption in nanopores and regard methane as non-adsorbed gas to obtain the methane-based void volume, which can be applied to calculating accurate adsorption isotherms. Thus, the excess adsorption is assumed zero at any temperature or pressure values when determining the methane-based void volume. Then a methane-based pore volume can be determined using the method for determination of a helium-based volume in simulations as described in Section 5.2. According to Section 5.2, a methane-based volume can be obtained when these three density values are almost the same ($\rho_a \approx \rho_t \approx \rho_b$, $\rho_a > \rho_t > \rho_b$).

6.2.2 Analytical methane-based volume

Some scholars thought that an accessible volume to adsorbates is the part where the solid-fluid potential is negative [112,113]. However, this was proved too restrictive because molecules can

also penetrate into a region where the solid-fluid potential is positive due to high temperature. Moreover, this defined accessible volume is found to give no physical meaning for the Henry constant and the differential heat at extremely high temperature [114]. Therefore, a new accessible volume was suggested by Prasetyo et al. to satisfy the correct physical constraints (zero differential heat at zero loadings, zero Henry constant at infinite temperature) [114].

The isosteric heat is an important parameter that describes the energy of adsorption and the isosteric heat at zero loadings can be obtained from the Clausius-Clapeyron equation [114,203]:

$$q_{st} = k_B T^2 \left(\frac{\partial lnp}{\partial T}\right)_{n_e} \tag{6.1}$$

where q_{st} is the isosteric heat, k is the Boltzmann constant, T is temperature, and P is pressure.

The differential heat, which is defined as the difference between isosteric heat and kT can be obtained by [114]

$$q_{st}{}^{(0)} - kT = \frac{\int_{V_\Omega}[-U(r)]\exp\left[-\frac{U(r)}{kT}\right]dr}{\{\int_{V_\Omega}\exp\left[-\frac{U(r)}{kT}\right]dr - V_\Omega\}} \tag{6.2}$$

where V_Ω is the volume that is accessible to adsorbates at any temperature, φ is the solid-fluid potential energy, and r denotes the position of an adsorbate particle.

When the temperature approaches infinite, the differential heat should be zero, which is given by

$$\lim_{T\to\infty}(q_{st}{}^{(0)} - kT) = \lim_{T\to\infty}\frac{\int_{V_\Omega}[-U(r)]\exp\left[-\frac{U(r)}{kT}\right]dr}{\{\int_{V_\Omega}\exp\left[-\frac{U(r)}{kT}\right]dr - V_\Omega\}} \tag{6.3}$$

To satisfy the correct constraints:

$$\int_{V_\Omega}[-U(r)]\,dr = 0 \qquad (6.4)$$

The new accessible volume corresponds to the part where the integral above equals zero [114], and **Figure 6.1** illustrates the schematic of the analytical methane-based volume for a slit pore. As indicated in Eq. (10), the areas of the positive regions (S1 and S2) are equal to the area of the negative region (S3). Potential equations such as the 10-4-3 equation and 9-3 equation can be applied to describe the solid-fluid potential between an adsorbate molecule and a flat structureless solid wall [204,205].

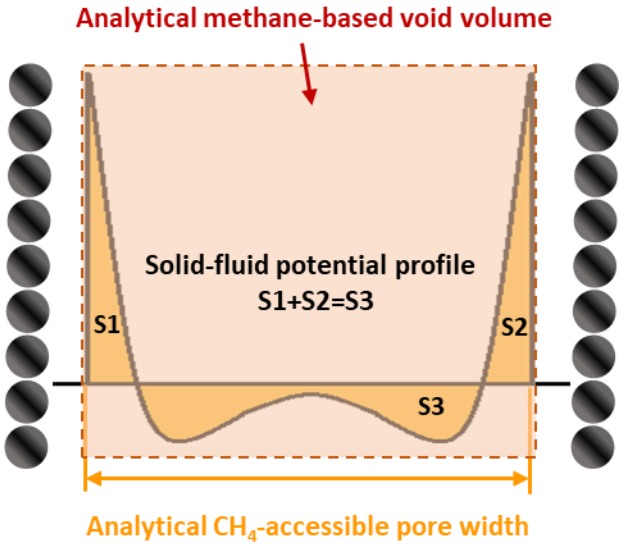

Figure 6. 1 Schematic of the analytical methane-based void volume and the areas of the positive regions (S1 and S2) are equal to the area of the negative region (S3).

6.2.3 Other referred volumes

In this work, we also use other values of the pore volume to investigate the reasonability of the choice of the void volume for calculating excess isotherms. Descriptions of different investigated void volumes are shown in **Table 6.1**. An apparent volume value v_{app} is determined by traditional

helium expansion tests [195,196]. In our study, we also use GCMC simulation to model the helium tests and employ the equation (5.1) to calculate the apparent helium-based volume. Helium probed void volume v_{He} is determined by Poreblazer developed by Sarkisov and Harrison (2011). A physical void volume of pores v_{phy} is obtained by simply multiplying the pore width H and surface area A.

Table 6. 1 Descriptions of the void volume determination of carbon slits.

Volume	Description
v_{app}	determined by traditional helium tests
v_{CH4_sim}	determined under the condition when $\rho_a \approx \rho_t \approx \rho_b$
v_{CH4_ana}	determined by the analytical method
v_{He}	determined by a helium probe
v_{phy}	$H \cdot A$

6.3 Methodology and model

6.3.1 Pore configuration

Due to the development of scanning electron microscope (SEM), characterization studies with high resolutions can be conducted on the organic-rich shale. It is shown that pores with different geometries constitute the pore networks in shale with the size varying from nanometer to micrometer [94,95,207]. According to the research done by Bu et al. [208], most pore geometries in shale are cylindrical and slit-like. We use slit-like pores because they are plentiful in the shale reservoirs and they have similar fluid density distributions with equal-size cylindrical pores [209]. An organic-hosted nanopore of shale is composed of two parallel graphite walls (**Figure 6.2**), and methane molecules acting as the shale gas will fill this pore. Three-dimensional periodical boundary conditions are applied in the three directions of simulation cell. The surface dimensions of each graphene layer in the x and y directions are 51.6 Å and 52.3 Å, respectively. We use the

nanopores with pore sizes of 10, 20 and 30 Å, and the pore size is defined as the distance between the centers of carbon atoms of the two pore walls in the *z*-direction.

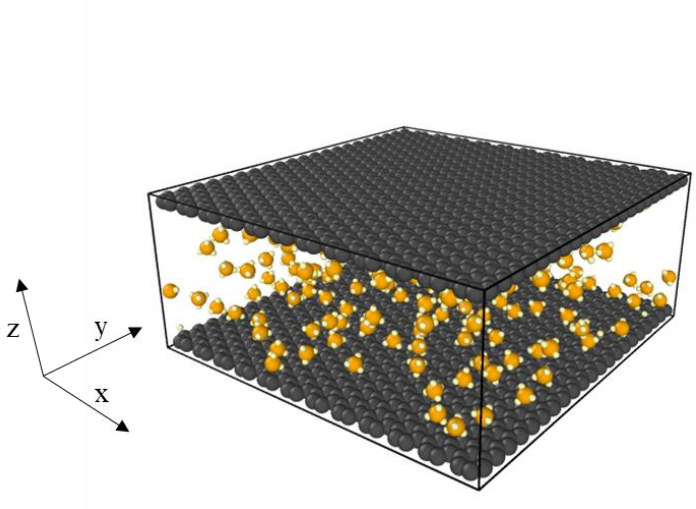

Figure 6. 2 Schematic of an organic-hosted nanopore of shale.

6.3.2 Simulation details

Interactions between adsorbate and adsorbate, adsorbate-adsorbent play an important role in an adsorption system. We use consistent valence force-field (CVFF) to describe methane adsorption on carbon-slit pores based on the ab initio calculations and experiments [160]. To save computing time, methane molecules and carbon-slit pores are treated as rigid structures.

Table 6. 2 Interaction parameters used in the simulation.

Bond parameters		
Bond type	k_{bond} (kcal mol^{-1} Å^{-2})	r_0 (Å)
C-C (graphene)	480.00	1.34
C-H (methane)	340.61	1.11

Angle parameters			
Angle type	k_{angle} (kcal mol^{-1} rad^{-2})	θ_0 (rad)	
C-C-C (graphene)	90.0	2.094	
H-C-H (methane)	39.5	1.911	
Torsion parameters			
Torsion type	$k_{torsion}$ (kcal mol^{-1})	n	d (rad)
C-C-C-C (graphene)	3.1	2	3.141
Nonbond parameters			
Nonbond type	ε (kcal mol^{-1})	σ (Å)	q (e)
C-C (graphene)	0.148	3.617	0.0
C-C (methane)	0.161	3.475	-0.4
H-H (methane)	0.038	2.461	0.1

Intermolecular interactions are calculated by a pairwise additive Lennard-Jones (LJ) 12-6 function, and the Lorentz-Berthelot mixing rule is used to calculate cross interaction parameters for unlike pairs. The interaction between the charged sites is calculated by equation (4.22). The parameters for describing these interactions are listed in **Table 6.2**. We perform GCMC simulations for methane at the temperatures of 323 K for 10, 20, and 30 Å pores with the pressure ranging from 0.01 to 1000 MPa, respectively. A total of 5e+6 GCMC moves are conducted in each GCMC simulation. The Verlet algorithm is employed to solve Newton's equations of motion and a Nose-

Hoover thermostat is used to control the reservoir temperature. Each simulation is conducted for 10 ns with a timestep of 1 fs. The first 5 ns are used to equilibrate the system and another 5 ns are for calculating the adsorption amount.

6.4 Results and discussions

We first illustrate the density distributions of methane molecules in carbon slit pores at 323 K with different pressures, and effects of the pore size and pressure on a local density profile are also clarified. Then five void volumes defined in Section 6.2 are compared. Finally, we demonstrate the effects of helium-based void volume on methane adsorption isotherms.

6.4.1 Density distribution in carbon slit pores

Figure 6.3 shows the methane molecule distribution in 20 Å carbon slit pores with different gas pressure. At low pressure, the distribution of molecules is random and it is obvious that the molecules are preferring staying close to the pore walls. As pressure increases, the layers closest to the pore walls are first formed by methane molecules and some degree of clustering can be found in the pore. When gas pressure reaches up to 1000 MPa, there are five layers accommodated in the pore and the packing of molecules is very efficient.

The plots of local density profiles of 10, 20 and 30 Å slit pores at 1, 10, 100 and 1000 MPa are shown in **figures 6.4-6.6**. The dashed lines in the plots represent the corresponding density of the bulk phase. First, we summarize the characteristics of adsorption in the pore of 10 Å. Only two molecular layers are formed in this ultrafine pore and the bulk phase is difficult to distinguish. Due to the confined pore size, the attraction between the pore walls and the methane molecules in the pore is always high, so the bulk phase is absent in an ultrafine pore. As pressure increases, the

peaks of the density profile increase and the peaks move close to the pore wall. Compared with the pore of 10 Å, there are some similar observations for the pores of 20 Å and 30 Å. The major difference is that more layers can be accommodated in the pore. Higher peaks of density profile near the pore wall are caused by the stronger interaction between the pore wall and methane molecules close to the pore wall. The bulk phase can be formed in the pore center at low pressures in 20 and 30 Å as a consequence that the interaction between pore wall and methane molecules is not strong in the pore center with a larger pore size. Under low pressures of 1 and 10 MPa, only two distinct peaks can be seen near the pore wall and the density in the center of the pore fluctuates around the value of the bulk density. The local density in the pore is not always larger than the bulk density. There are also some valley parts between the peaks and these valley parts are enhanced by higher pressure. At 1000 MPa for pores with 10, 20 and 30 Å, the peak parts above the bulk density compensate for the valley parts. If we assume the area between the closest peak and valley to the pore wall as the adsorbed layer, the averaged density of the adsorbed phase can be comparable to the bulk density at 1000 MPa. Based on equation (5.3), the discrepancy between the calculated total density values of 10, 20 and 30 Å at 1000 MPa and the corresponding bulk phase density can be neglected. Therefore, we can use the equation (5.1) to determine the void volume at 1000 MPa and this value is the simulated methane-based void volume.

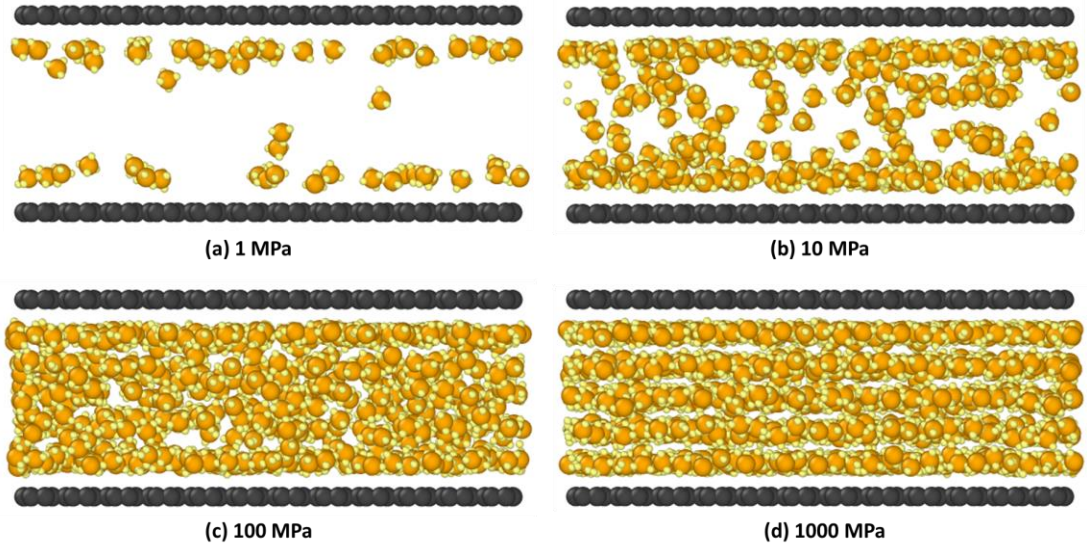

Figure 6. 3 Methane molecule distribution in carbon slit pores at 323 K. (a) 1 MPa, (b)10 MPa, (c) 100 MPa, (d) 1000MPa.

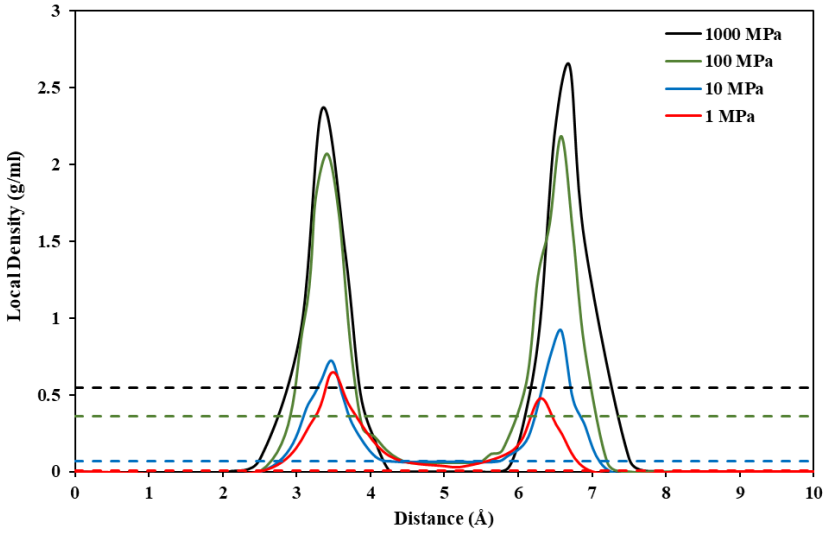

Figure 6. 4 Local density versus distance for the 10 Å carbon slit pore.

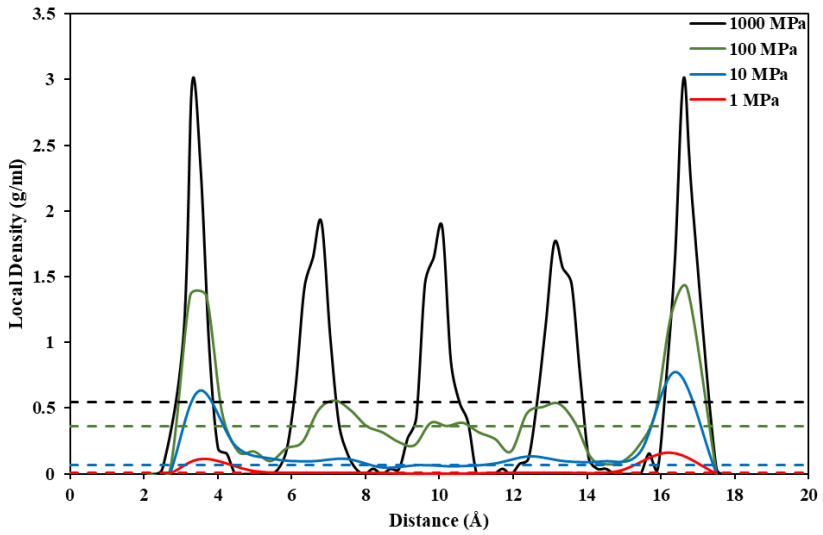

Figure 6. 5 Local density versus distance for the 20 Å carbon slit pore.

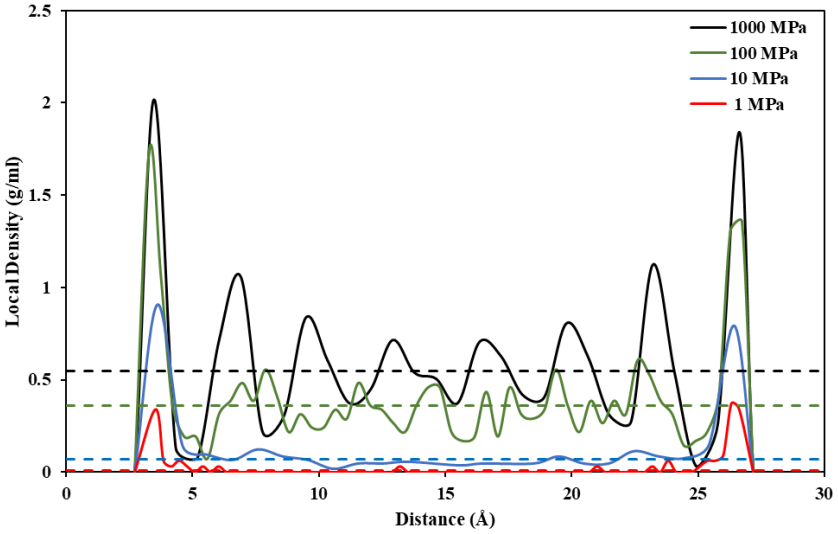

Figure 6. 6 Local density versus distance for the 30 Å carbon slit pore.

6.4.2 Void pore volumes

Five pore volume values of pores are compared in **Table 6.3**, including an apparent void volume by traditional helium tests (v_{app}), a helium-probed volume (v_{He}), a simulated methane-based

volume (v_{CH4_sim}), an analytical methane-based volume (v_{CH4_ana}), and a physical void volume (v_{phy}). The methods for determining these volumes have been discussed in Section 6.2.

Table 6. 3 The void volumes of the carbon slit pore with the pore size of 10, 20 and 30 Å determined by different methods

Volume (Å^3)/Pore width (Å)	10	20	30
v_{app}	21112.15	49094.32	76696.11
v_{He}	18993.64	46104.65	73151.36
v_{CH4_sim}	16214.51	43748.94	71445.96
v_{CH4_ana}	15793.06	43019.29	70148.03
v_{phy}	26986.80	53973.60	80960.40

Table 6. 4 Effective pore widths of the carbon slit pore determined by different methods.

Pore width (Å)	10	20	30
H_{app}	7.82	18.19	28.42
H_{He}	7.04	17.08	27.11
H_{CH4_sim}	6.01	16.21	26.47
H_{CH4_ana}	5.85	15.94	25.99
H_{phy}	10	20	30

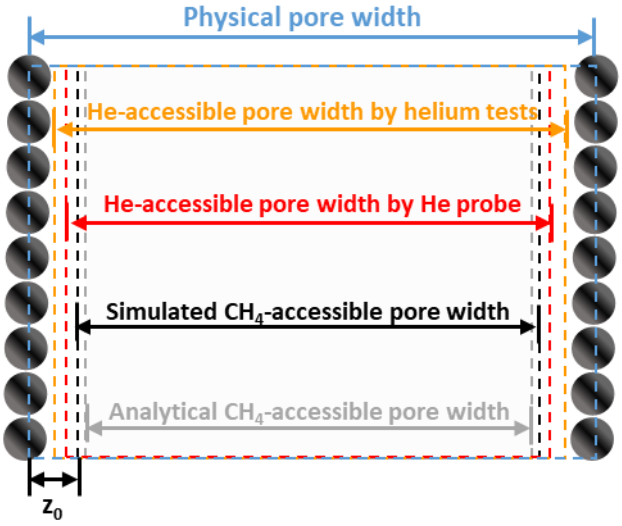

Figure 6. 7 Schematic of various pore widths for a carbon slit pore.

It is shown that the physical volume is always larger than both methane-based and helium-based volumes. The pore width used for calculating the physical volume is defined as the distance between the centers of carbon atoms of two pore walls in the *z*-direction, and this width is always larger than the accessible width for helium and methane (**Figure 6.7**). Additionally, helium adsorption results in larger volumes determined by helium tests compared to the helium-probed volume obtained by the Poreblazer and effects of helium adsorption on the determination of the void volume in the experiments cannot be ignored. It is obvious that methane-based volumes are generally smaller than helium-based volumes. As shown in **Figure 6.8**, the center of helium atom can be closer to the pore wall compared to methane molecule and thus helium atom can approach closer to the pore wall. Moreover, helium can get into small pores which are inaccessible to methane. These two reasons can contribute to a larger helium-based volume. We simply use one single slit pore in our study and the second reason will not have an effect on the volume

determination. However, the shale reservoir has more complex pore structures with various pore sizes, and penetration of helium into small pores can have a significant effect on the void volume measurement of shales.

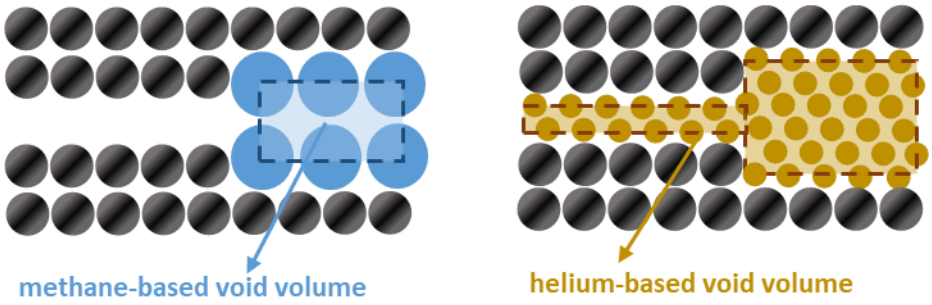

Figure 6. 8 Helium-based and methane-based void volume of the slit pore are compared.

Based on our results, the simulated methane-based volume is larger than the analytical methane-based volume. The analytical volume is calculated based on the assumption of extremely high temperatures while the simulated one is obtained at high pressures. When the pressure in the pore is high, methane molecules near the pore wall can approach closer to the pore wall under the repulsive forces from other methane molecules in the pore, which further results in a larger methane-based volume. Therefore, the simulated methane-based volume can represent the accessible volume to methane molecules more accurately.

Effective pore widths are calculated by dividing the determined void volume by the surface area (**Table 6.4**). As described before, the physical pore width is always larger than other effective ones. Therefore, we use the simulated methane-based volume to calibrate the physical pore when it is used for calculation the pore void volume. The distance between the closest approach of the adsorbate molecules and the pore wall z_0 depends on the L-J size parameters of both adsorbates and adsorbents. A coefficient m is introduced for calculating the distance z_0:

$$z_0 = m\sigma_{fs} \tag{6.5}$$

Then the effective pore width can be written as

$$H_e = H_{phy} - 2z_0 \tag{6.6a}$$

$$H_e = H_{phy} - 2m\sigma_{fs} \tag{6.6b}$$

where σ_{fs} is the cross interaction L-J size parameters of adsorbates and adsorbent, which is calculated by the Lorentz-Berthelot combining rule. Here, the calculated coefficient for methane and carbon slit pores doesn't vary too much for different pore sizes and it can be assumed as a constant value 0.55 for calibration. Although the difference in these pore width is not essential when the bulk density is sufficiently low, it can cause an appreciable discrepancy when calculating the excess adsorption amount at high pressures [112].

6.4.3 Methane adsorption analysis

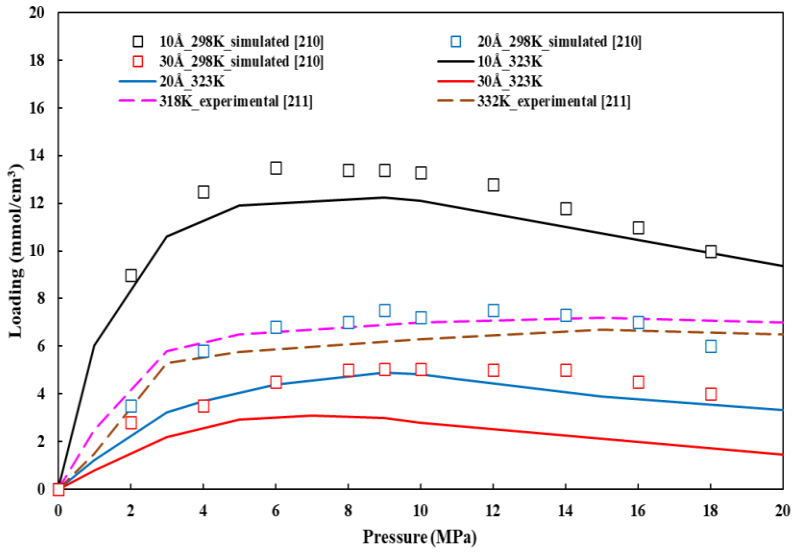

Figure 6. 9 Comparison of simulation data with other simulations and experiments from literature [210,211]**.**

In order to validate the accuracy of the simulation data, the excess adsorption isotherms calculated based on the apparent void volume by the equation (2.2) for the carbon slit pores of 10, 20 and 30 Å are compared with available data from other simulation and experiments [210,211]. Generally, these eight excess isotherms show the same trend and the data obtained from both simulations and experiments are in the same order of magnitude as displayed in **Figure 6.9**. However, some discrepancies can still be seen in the plot. The simulated data reported by Mosher et al. [210] are always larger than our simulation data. Adsorption is an exothermic process, so low temperature can enhance the methane adsorption and the excess adsorption amounts at 298 K are larger than the amounts at 323 K. The deviation between the simulation and experiments is due to the fact that a real organic pore structure is combined of various pore widths and more complex than the slit-pore model.

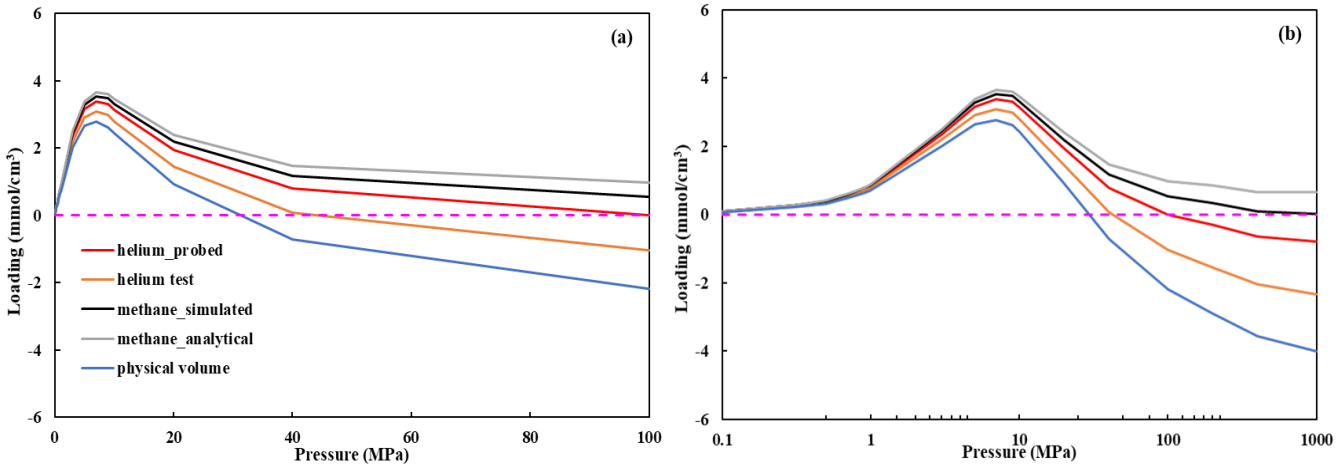

Figure 6. 10 Excess adsorption isotherms of methane for 10 Å pore at 323 K with (a) low range pressure; (b) wide range pressure.

Five different void volumes are used to calculate the excess adsorption amounts for methane by the equation (2.2) and the results are displayed in **figures 6.10-6.12**. With sufficient pressure

increase, the excess adsorption amount first reaches a maximum. According to the equation (2.2), the maximum excess adsorption amounts can be reached when the increase in the total loading amount is equal to the increase in the bulk density with pressure. Beyond this point, this increase is followed by a subsequent decrease with pressure. As pressure continues to go up, most of the available sites are filled up and additional pressure is required for adsorbing more molecules. With fewer molecules added into the adsorbed phase, the excess adsorption starts to decrease.

In the GCMC simulations, the total loading amount is dependent on pressure and temperature. Based on the equation (2.2), the void volume used for calculation of excess amounts is of great importance when the bulk density is given and the total loading number is constant at a specific pressure and temperature. As shown in **figures 6.10-6.12**, a larger void volume can result in underestimation of the excess adsorption amount and even negative excess adsorption at a certain pressure. Taking the excess isotherms for 20 Å pores as an example, the isotherms calculated by the physical volume, the helium-probed volume and the apparent volume determined by helium expansion tests become negative within the narrow pressure range. However, the adsorbed phase can be clearly seen in the density profile and the excess adsorption amount under this condition is definitely positive. These calculated excess isotherms by the physical volume, helium-probed volume, and the apparent volume are contradictory to the density profile results. Therefore, it is obvious that use of helium-based volume can lead to a wrong excess isotherm even for a simple carbon slit pore. For shale reservoirs and other natural minerals, the pore size distribution is much more complex than the simulation cell. For the pores which are bigger than helium but smaller than methane molecules, they cannot be accessed by methane. However, the void volumes of these pores are still included in the total void volume, which is much larger than the actual accessible

void volume. Therefore, the calculated isotherms by helium-based volume are far from true. In general, the isotherms determined by simulated and analytical methane-based volumes have the same trend and remain positive even at extremely high pressure. The isotherms calculated by the analytical volume are slightly larger than the simulated ones. This is because the analytical volume is not determined under the assumption of extremely high pressure. Under an extremely high-pressure condition, the gas molecules pack close to each other, the adsorbed molecules can be affected by strong repulsion from neighboring molecules and they can approach closer to the pore wall. Thus, use of the analytical methane-based void volume can result in an overestimation of excess adsorption amounts.

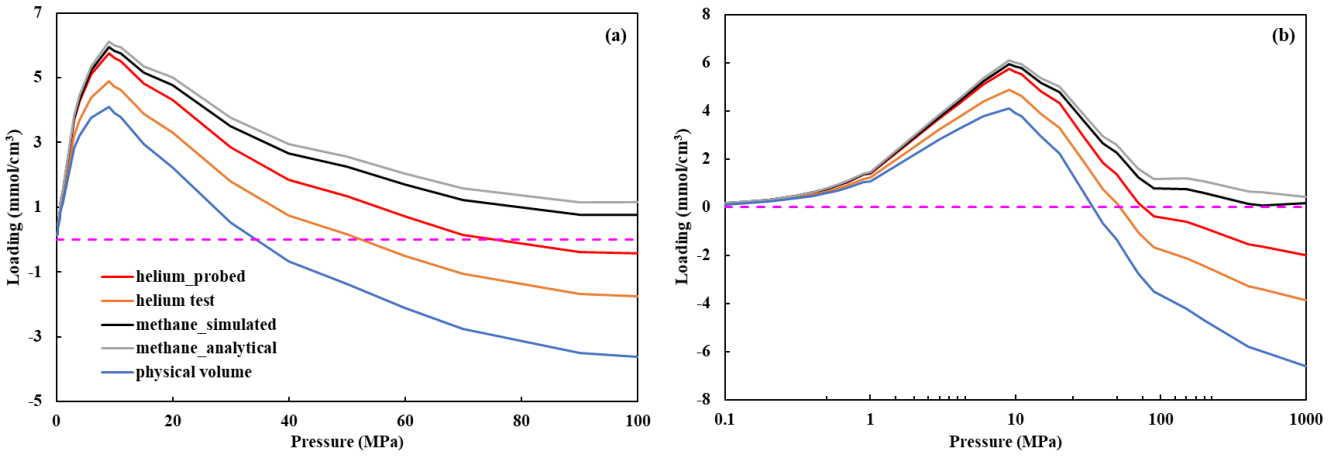

Figure 6. 11 Excess adsorption isotherms of methane for 20 Å pore at 323 K with (a) low range pressure; (b) wide range pressure.

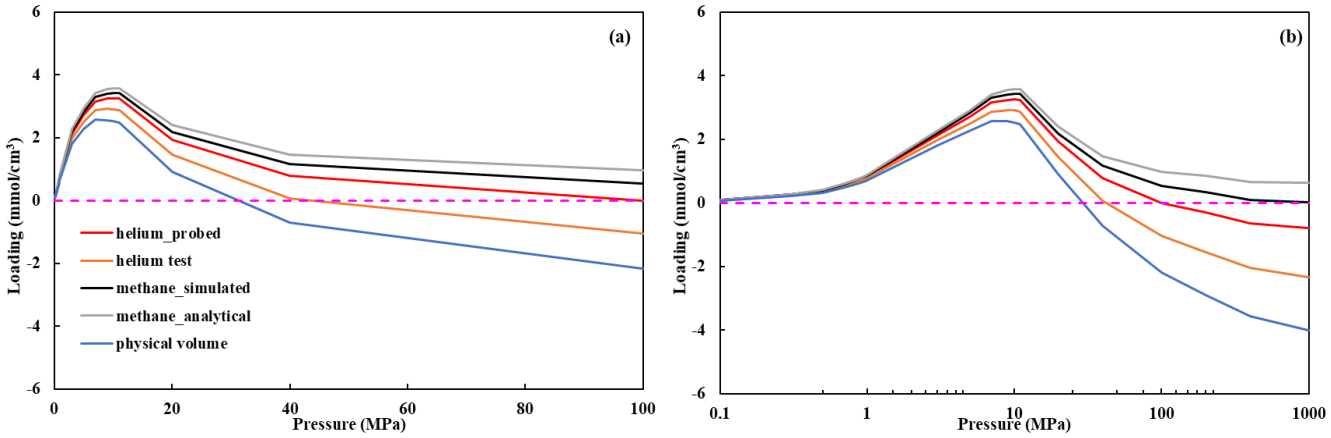

Figure 6. 12 Excess adsorption isotherms of methane for 30 Å pore at 323 K with (a) low range pressure; (b) wide range pressure.

Figure 6.13 shows the excess adsorption isotherms as a function of pressure and pore width. By comparing the excess isotherms for pores with different sizes, it is obvious that smaller pores have a higher excess adsorption amount than larger pores. With the increase in pore size, the maximum value of excess adsorption isotherms occurs at higher pressure. The adsorption potential exerted by pore walls on the methane molecules is lower in a larger pore and higher pressure is necessary

to pack more molecules in larger pores. These results are also illustrated in other previous investigations [210].

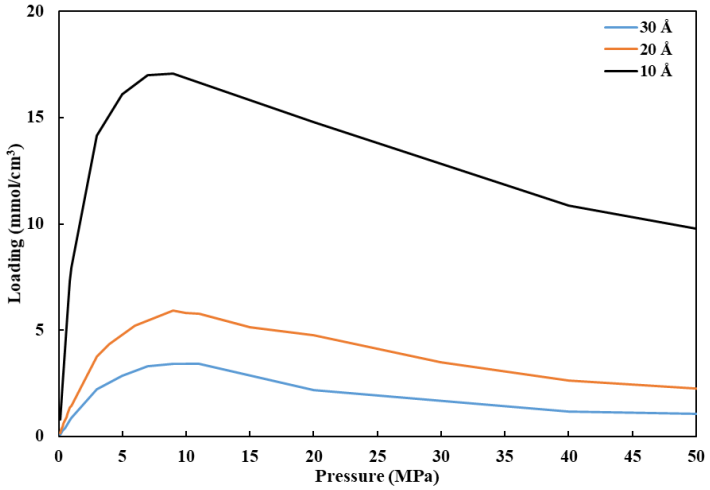

Figure 6. 13 Comparison of excess methane adsorption isotherms for pores of 10, 20 and 30 Å.

6.5 Applications

6.5.1 Calibration of methane adsorption isotherms in shale

The pore volume of the shale sample measured by helium expansion tests is always overestimated in many isothermal adsorption experiments and the corresponding excess adsorption amounts will be underestimated. Based on our results, the measured apparent pore volume can be calibrated and contribute to an accurate calculation of adsorption isotherms. The shale sample CQ collected from Sichuan Basin, Southwest China is taken as an example and the apparent pore volume of this sample is 0.3688 cm^3. The measured pore size distribution for the shale sample CQ is presented in **Figure 6.14** [77], and it is obvious that the dominant pore size ranges from 2 to 4 nm.

The total pore volume can be expressed as

$$v_t = \sum_{i=1}^{N} v_i \tag{6.7}$$

where v_i represents the apparent volume of pores in the *i*th group, and these groups are classified by the pore size in the shale sample; *N* is the number of the groups in the shale sample.

Assuming that these pores are slit-shaped, the calibrated methane-based volume can be given by

$$v_t^* = \sum_{i=1}^{N} \alpha_i v_i = \sum_{i=1}^{N} \alpha_i f_i v_t \tag{6.8}$$

where α_i is the calibrated factor of the apparent volume for the *i*th group ($\alpha_i = v_{iCH4\_sim}/v_{iapp}$), which is determined by GCMC simulation; f_i is the volume fraction of the *i*th group.

Combining equations (2.2) and (6.8), the calibrated excess adsorption amount can be obtained:

$$n_e^* = n_t - \frac{\sum_{i=1}^{N} \alpha_i f_i v_t \cdot \rho_b}{M} = n_e + \frac{(1-\sum_{i=1}^{N} \alpha_i f_i) v_t \cdot \rho_b}{M} \tag{6.9}$$

Figure 6.15 shows methane excess adsorption isotherms of the shale sample CQ. Three solid lines are generated by the L-G model based on data collected from methane adsorption experiments within a low-pressure range (0-20 MPa) [77]. When extending the isotherms to a high-pressure value of 140 MPa, a negative excess adsorption amount can be found, which has no physical meaning. After the calibration of the pore volume of the shale sample, the excess adsorption isotherms can remain positive at a high pressure.

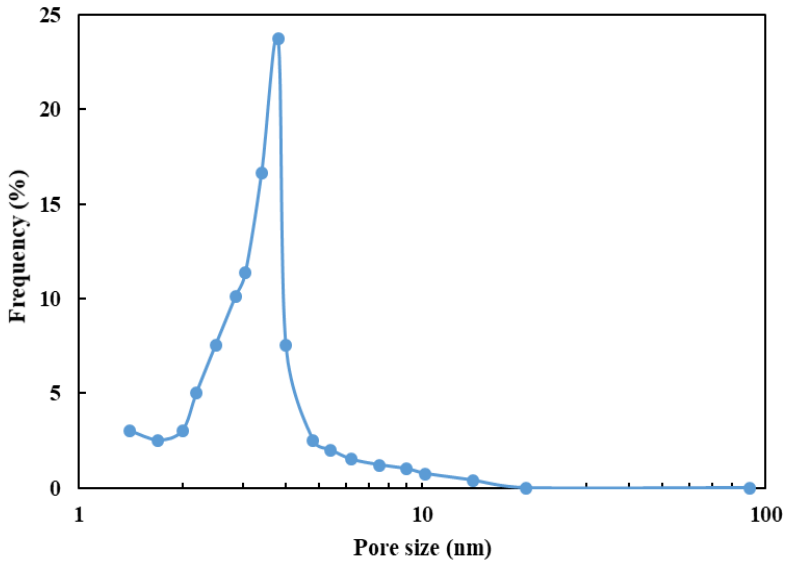

Figure 6. 14 Pore size distribution of the shale sample CQ [77].

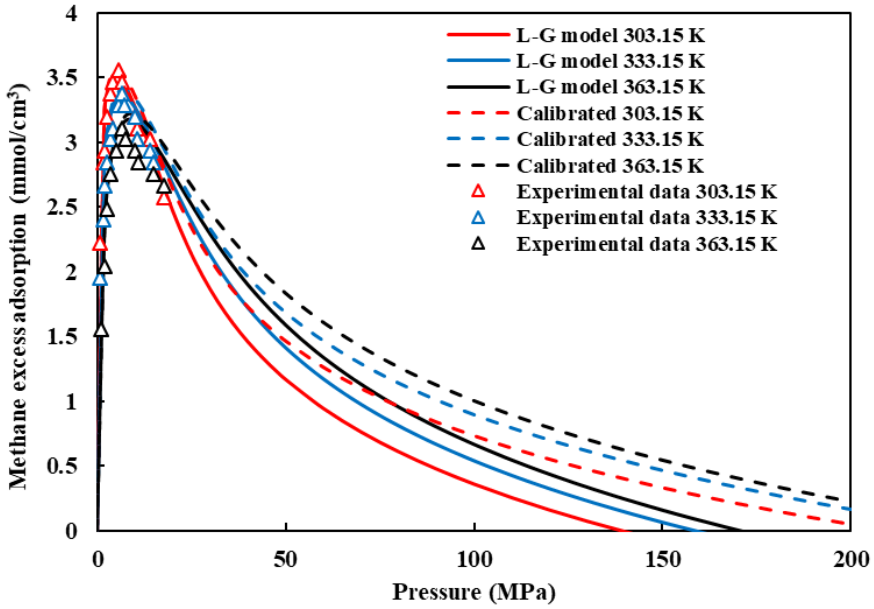

Figure 6. 15 Excess methane adsorption isotherms for the shale sample CQ.

6.5.2 Proportions of the free gas and the excess adsorbed gas

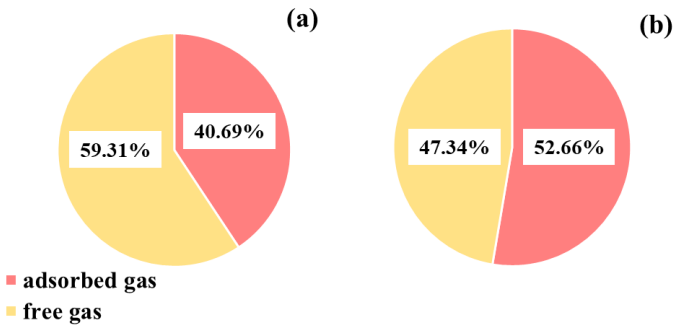

Figure 6. 16 Proportions of the free gas and the excess adsorbed gas calculated based on (a) isotherms determined by the apparent volume and (b) isotherms determined by the simulated methane-based volume.

Furthermore, we calculate the proportions of the free gas amounts and the excess adsorbed gas amounts based on the reservoir conditions of the shale sample CQ. In the reservoir, the reservoir pressure and temperature correspond to 47 MPa and 384 K, respectively [77]. The proportions of the excess adsorbed gas vary a lot calculated on the basis of the isotherms determined by the apparent volume and the methane-based volume **(Figure 6.16)**; the contributions of the excess adsorbed gas are 40.69% and 52.66%, sequentially. Apparently, appropriate use of a void volume can also have a significant effect on the estimation of the free gas amount and adsorbed amount in shale gas reservoirs, which can influence the prediction of production and development strategies of shale gas reservoirs.

6.6 Summary

In this chapter, we introduce five void volumes of carbon slit pores including an apparent volume determined by helium expansion tests, a helium-probed volume, a simulated methane-based volume, an analytical methane-based volume, and a physical volume. Besides, the choice of the

void volume for calculating excess adsorption amounts is verified by using the GCMC simulation. Based on our study, some conclusions can be made as follows:

1. Due to the finite size of adsorbate molecules, a physical void volume is always larger than both helium-based and methane-based pore volume. It is necessary to calibrate the physical volume before using it to calculate the excess adsorption amounts.
2. When a helium-based volume is used in the calculation of the excess amount, the excess isotherms become negative at high pressures, which is contradictory to the density profile results at that pressure and has no physical meaning.
3. The simulated methane-based volume can represent the accessible volume probed by the methane molecule, and it is accurate to apply it to excess amounts calculation and the adsorption mechanism investigation. Use of the analytical methane-based volume leads to overestimations of excess adsorption amounts. With the appropriate volume, the excess isotherms are always positive at high pressures.
4. Small pores have a higher excess adsorption amount than large pores. The maximum value of excess adsorption isotherms occurs at higher pressure in larger pores due to the lower adsorption potential exerted by the pore walls.
5. Utilization of the void volume can have a significant effect on the estimation of the contribution of free gas amount and adsorbed amount in shale gas reservoirs, which can influence the prediction of shale gas production.

Chapter 7 Gas adsorption in shale kerogens coupling sorption-induced swelling

7.1 Introduction

Gas adsorption can induce kerogen swelling with changes in pore volumes. In this chapter, hybrid GCMC/MD simulations are conducted to investigate gas adsorption in kerogen and the corresponding sorption-induced swelling. A unified relationship between volumetric strain and an absolute adsorption amount is developed for different adsorbates. A theoretical model for calculating excess adsorption isotherms coupling swelling is proposed. Results show that (i) steep increases in C_2H_6 and CO_2 adsorption isotherms at lower pressure indicate stronger affinities of C_2H_6 and CO_2 than CH_4; however, a larger size of C_2H_6 results in smaller accessible pore volumes and smaller maximum absolute adsorption amounts than CH_4 and CO_2. (ii) A linear relationship between volumetric strain and an adsorption amount is shown for CH_4, C_2H_6 and CO_2, separately. The volumetric strain caused by per unit of the absolute adsorption amount for C_2H_6 is the greatest because C_2H_6 with greater diameters has larger contact areas with pore walls for the same adsorbed amount. The maximum swelling upon CO_2 adsorption is the largest ($CO_2 > CH_4 > C_2H_6$) due to its greatest absolute adsorption amount. (iii) Excess adsorption isotherms generated by our model are consistent with excess adsorption data calculated by variable pore volumes, which shows a large discrepancy compared to that determined using constant volumes, especially at high pressures. The difference between the fraction of free CH_4 in our model and that calculated by using a constant volume is up to 23.2% at 323 K, 40 MPa. Therefore, this theoretical model can accurately

determine free and adsorbed gas amounts in shale, further influencing prediction of hydrocarbon production and CO_2 sequestration.

The remainder of this chapter is organized as follows: in Section 7.2, the establishment of a kerogen model is illustrated. Moreover, force fields and GCMC/MD simulation details are introduced. Details of volumes used in this study and the theoretical model are explained in Section 7.3. In Section 7.4, we display the effects of kerogen swelling on volumetric strain and porosity induced by adsorption of different adsorbates, including CO_2, CH_4, and C_2H_6. Additionally, effects of kerogen swelling on excess adsorption isotherms are discussed. Moreover, limitations of this study are illustrated in Section 7.5. In Section 7.6, we finally summarize some important findings.

7.2 Methodology

7.2.1 Kerogen model

A type II-D kerogen model unit developed by Ungerer et al. [212] is used in our work with a chemical formula of $C_{175}H_{102}O_9N_4S_2$ as shown in **Figure 7.1(a)**. It is a kind of typical organic matter in a gas formation zone deposited in a marine anoxic environment, which is common in unconventional gas reserves such as the Barnett Shale [212]. Analysis of functional groups and elements for this kerogen unit including the H/C, O/C, N/C and S/C ratios, the average aromaticity, the average size of aromatic units, the percentage of aromatic carbons, and the number of protonated aromatic carbons is consistent with experimental results [213].

A consistent valence force field (CVFF) is used to simulate the kerogen model in LAMMPS [160] and eight kerogen model units are initially placed in a simulation box of 100.0 Å × 100.0 Å × 100.0 Å to build a kerogen porous model. The steps for the construction of a kerogen porous model

are shown in **Table 7.1**. First, an NVT ensemble is used and the temperature is kept at 1000 K by a Nosé-Hoover thermostat for 100000 fs with a time step of 1 fs. Then these kerogen units are relaxed in an NPT ensemble (10 MPa) and the temperature decreases from 1000 K to 300 K within four steps (1000 K-900 K, 900 K-700 K, 700 K-500 K, 500 K-300 K). Each cooling step is run for 100000 fs. Subsequently, the system is equilibrated in an NPT ensemble with the pressure decreasing from 10 MPa to 0.1 MPa for 400000 fs. A kerogen porous model (28.9 Å × 28.9 Å × 28.9 Å) displayed in **Figure 7.1(b)** can be obtained after these steps and its density is around 1.3 g/ml at 300 K and 0. 1 MPa that is consistent with data in the literature [212,214].

Table 7. 1 Steps for the construction of a kerogen porous model.

Step	Ensemble	Pressure (MPa)	Temperature (K)	Simulation time (fs)
1	NVT	10	1000	100000
2	NPT	10	1000 - 900	100000
3	NPT	10	900 - 700	100000
4	NPT	10	700 - 500	100000
5	NPT	10	500 -300	100000
6	NPT	10 – 0.1	300	400000

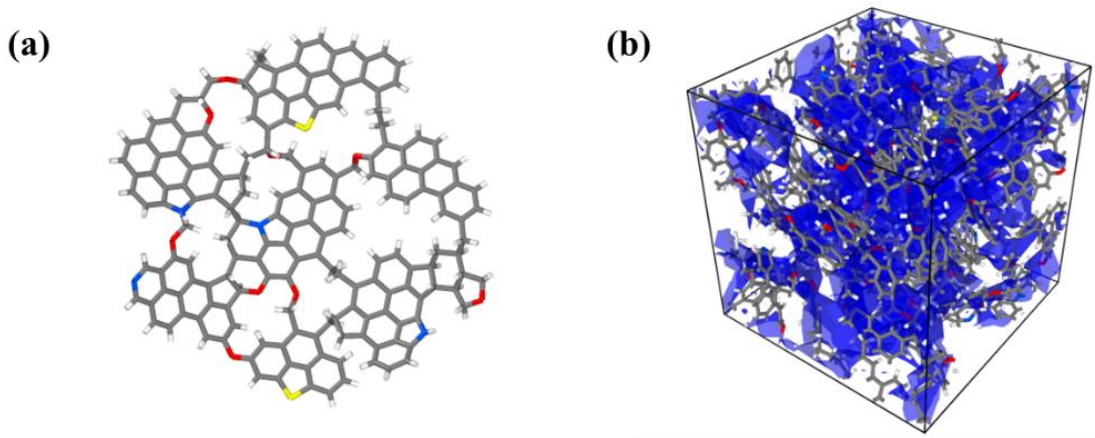

Figure 7. 1 (a) Model unit of kerogen type II-D ($C_{175}H_{102}O_9N_4S_2$) developed by Ungerer et al. [212]. Color scheme: carbon (grey), hydrogen (white), oxygen (red), nitrogen (blue), sulfur (yellow); (b) kerogen porous model with an accessible surface area by CO_2 molecules.

7.2.2 Molecular simulation details

Intermolecular interactions are calculated by a pairwise additive Lennard-Jones (LJ) 12-6 function, and the Lorentz-Berthelot mixing rule is used to calculate cross interaction parameters for unlike pairs. The interaction between the charged sites is calculated by equation (4.22). The TraPPE United Atom (TraPPE-UA) force field is also applied to simulate CH_4 and C_2H_6 molecules and the TraPPE force field is used for description of CO_2 molecules. These force fields have been proven to reproduce the thermodynamic and equilibrated vapor-liquid properties [215–218]. Parameters for molecules including CH_4, C_2H_6, and CO_2 are displayed in **Table 7.2** [162].

Table 7. 2 L-J parameters employed in the simulations [200,216–218]**.**

Site	ε/k_B (K)	σ (Å)	q (e)
CH_4 (methane)	148.0	3.73	0.00
CH_3 (ethane)	98.0	3.75	0.00

C (carbon dioxide)	27.0	2.80	0.70
O (carbon dioxide)	79.0	3.05	-0.35

A hybrid GCMC/MD method is implemented to investigate gas adsorption and the corresponding swelling process of the kerogen porous structure [16,17]. Periodical boundary conditions are applied in three directions and the Verlet algorithm is used to solve Newton's equations of motion in LAMMPS. First, MD simulations in an NPT ensemble are carried out for 1000 steps, and then a GCMC cycle including 1000 GCMC exchanges and 1000 GCMC moves is performed. The probabilities for insertion and deletion attempts in GCMC exchanges, and translation and rotation attempts in GCMC moves are 50%. In our GCMC simulations, the chemical potential is substituted by pressure, and the fugacity coefficient of an ideal gas reservoir and the fugacity of gas molecules can be calculated by the equation of state such as the Peng-Robinson equation. The number of molecules is updated after each GCMC cycle for the subsequent MD simulation steps. In MD simulations, the kerogen structure and gas molecules are allowed to relax and the simulation box can swell and shrink freely in an NPT ensemble. In this chapter, we only focus on the kerogen swelling caused by gas adsorption, and the effect of the mechanical compression on the swelling is not taken into consideration. Therefore, the pressure for the imaginary reservoir in GCMC simulations (P_{GCMC}) is set to be equal to the pressure in the NPT ensemble (P_{NPT}) without any effective stress to obtain the maximum adsorption-induced swelling [16]. When the system is equilibrated, the size of this simulation box and the number of gas molecules become stable. The total time for MD simulation is 6000000 fs with a time step of 0.1 fs to achieve the equilibrium state.

7.3 Volumes and adsorption

7.3.1 Volumes

The bulk volume of a kerogen structure under different conditions corresponds to the volume of a simulation cell, which can be obtained by

$$V = L_x \cdot L_y \cdot L_z \tag{7.1}$$

where L_x, L_y, and L_z are the lengths of the simulation cell in the *x*, *y* and *z* directions (cm), respectively.

The bulk volumetric strain of kerogen induced by gas adsorption can be calculated:

$$\varepsilon_b = \frac{V - V_i}{V_i} \times 100\% \tag{7.2}$$

where V is the volume of kerogen at a certain condition (cm^3), V_i is the volume of the initial kerogen structure (cm^3), and ε_b represents the sorption-induced bulk volumetric strain (dimensionless).

An accessible pore volume is defined as the pore volume where a probe particle can penetrate, which is dependent on an adsorbate as reported in recent studies [46,110,156,219,220]. Small atoms such as helium can penetrate small pores, which large molecules such as CH_4 and CO_2 cannot enter. Additionally, helium atoms can also approach closer to a pore surface than other large molecules, resulting in a larger pore void volume. In this chapter, the adsorbate-dependent accessible pore volume of the kerogen is computed based on the algorithm proposed by Herrera et al. [221] using the corresponding probe particles. Therefore, we can calculate the adsorbate-dependent porosity:

$$\phi = \frac{V_p}{V} \tag{7.3}$$

where ϕ is the porosity of the kerogen structure (dimensionless) and V_p is the adsorbate-dependent accessible pore volume (cm^3).

7.3.2 Adsorption

Gas molecules adhesion to a solid surface or filling inside micropores can be defined as adsorption [74–76]. Based on the considered interface volume, adsorption can be divided into absolute adsorption and excess adsorption [98].

An absolute adsorption amount is the gas amount within an adsorbed layer that takes up a certain volume. Due to the extremely small size of pores in the built kerogen structure, the total loading amount of an adsorbent in the kerogen model can be regarded as an absolute adsorbed amount in this study. Because of the experimental limitations, the volume of the adsorbed layer cannot be directly determined. Therefore, it is very difficult to obtain the absolute adsorption amount. The excess adsorption amount that follows Gibb's assumption is calculated by considering an ideal surface:

$$N_e = N_{ab} - \frac{\rho_b V_p}{M} \tag{7.4a}$$

$$N_e = N_{ab} - \frac{\rho_b \phi V_i}{M} \tag{7.4b}$$

where N_{ab} is the absolute adsorption amount (mol); N_e is the excess adsorption amount (mol); M is the molar mass of gas (g/mol); and ρ_b is the density of the bulk phase (g/cm^3).

As mentioned above, the swelling of the kerogen structure occurs due to gas adsorption, and the bulk volume of the kerogen model will change as a function of gas adsorption amount or gas pressure. Therefore, it is not strict to calculate an excess adsorption amount using a constant pore volume, and we define the excess adsorption amount calculated using a constant pore volume as the apparent excess adsorption volume N_e^{app}. Many scholars found that the volumetric strain was related to the absolute adsorption amount [43–46]. In our study, different linear relationships between the volumetric strain and the absolute adsorption amount are obtained for CH_4, C_2H_6 and CO_2, and these relationships can be normalized for different adsorbates, which will be shown later in Section 7.4 and Appendix C. A new coefficient α is introduced, representing the bulk volumetric strain induced by per unit of gas adsorption amount:

$$\varepsilon_b = \alpha N_{ab} \tag{7.5}$$

By combining equations (7.2), (7.3), (7.4), and (7.5), the actual excess adsorption calculated by a variable pore volume can be obtained:

$$N_e^{ac} = N_{ab} - \frac{\rho_b \phi V_i (1+\varepsilon_b)}{M} = N_{ab} - \frac{\rho_b \phi V_i}{M}(1 + \alpha N_{ab}) = N_{ab}\left(1 - \frac{\alpha \rho_b \phi V_i}{M}\right) - \frac{\rho_b \phi V_i}{M} \tag{7.6a}$$

The equation (7.6a) can also be written in terms of the apparent excess adsorption volume N_e^{app}:

$$N_e^{ac} = N_e^{app} - \frac{\alpha N_{ab} \rho_b \phi V_i}{M} \tag{7.6b}$$

Then the actual excess adsorption amount can be obtained by analyzing the variations of the bulk volumetric strain and the absolute adsorption amount at different pressures.

7.4 Results and discussion

In this section, simulation results of gas adsorption are first validated by data from the literature, and the absolute adsorption isotherms for CH_4, C_2H_6 and CO_2 are displayed. Then the variations of the adsorbate-dependent porosity and the volumetric strain as a function of pressure are first illustrated. Additionally, a unified relationship between the bulk volumetric strain and the absolute adsorption amount for different types of adsorbates is also discussed. Finally, the apparent excess adsorption isotherms and the actual excess adsorption isotherms are compared.

7.4.1 Absolute adsorption

The excess adsorption isotherm of CH_4 in simulation is compared with adsorption data from the literature in **Figure A1**. The experimental data for the organic-rich Barnett shale was measured by Zhang et al. and Gasparik et al. and normalized by TOC [86,196]. Similar to the kerogen model in this study, this kind of organic-rich shale is also within the generation window of dry gas. Additionally, the maturities of our model and the Barnett shale are close to each other [222]. Due to the factors including the differences in sample preparation, the inorganic matter content, the pore size distribution, and the pore connectivity, it is difficult to compare gas adsorption isotherms even for similar samples. Therefore, the reasonability, instead of the accuracy of our data compared with data from the literature, should be focused on. As shown in **Figure A1**, the magnitude of our simulation data is within a reasonable range compared with the experimental data. We also compare our data with simulations conducted by Ho et al. [223]. It is found that the adsorption amounts in our simulation are slightly larger than those from the literature. This is because the literature data were obtained for CH_4 adsorption on kerogen at 338 K, which is higher than the temperature of 323 K in our simulation, and a higher temperature generally results in a smaller

adsorption amount. Overall, our simulation data is of great reasonability compared with experimental and simulation data from the literature.

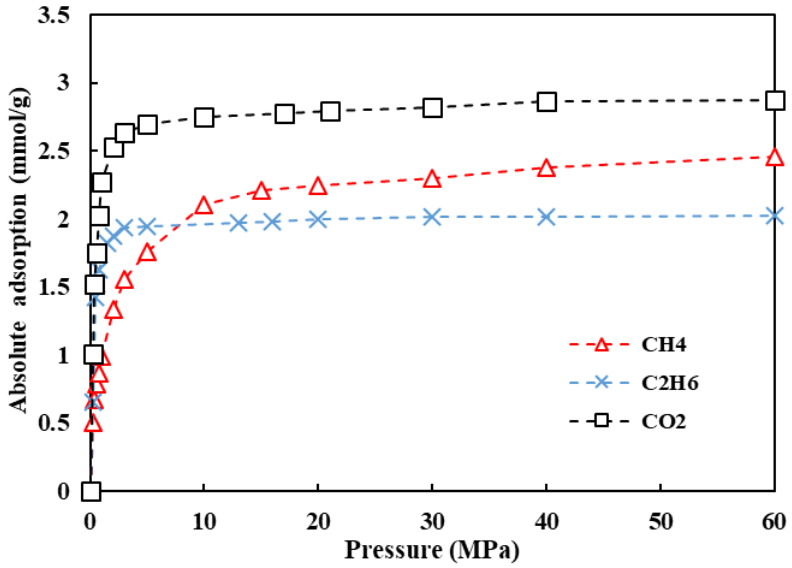

Figure 7. 2 Absolute adsorption isotherms of CH_4, C_2H_6, and CO_2 in kerogen at 323 K with pressure ranging from 0 to 60 MPa.

As a pore size is extremely small in the built kerogen structure (**Figure B1**), the total loading amount of adsorbate is treated as the absolute adsorbed amount in this work. The absolute adsorption isotherms of CH_4, C_2H_6, and CO_2 are shown in **Figure 7.2**. Hereby, the adsorption isotherm of CH_4 is taken as an example. An increase in the absolute adsorption amount with pressure can be observed within a low-pressure range and the absolute adsorption amount gradually reaches a plateau, which indicates that all the adsorption sites are taken by CH_4 molecules. The same trend can be also obtained for absolute adsorption isotherms of C_2H_6 and CO_2; however, the plateaus of the absolute adsorption amount are reached with steep increases at a lower pressure compared with CH_4. At the pressure of 2 MPa, the absolute adsorption amounts for C_2H_6 and CO_2 are 1.936 and 2.634 mmol/g, which are approximately 1.45 and 1.97 times that

for CH_4 (1.336 mmol/g). This indicates that C_2H_6 and CO_2 molecules have stronger affinities for the kerogen model than CH_4 and similar phenomena were also illustrated for gas adsorption in montmorillonite, kerogen, and illite pores [88,224,225]. However, the absolute adsorption amount for C_2H_6 at high pressure is smaller than that for CH_4. This is due to a smaller size of CH_4 than C_2H_6, and more CH_4 can occupy the same pore. Moreover, there are also more pores accessible to CH_4 than C_2H_6. The absolute adsorption capacity for CO_2 is the largest among these three kinds of adsorbates, indicating the strong interaction between CO_2 and the kerogen model and a large CO_2 accessible pore volume.

7.4.2 Changes in porosity and volumetric strain

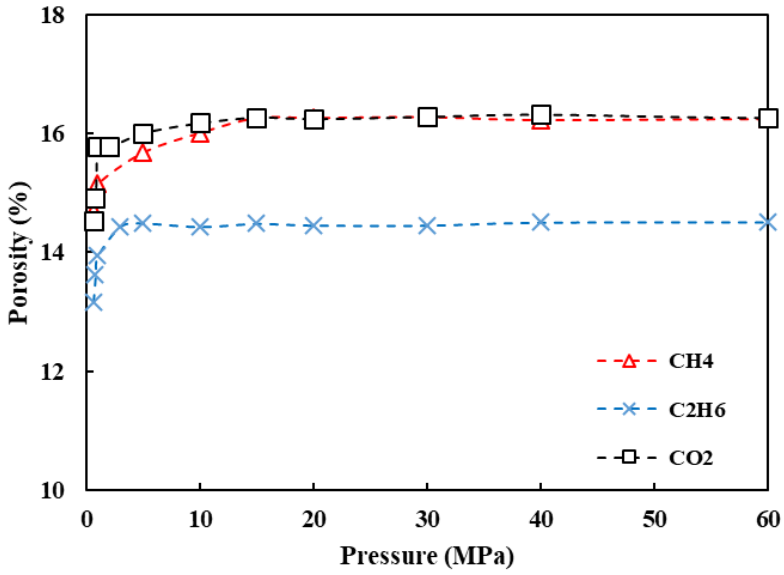

Figure 7. 3 Changes in the adsorbate-dependent porosity for CH_4, C_2H_6 and CO_2 as a function of pressure.

Table 7. 3 Adsorbate-dependent porosity for CH_4, C_2H_6 and CO_2 under different pressures.

Porosity(%)/Pressure (MPa)	1	10	40

CH_4	15.2	16.0	16.2
C_2H_6	13.9	14.4	14.5
CO_2	15.8	16.2	16.3

The pore volumes accessible to CH_4, C_2H_6 and CO_2 are determined using different probes and the corresponding adsorbate-dependent porosities are calculated by equation (7.3) as shown in **Figure 7.3** and **Table 7.3**. Due to the smallest size of CO_2 molecules, the initial porosity of the kerogen structure is 14.88% for CO_2 and it increases to a maximum of 16.35%, which is the largest among these three adsorbates. This is because small molecules can access small pores and approach close to a pore wall, resulting in a large pore volume. Upon gas adsorption, the microstructure of the kerogen changes with increasing pressure and the kerogen swelling can lead to an increase in the porosity within a low-pressure range. As the pressure increases to a certain value, the absolute adsorption amount stabilizes and the kerogen structure does not change much. Therefore, the variation of the porosity is not obvious at high pressure.

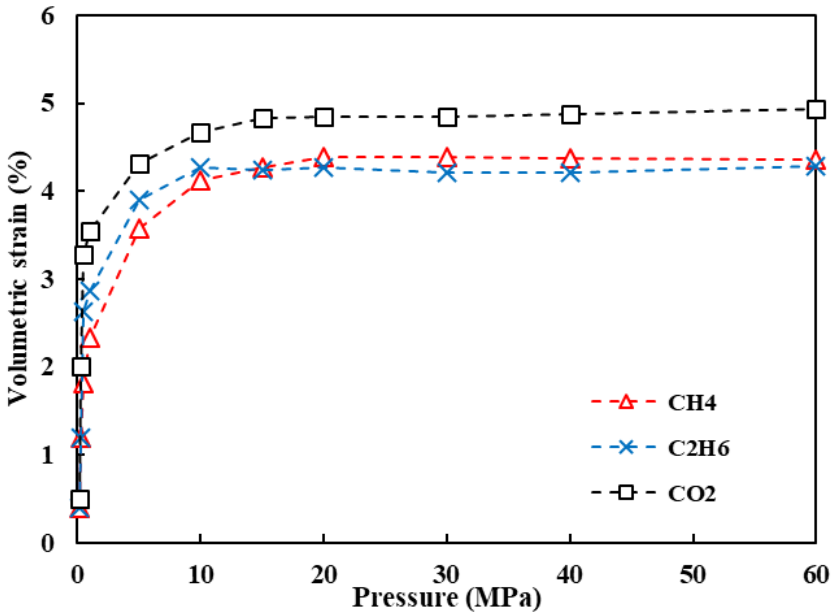

Figure 7. 4 Sorption-induced volumetric strain of kerogen as a function of pressure for CH_4, C_2H_6 and CO_2.

The sorption-induced bulk volumetric strain of kerogen calculated by equation (7.2) is shown in **Figure 7.4**. An increase in the volumetric strain can be found with increasing pressure at low pressure before reaching a plateau, which exhibits a similar characteristic with the absolute adsorption amount. A similar trend in the volumetric strain caused by gas adsorption was also observed in experiments and simulations by many scholars [16,226]. However, a gradual increase in the volumetric strain with an increasing pressure after reaching the maximum was also found [116,117]. This is caused by both swelling and mechanical compressions. Within the low-pressure range, the sorption-induced swelling dominates the changes in the volumetric strain. For high pressure, mechanical compression plays an important role and results in a decrease in the volumetric strain [117]. As indicated before, we investigate the maximum sorption-induced volumetric strain in our study and effects of the mechanical compression are not considered. The maximum volumetric strains for CO_2, CH_4 and C_2H_6 are approximately 4.96%, 4.41%, and 4.28%, respectively, which are in good agreement with the simulation and experimental data [16,117,227]. The kerogen swelling increases with an increasing absolute gas adsorption amount and the maximum swelling upon CO_2 adsorption is the largest ($CO_2 > CH_4 > C_2H_6$).

7.4.3 Sorption-induced swelling

The volumetric strain as a function of the absolute adsorption amount is also plotted in **Figure 7.5**, and a linear relationship between these two parameters is observed. The slopes of the dashed lines represent coefficients α for different gas types in **Figure 7.5**, reflecting the volumetric strain caused by per unit of the absolute adsorption amount. The coefficient α for C_2H_6 is the largest compared with other adsorbates in this study. This is associated with the size of gas molecules, and C_2H_6

molecules with the largest kinetic diameter can result in the largest volumetric strain of kerogens [16]. For a molecule with a large kinetic diameter, it can have a great contact area with a pore wall and the fraction of the pore wall influenced by adsorbed molecules is also large when the amount of adsorbed molecules is the same. On the contrary, a small volumetric strain is induced by a small molecular with the same adsorbed amount.

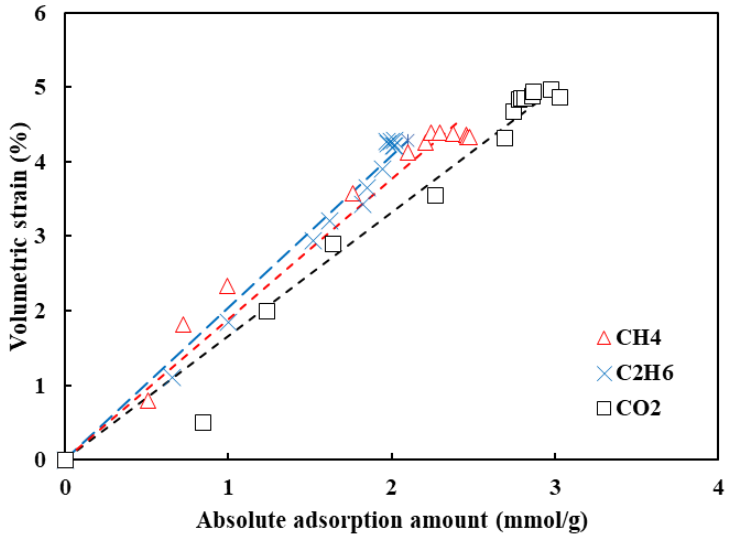

Figure 7. 5 Volumetric strain of kerogen as a function of the absolute adsorption amount induced by CH_4, C_2H_6, and CO_2.

The linear relationships for different adsorbates between the bulk volumetric strain and the absolute adsorption amount can be normalized by equation (C3) (see Appendix C), and the unified relationship between the volumetric strain and the absolute adsorption amount is displayed in **Figure 7.6**. Some data from the literature is also plotted to validate this relationship and it is found that this unified relationship can be successfully used to describe the volumetric strain induced by CH_4, C_2H_6 and CO_2 adsorption in adsorbents such as kerogen, carbon, kaolinite and coal [16,120,121]. The parameter *k* in equation (C1), which is only dependent on adsorbents, is the

largest for coal among these adsorbents, indicating that the swelling of coal is the greatest with the same adsorbed gas amount (**Table 7.4**). For kerogen, parameter *k* is around 4.6 by analyzing data reported by Ho et al. and our simulation data, which can be used to predict the sorption-induced bulk volumetric strain of kerogen.

Table 7. 4 Values of parameter *k* for different adsorbents.

Adsorbent	Coal	Kerogen	Kaolinite	Carbon
k (10^{-2}g·mmol^{-1}·nm$^{-1.02}$)	5.8	around 4.6	2.13	0.079

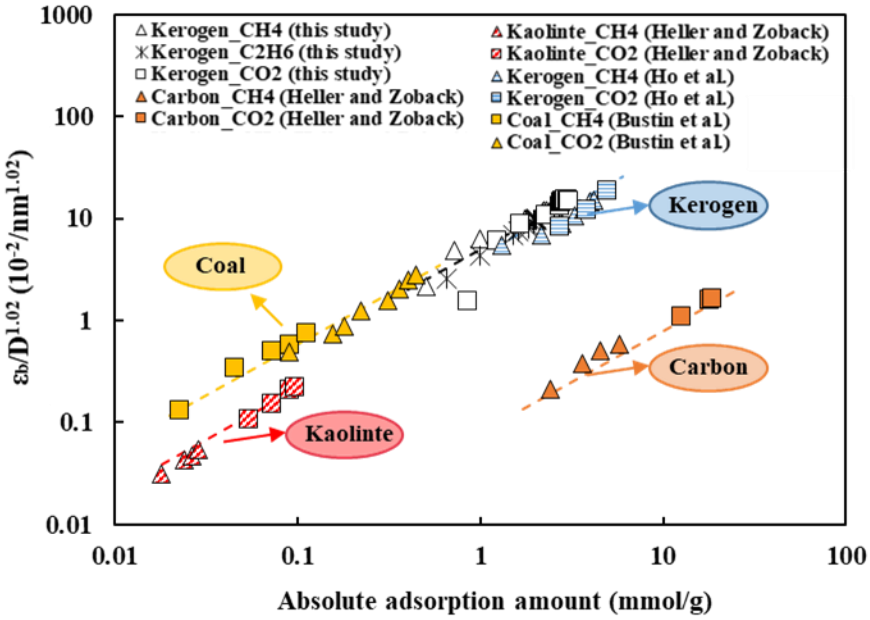

Figure 7. 6 A unified relationship between the bulk volumetric strain and the absolute adsorption amount.

7.4.4 Apparent and actual excess adsorption isotherms

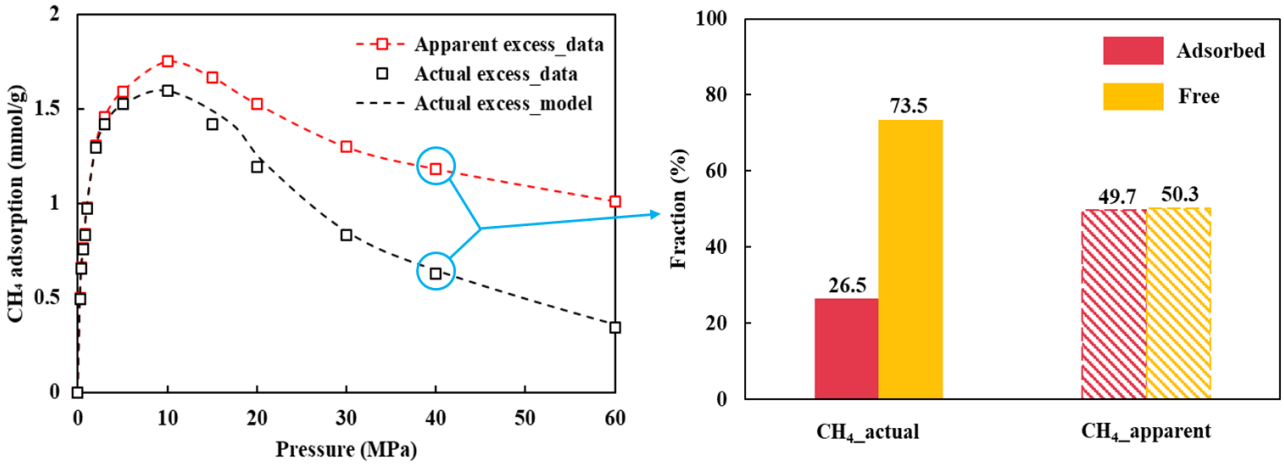

Figure 7. 7 Apparent and actual excess adsorption amounts of CH_4 in kerogens, and fractions of the excess adsorbed amount and free gas amount for CH_4 (323 K, 40 MPa).

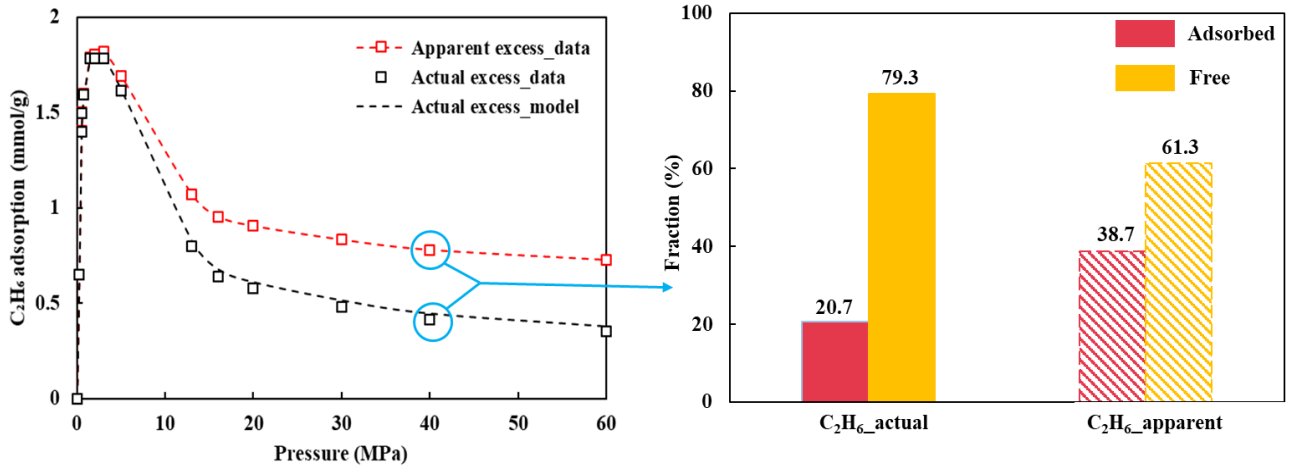

Figure 7. 8 Apparent and actual excess adsorption amounts of C_2H_6 in kerogens, and fractions of the excess adsorbed amount and free gas amount for C_2H_6 (323 K, 40 MPa).

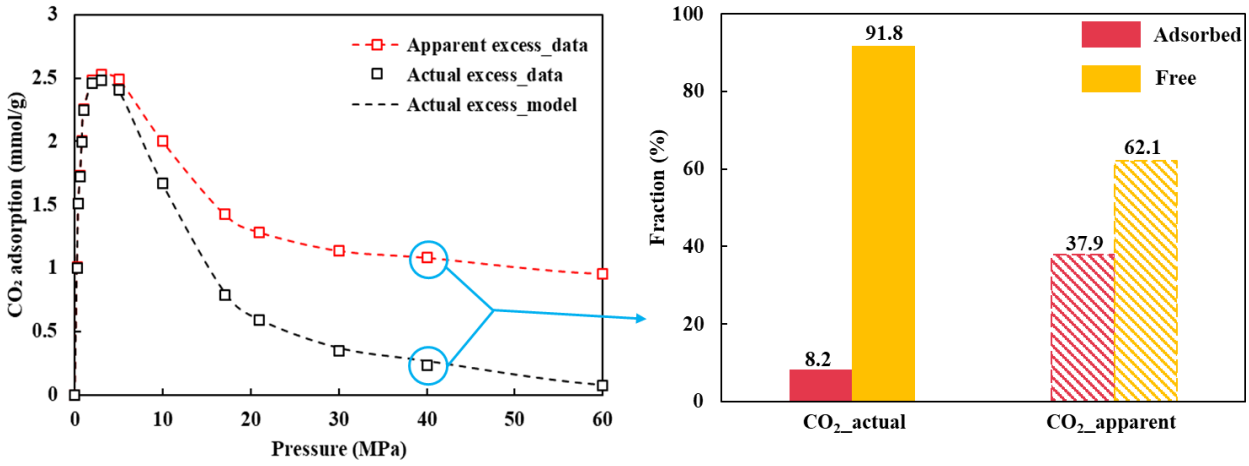

Figure 7. 9 Apparent and actual excess adsorption amounts of CO_2 in kerogens, and fractions of the excess adsorbed amount and free gas amount for CO_2 (323 K, 40 MPa).

After obtaining a relationship between the bulk volumetric strain and the absolute adsorption amount, the actual excess adsorption isotherms can be calculated by equation (7.6a). The actual excess adsorption isotherms calculated by equation (7.6a) and the excess adsorption data calculated by a variable pore volume using equation (7.4a) for CH_4, CO_2 and C_2H_6 are displayed in **figures 7.7-7.9**, and are also compared with the apparent adsorption isotherms calculated using a constant pore volume using equation (7.4a). It is obvious that the excess adsorption isotherms generated by equation (7.6a) have a good agreement with the actual excess adsorption data, indicating that the actual adsorption amount can be effectively obtained based on our model. Moreover, a difference between the actual and apparent excess adsorption amounts is not obvious within a low-pressure range. However, it becomes greater as the pressure increases. According to equation (7.4a), the density of the bulk phase is large at high pressures and a small change in the pore volume can still result in a large variation in $\rho_b V_p$, which leads to a large difference in the excess adsorption amount. Therefore, the excess adsorption amounts at high pressures are

overestimated without considering effects of the kerogen swelling. The greatest discrepancy between the actual and the apparent excess adsorption can be witnessed for CO_2 at high pressures because the swelling of the kerogen structure is the largest upon CO_2 adsorption.

The fractions of the free gas amount and the excess adsorbed gas amount are calculated under the reservoir conditions (323 K, 40 MPa) based on the apparent and actual excess adsorption isotherms for CH_4, CO_2, and C_2H_6, respectively. As shown in **figures 7.7-7.9**, the kerogen swelling has significant effects on the estimations of fractions of the free gas amount and the excess adsorbed gas amount. According to CH_4 excess adsorption isotherms, the proportions of the excess adsorbed gas amount are 26.5% and 49.7% for the actual and apparent excess isotherms, sequentially. Apparently, the discrepancy in the determination of fractions of the free and excess adsorbed gas amounts of CO_2 is the greatest, which is induced by the largest kerogen swelling upon CO_2 adsorption. Therefore, it is of great necessity to take the effects of kerogen swelling into consideration, which can further result in accurate estimations of the free gas amount and the excess adsorbed amount in shale gas reservoirs. Furthermore, the prediction of hydrocarbon production and CO_2 sequestration in shale reservoirs can be significantly influenced by considering the kerogen swelling.

7.5 Limitations

Besides gas adsorption, the mechanical compression can also affect kerogen swelling or shrinkage, further resulting in inappropriate excess adsorption isotherms [228–231]. Natural pores can be compressed by the overburden with a decrease in gas pressure in the pores, which leads to a reduction in the total pore volume. When gas adsorption is measured in a core sample with a constant confining stress, gradual changes in the pore volume of the sample are found in each

pressure-step measurement [232]. Sometimes, gas adsorption amounts of a crushed sample are measured without any confining stress in experiments, and the effects of the mechanical compression on swelling or shrinkage cannot be determined.

The volumetric strain of kerogen induced by gas adsorption and the volumetric strain of coal samples induced by mechanical compression are compared in **Table 7.5** [231]. The volumetric strain caused by mechanical compression is relatively smaller than that caused by gas adsorption, but it can still have effects on swelling and shrinkage. We only focus on the maximum sorption-induced kerogen swelling without considering the mechanical compression in the current study, and the mechanical compression will be investigated in detail in our next research.

Table 7. 5 Volumetric strain induced by gas adsorption and mechanical compression.

Volumetric strain induced by CO_2 sorption (%)	Volumetric strain induced by CH_4 sorption (%)	Volumetric strain induced by C_2H_6 sorption (%)	Volumetric strain induced by mechanical compression (%)
4.96	4.41	4.28	1.44-2.2

7.6 Summary

In this chapter, hybrid GCMC/MD simulations are conducted to investigate gas adsorption in shale coupling kerogen swelling under reservoir conditions. A unified relationship between the bulk volumetric strain and an absolute adsorption amount is developed. Additionally, a theoretical model for calculating the excess adsorption amount is proposed considering the effects of kerogen swelling. Then actual excess adsorption isotherms are compared with apparent adsorption isotherms. The main conclusions can be reached as follows:

1. The plateaus of the absolute adsorption isotherms for C_2H_6 and CO_2 are reached with steep increases at a lower pressure compared with CH_4, indicating that C_2H_6 and CO_2 have stronger affinities for the kerogen model than CH_4. However, the maximum absolute adsorption amount for C_2H_6 is smaller than that for CH_4 and CO_2, which is associated with a gas molecular size. Due to a smaller size of CH_4 than C_2H_6, more pores can be accessible to CH_4 than C_2H_6 and more CH_4 can occupy the pores. An increase in porosity is observed within a low-pressure range, but the variation of the porosity is not obvious at high pressure when the absolute adsorption amount is stabilized.
2. The kerogen swelling increases with an increase in the absolute gas adsorption amount and the maximum swelling upon CO_2 adsorption is the largest (CO_2 > CH_4 > C_2H_6). Additionally, a linear relationship between the absolute adsorbed gas amount and the volumetric strain can also be obtained and the slope reflecting the volumetric strain caused by per unit of the absolute adsorption amount for C_2H_6 is the largest. This is related to the size of gas molecules, and C_2H_6 molecules with the largest kinetic diameter can result in the largest volumetric strain of kerogens.
3. The actual excess adsorption isotherms generated by our proposed model have a good agreement with the actual excess adsorption data, which shows a large discrepancy compared to the apparent adsorption isotherms, especially at high pressures. The greatest discrepancy of the fraction of the free gas amount (up to 29.7%) can be witnessed for CO_2 because the swelling of the kerogen structure is the largest upon CO_2 adsorption.

Chapter 8 Conclusions and recommendations

8.1 Conclusions

This thesis first provides a literature review on characteristics of shale gas reservoirs and gas adsorption in shale formations in Chapter 2. Then basic knowledge of GCMC and MD simulations is introduced in Chapter 3. From Chapters 4-7, rock wettability indicating interactions between gas and shale adsorbents, and gas adsorption in shale reservoirs are investigated by GCMC and MD simulations.

Novelties of our work are summarized:

1. Water contact angles on the surfaces of shale organic matter in the atmospheres of CO_2 and CH_4 under reservoir conditions are studied, which are of great significance to CO_2 sequestration and enhanced gas recovery processes. Based on our results, we can have a better understanding of the rock wettabilities and water contact angles describing interactions between CO_2, CH_4, brine and shale formations. Influencing factors such as temperature, pressure and mole fraction of gas are also investigated. The injecting timing of CO_2 and temperature of injected CO_2 can be optimized in field development to improve the displacement efficiency.
2. We use an adsorbate-based volume to calculate the excess adsorption isotherms, contributing to an accurate estimation of GIP and the proportions of free and adsorbed gas in shale. However, in other literature, excess adsorption isotherms of methane are always calculated by helium-based volume, and results in an underestimated of adsorbed gas.

3. Realistic pore models, such as kerogen, are used in our study to simulate organic pores in shale. As is known, the pore volume in shale is influenced by sorption-induced swelling and shrinkage. However, the pore in simulation is kept rigid and the pore volume is assumed constant to simplify the simulation in other literature. In our work, the pore will not be kept rigid and it can change during adsorption. We determine the pore volume under different pressure and temperatures instead of using a constant volume to generate the adsorption isotherms. A unified relationship between volumetric strain and an absolute adsorption amount is developed for different adsorbates. A theoretical model for calculating excess adsorption isotherms coupling swelling is also proposed.

Main conclusions of this thesis are described in the following four parts based on Chapters 5-7.

8.1.1 Molecular dynamics computations of brine-CO_2/CH_4-shale contact angles

An increase in contact angle with temperature below the critical temperature is greater than that above the critical temperature. Temperature generally has a more significant effect on the water contact angle under an intermediate-pressure condition than a high-pressure condition. The wettability behavior of a CO_2-water-shale organic matter system turns from a neutrally-wet state to a CO_2-wet state approximately at the critical pressure of CO_2, which contributes to a large CO_2 adsorption capacity in the system. The salinity and ion types have a minor impact on the brine contact angle in a CO_2-brine-shale system. However, high ionic strength and strong adsorption ability of ions can still result in large brine contact angles. Moreover, the water contact angle decreases as the CH_4 fraction of a CO_2/CH_4 mixture increases. The organic matter in shale has a stronger affinity for CO_2 than CH_4, which results in a more CO_2-wet system and a higher CO_2 adsorption capacity than CH_4.

8.1.2 Suitable experimental conditions for determination of void volume by helium expansion tests

The density of an adsorbed phase can be rather close to but never smaller than the bulk density at extremely high pressure due to the existence of a strong interaction between a pore wall and adsorbates. Therefore, helium adsorption effects on the void volume determination can be reduced but not totally eliminated. A negative excess amount can be observed at high pressures when the isotherms are calculated by overestimated void volumes and a larger overestimation leads to an earlier negative excess adsorption phenomenon. A void volume determined under a moderate-pressure condition at 500 K is reasonable for excess isotherm calculations and an adsorption mechanism investigation.

8.1.3 Methane-based volumes for methane adsorption

A physical void volume is always larger than both helium-based and methane-based pore volumes because of a finite size of adsorbate molecules. Therefore, a physical volume should be calibrated before using it to calculate the excess adsorption amounts. Use of a helium-based volume in the calculation of the excess amount of methane adsorption can lead to a negative excess amount at high pressures, which has no physical meaning. An accessible volume probed by methane molecules can be well represented by a simulated methane-based volume, and it is accurate to apply it to calculations of excess amounts and an investigation of methane adsorption mechanisms. A high excess adsorption amount is observed in small pores. The maximum value of excess adsorption isotherms occurs at lower pressure in smaller pores because of the high adsorption potential exerted by pore walls. The estimation of the contribution of a free gas amount and an adsorbed amount in shale gas reservoirs can be greatly affected by a void volume used in

calculations of adsorption isotherms, and this can further influence the prediction of shale gas production.

8.1.4 Gas adsorption in shale kerogens coupling sorption-induced swelling

C_2H_6 and CO_2 have stronger affinities for a kerogen model than CH_4. However, the maximum absolute adsorption amount for C_2H_6 is smaller than that for CH_4 and CO_2, which is associated with a gas molecular size. More pores can be accessible to CH_4 than C_2H_6 and a larger amount of CH_4 can occupy the pores because of a smaller size of CH_4. The kerogen swelling increases with an increase in the absolute gas adsorption amount and the maximum swelling upon CO_2 adsorption is the largest ($CO_2 > CH_4 > C_2H_6$). A linear relationship between the absolute adsorbed gas amount and the volumetric strain is obtained and the slope reflecting the volumetric strain caused by a unit of the absolute adsorption amount for C_2H_6 is the largest among these three molecules. This is because C_2H_6 molecules with the largest kinetic diameter can contribute to the largest volumetric strain of kerogens. The actual excess adsorption isotherms generated by our proposed model have a good agreement with the actual excess adsorption data. Therefore, use of our proposed model coupling the kerogen swelling can accurately estimate the free and adsorbed gas amounts in shale reservoirs.

8.2 Recommendations

This study has provided a deep understanding of gas adsorption in shales and a theoretical adsorption model coupling the kerogen swelling, with which the contributions of the free gas and adsorbed gas in the shale reservoirs can be accurately described, further improving the industrial development strategy.

However, there are still recommendations for future work:

1. A graphene sheet with different functional groups can be established with a more realistic TOC content that is close to that of organic-rich shale for an investigation of rock wettability of shale formations. Moreover, effects of the surface roughness can also be considered.
2. In addition to gas adsorption, mechanical compression can also have an effect on kerogen swelling or shrinkage, which needs to be further discussed.
3. Inorganic pore models, such as montmorillonite and elite, can also be applied for an investigation of the adsorption mechanisms in inorganic pores in shale.
4. In the current study, effects of moisture and water films on gas adsorption in shales, especially clay minerals are not considered, which can be analyzed by both simulation and analytical work.

References

[1] Chong J, Simikian M. Shale gas in Canada: Resource potential, current production and economic implications. Library of Parliament= Bibliothèque du Parlement; 2014.

[2] Regulator AE. Alberta's energy reserves 2014 and supply/demand outlook 2015–2024. Stat Ser 2015–98 2015.

[3] IEA. Technology Roadmap Carbon Capture and Storage–2013 Edition 2013.

[4] Yu X, Ahmadinia M, Shariatipour SM, Lawton D, Osadetz K, Saeedfar A. Impact of Reservoir Permeability, Permeability Anisotropy and Designed Injection Rate on CO2 Gas Behavior in the Shallow Saline Aquifer at the CaMI Field Research Station, Brooks, Alberta. Nat Resour Res 2019. https://doi.org/10.1007/s11053-019-09604-3.

[5] UNCCS. Climate Action Now: Summary for Policymakers 2015 2015.

[6] Zhou J, Jin Z, Luo KH. The role of brine in gas adsorption and dissolution in kerogen nanopores for enhanced gas recovery and CO2 sequestration. Chem Eng J 2020;399:125704. https://doi.org/https://doi.org/10.1016/j.cej.2020.125704.

[7] Yu X, Li J, Chen Z, Wu K, Zhang L, Hui G, et al. Molecular dynamics computations of brine-CO2/CH4-shale contact angles: Implications for CO2 sequestration and enhanced gas recovery. Fuel 2020;280:118590. https://doi.org/10.1016/j.fuel.2020.118590.

[8] Lu X-C, Li F-C, Watson AT. Adsorption measurements in Devonian shales. Fuel 1995;74:599–603.

[9] Curtis JB. Fractured shale-gas systems. Am Assoc Pet Geol Bull 2002;86:1921–38.

[10] Tang X, Ripepi N, Luxbacher K, Pitcher E. Adsorption models for methane in shales: Review, comparison, and application. Energy & Fuels 2017;31:10787–801.

[11] Hu K, Mischo H. Modeling High-Pressure Methane Adsorption on Shales with a Simplified Local Density Model. ACS Omega 2020;5:5048–60. https://doi.org/10.1021/acsomega.9b03978.

[12] Ruppel T, Grein C, Bienstock D. Adsorption of methane/ethane mixtures on dry coal at elevated pressure. Fuel 1972;51:297–303.

[13] Zhang T, Ellis GS, Ruppel SC, Milliken K, Yang R. Effect of organic-matter type and thermal maturity on methane adsorption in shale-gas systems. Org Geochem 2012;47:120–31.

[14] Zhang J, Clennell MB, Dewhurst DN, Liu K. Combined Monte Carlo and molecular dynamics simulation of methane adsorption on dry and moist coal. Fuel 2014;122:186–97. https://doi.org/10.1016/j.fuel.2014.01.006.

[15] Vidal D, Malbrunot P, Guengant L, Vermesse J, Bose TK, Chahine R. Measurement of physical adsorption of gases at high pressure. Rev Sci Instrum 1990;61:1314–8.

[16] Ho TA, Wang Y, Criscenti LJ. Chemo-mechanical coupling in kerogen gas adsorption/desorption. Phys Chem Chem Phys 2018;20:12390–5. https://doi.org/10.1039/c8cp01068d.

[17] Tesson S, Firoozabadi A. Deformation and Swelling of Kerogen Matrix in Light

Hydrocarbons and Carbon Dioxide. J Phys Chem C 2019;123:29173–83. https://doi.org/10.1021/acs.jpcc.9b04592.

[18] Huang L, Ning Z, Wang Q, Qi R, Cheng Z, Wu X, et al. Kerogen deformation upon CO2/CH4 competitive sorption: Implications for CO2 sequestration and enhanced CH4 recovery. J Pet Sci Eng 2019;183:106460. https://doi.org/10.1016/j.petrol.2019.106460.

[19] Yao J, Sun H, Fan D, Wang C, Sun Z. Numerical simulation of gas transport mechanisms in tight shale gas reservoirs. Pet Sci 2013;10:528–37.

[20] Wu T, Zhao H, Tesson S, Firoozabadi A. Absolute adsorption of light hydrocarbons and carbon dioxide in shale rock and isolated kerogen. Fuel 2019;235:855–67. https://doi.org/10.1016/j.fuel.2018.08.023.

[21] Behrang A, Mohammadmoradi P, Taheri S, Kantzas A. A theoretical study on the permeability of tight media; Effects of slippage and condensation. Fuel 2016;181:610–7. https://doi.org/10.1016/j.fuel.2016.05.048.

[22] Tran H, Sakhaee-Pour A. Viscosity of shale gas. Fuel 2017;191:87–96. https://doi.org/10.1016/j.fuel.2016.11.062.

[23] Xu Y, Adefidipe O, Dehghanpour H. A flowing material balance equation for two-phase flowback analysis. J Pet Sci Eng 2016;142:170–85. https://doi.org/10.1016/j.petrol.2016.01.018.

[24] Yuan J, Luo D, Feng L. A review of the technical and economic evaluation techniques for shale gas development. Appl Energy 2015;148:49–65.

https://doi.org/10.1016/j.apenergy.2015.03.040.

[25] Kuuskraa V, Stevens SH, Moodhe KD. Technically recoverable shale oil and shale gas resources: an assessment of 137 shale formations in 41 countries outside the United States. US Energy Information Administration, US Department of Energy; 2013.

[26] Hill RJ, Zhang E, Katz BJ, Tang Y. Modeling of gas generation from the Barnett shale, Fort Worth Basin, Texas. Am Assoc Pet Geol Bull 2007;91:501–21.

[27] Magoon LB, Dow WG. The petroleum system: chapter 1: Part I. Introduction 1994.

[28] Bernard S, Horsfield B, Schulz H-M, Schreiber A, Wirth R, Vu TTA, et al. Multi-scale detection of organic and inorganic signatures provides insights into gas shale properties and evolution. Geochemistry 2010;70:119–33.

[29] Martini AM, Budai JM, Walter LM, Schoell M. Microbial generation of economic accumulations of methane within a shallow organic-rich shale. Nature 1996;383:155–8.

[30] Tomlinson CW. The origin of red beds: a study of the conditions of origin of the Permo-Carboniferous and Triassic red beds of the western United States. J Geol 1916;24:153–79.

[31] Hosterman JW, Whitlow SI. Munsell color value as related to organic carbon in Devonian shale of Appalachian basin. Am Assoc Pet Geol Bull 1981;65:333–5.

[32] Jarvie DM, Hill RJ, Ruble TE, Pollastro RM. Unconventional shale-gas systems: The Mississippian Barnett Shale of north-central Texas as one model for thermogenic shale-gas assessment. Am Assoc Pet Geol Bull 2007;91:475–99.

[33] Jarvie DM. Total organic carbon (TOC) analysis: Chapter 11: Geochemical methods and

exploration 1991.

[34] Cooles GP, Mackenzie As, Quigley TM. Calculation of petroleum masses generated and expelled from source rocks. Org Geochem 1986;10:235–45.

[35] Hunt JM. Petroleum geochemistry and geology 1995.

[36] Tissot BP, Welte DH. Petroleum formation and occurence, second revised and enlarge edition 1984.

[37] Cui X, Bustin AMM, Bustin RM. Measurements of gas permeability and diffusivity of tight reservoir rocks: different approaches and their applications. Geofluids 2009;9:208–23.

[38] Bustin RM, Bustin AMM, Cui A, Ross D, Pathi VM. Impact of shale properties on pore structure and storage characteristics. SPE shale gas Prod. Conf., Society of Petroleum Engineers; 2008.

[39] Gasparik M, Ghanizadeh A, Bertier P, Gensterblum Y, Bouw S, Krooss BM. High-pressure methane sorption isotherms of black shales from the Netherlands. Energy & Fuels 2012;26:4995–5004.

[40] Yaalon DH. Mineral composition of the average shale: Clay Minerals Bull., v. 5 1962.

[41] Rani S, Padmanabhan E, Prusty BK. Review of gas adsorption in shales for enhanced methane recovery and CO2 storage. J Pet Sci Eng 2019;175:634–43.

[42] Curtis ME, Ambrose RJ, Sondergeld CH, Rai CS. Investigation of the relationship between organic porosity and thermal maturity in the Marcellus Shale. North Am. Unconv. gas Conf. Exhib., Society of Petroleum Engineers; 2011.

[43] Passey QR, Bohacs K, Esch WL, Klimentidis R, Sinha S. From oil-prone source rock to gas-producing shale reservoir-geologic and petrophysical characterization of unconventional shale gas reservoirs. Int. oil gas Conf. Exhib. China, Society of Petroleum Engineers; 2010.

[44] Volzone C, Rinaldi JO, Ortiga J. N2 and CO2 Adsorption by TMA-and HDP-Montmorillonites. Mater Res 2002;5:475–9.

[45] Venaruzzo JL, Volzone C, Rueda ML, Ortiga J. Modified bentonitic clay minerals as adsorbents of CO, CO2 and SO2 gases. Microporous Mesoporous Mater 2002;56:73–80.

[46] Ross DJK, Marc Bustin R. Impact of mass balance calculations on adsorption capacities in microporous shale gas reservoirs. Fuel 2007;86:2696–706. https://doi.org/10.1016/j.fuel.2007.02.036.

[47] Britt LK, Schoeffler J. The geomechanics of a shale play: what makes a shale prospective. SPE East. Reg. Meet., Society of Petroleum Engineers; 2009.

[48] Binnion M. How the technical differences between shale gas and conventional gas projects lead to a new business model being required to be successful. Mar Pet Geol 2012;31:3–7.

[49] Rouquerol J, Avnir D, Fairbridge CW, Everett DH, Haynes JM, Pernicone N, et al. Recommendations for the characterization of porous solids (Technical Report). Pure Appl Chem 1994;66:1739–58.

[50] Loucks RG, Reed RM, Ruppel SC, Hammes U. Spectrum of pore types and networks in mudrocks and a descriptive classification for matrix-related mudrock pores. Am Assoc Pet

Geol Bull 2012;96:1071–98. https://doi.org/10.1306/08171111061.

[51] Guo W, Hu Z, Zhang X, Yu R, Wang L. Shale gas adsorption and desorption characteristics and its effects on shale permeability. Energy Explor Exploit 2017;35:463–81.

[52] Rine J, Dorsey W, Floyd M, Lasswell P. A comparative sem study of pore types and porosity distribution in high to low porosity samples from selected gas-shale formations 2010.

[53] Dake LP. Fundamentals of reservoir engineering. Elsevier; 1983.

[54] Morrow NR. Wettability and its effect on oil recovery. J Pet Technol 1990;42:1–476.

[55] Arif M, Lebedev M, Barifcani A, Iglauer S. CO2 storage in carbonates: Wettability of calcite. Int J Greenh Gas Control 2017;62:113–21. https://doi.org/https://doi.org/10.1016/j.ijggc.2017.04.014.

[56] Shojai Kaveh N, Barnhoorn A, Wolf K-H. Wettability evaluation of silty shale caprocks for CO2 storage. Int J Greenh Gas Control 2016;49:425–35. https://doi.org/10.1016/J.IJGGC.2016.04.003.

[57] Chaudhary K, Guiltinan EJ, Cardenas MB, Maisano JA. Wettability measurement under high P-T conditions using X-ray imaging with application to the brine-supercritical CO2 system. Geochemistry, Geophys Geosystems 2015:2858–64. https://doi.org/10.1002/2015GC005936.Received.

[58] Pan B, Li Y, Wang H, Jones F, Iglauer S. CO2 and CH4 Wettabilities of Organic-Rich Shale. Energy and Fuels 2018;32:1914–22. https://doi.org/10.1021/acs.energyfuels.7b01147.

[59] Iglauer S, Pentland CH, Busch A. CO2 wettability of seal and reservoir rocks and the implications for carbon geo-sequestration. Water Resour Res 2015;51:729–74.

[60] Lan Q, Xu M, Binazadeh M, Dehghanpour H, Wood JM. A comparative investigation of shale wettability: The significance of pore connectivity. J Nat Gas Sci Eng 2015;27:1174–88.

[61] Hu Y. Dependence of organic pore wettability on kerogen maturity: A water droplet microscopic simulation study. Proc - SPE Annu Tech Conf Exhib 2014;7:5621–32. https://doi.org/10.2118/173476-stu.

[62] Arif M, Lebedev M, Barifcani A, Iglauer S. Influence of shale-total organic content on CO2 geo-storage potential. Geophys Res Lett 2017;44:8769–75. https://doi.org/10.1002/2017GL073532.

[63] Guiltinan EJ, Cardenas MB, Bennett PC, Zhang T, Espinoza DN. The effect of organic matter and thermal maturity on the wettability of supercritical CO2 on organic shales. Int J Greenh Gas Control 2017;65:15–22. https://doi.org/10.1016/J.IJGGC.2017.08.006.

[64] Bohloli B, Skurtveit E, Grande L, Titlestad GO, Børresen M, Johnsen Ø, et al. Evaluation of reservoir and cap-rock integrity for the Longyearbyen CO2 storage pilot based on laboratory experiments and injection tests 2014.

[65] Busch A, Bertier P, Gensterblum Y, Rother G, Spiers CJ, Zhang M, et al. On sorption and swelling of CO 2 in clays. Geomech Geophys Geo-Energy Geo-Resources 2016;2:111–30.

[66] Roshan H, Al-Yaseri AZ, Sarmadivaleh M, Iglauer S. On wettability of shale rocks. J

Colloid Interface Sci 2016;475:104–11. https://doi.org/10.1016/J.JCIS.2016.04.041.

[67] Liang L, Luo D, Liu X, Xiong J. Experimental study on the wettability and adsorption characteristics of Longmaxi Formation shale in the Sichuan Basin, China. J Nat Gas Sci Eng 2016;33:1107–18. https://doi.org/10.1016/J.JNGSE.2016.05.024.

[68] Bachu S. CO2 storage in geological media: Role, means, status and barriers to deployment. Prog Energy Combust Sci 2008;34:254–73. https://doi.org/10.1016/j.pecs.2007.10.001.

[69] Tao Z, Clarens A. Estimating the carbon sequestration capacity of shale formations using methane production rates. Environ Sci Technol 2013;47:11318–25.

[70] Al-Yaseri AZ, Roshan H, Lebedev M, Barifcani A, Iglauer S. Dependence of quartz wettability on fluid density. Geophys Res Lett 2016;43:3771–6.

[71] Ren Q-Y, Chen G-J, Yan W, Guo T-M. Interfacial tension of (CO2+ CH4)+ water from 298 K to 373 K and pressures up to 30 MPa. J Chem Eng Data 2000;45:610–2.

[72] Liu Y, Li HA, Okuno R. Measurements and modeling of interfacial tension for CO2/CH4/brine systems under reservoir conditions. Ind Eng Chem Res 2016;55:12358–75.

[73] Chen C, Chai Z, Shen W, Li W. Effects of Impurities on CO2 Sequestration in Saline Aquifers: Perspective of Interfacial Tension and Wettability. Ind & Eng Chem Res 2017;57:371–9. https://doi.org/10.1021/acs.iecr.7b03873.

[74] Adisa OO, Cox BJ, Hill JM. Methane storage in molecular nanostructures. Nanoscale 2012;4:3295–307.

[75] Li J, Wu K, Chen Z, Wang W, Yang B, Wang K, et al. Effects of energetic heterogeneity

on gas adsorption and gas storage in geologic shale systems. Appl Energy 2019;251:113368. https://doi.org/10.1016/j.apenergy.2019.113368.

[76] Bai J, Kang Y, Chen M, Liang L, You L, Li X. Investigation of multi-gas transport behavior in shales via a pressure pulse method. Chem Eng J 2019;360:1667–77.

[77] Li J, Wu K, Chen Z, Wang K, Luo J, Xu J, et al. On the Negative Excess Isotherms for Methane Adsorption at High Pressure: Modeling and Experiment. SPE J 2019.

[78] Wu K, Li X, Guo C, Wang C, Chen Z. A unified model for gas transfer in nanopores of shale-gas reservoirs: coupling pore diffusion and surface diffusion. Spe J 2016;21:1–583.

[79] Li J, Chen Z, Wu K, Wang K, Luo J, Feng D, et al. A multi-site model to determine supercritical methane adsorption in energetically heterogeneous shales. Chem Eng J 2018;349:438–55. https://doi.org/10.1016/j.cej.2018.05.105.

[80] Ross DJK, Bustin R. The importance of shale composition and pore structure upon gas storage potential of shale gas reservoirs. Mar Pet Geol 2009;26:916–27. https://doi.org/10.1016/j.marpetgeo.2008.06.004.

[81] Chalmers GRL, Bustin RM. The organic matter distribution and methane capacity of the Lower Cretaceous strata of Northeastern British Columbia, Canada. Int J Coal Geol 2007;70:223–39.

[82] Weniger P, Kalkreuth W, Busch A, Krooss BM. High-pressure methane and carbon dioxide sorption on coal and shale samples from the Paraná Basin, Brazil. Int J Coal Geol 2010;84:190–205.

[83] Bakshi T, Prusty BK, Pathak K, Pal SK. Pore characteristics of Damodar valley shale and their effect on gas storage potential. J Pet Sci Eng 2018;162:725–35.

[84] Chareonsuppanimit P, Mohammad SA, Robinson Jr RL, Gasem KAM. High-pressure adsorption of gases on shales: Measurements and modeling. Int J Coal Geol 2012;95:34–46.

[85] Chalmers GRL, Bustin RM. Lower Cretaceous gas shales in northeastern British Columbia, Part I: geological controls on methane sorption capacity. Bull Can Pet Geol 2008;56:1–21.

[86] Gasparik M, Bertier P, Gensterblum Y, Ghanizadeh A, Krooss BM, Littke R. Geological controls on the methane storage capacity in organic-rich shales. Int J Coal Geol 2014;123:34–51.

[87] Schettler Jr PD, Parmely CR. Contributions to total storage capacity in Devonian shales. SPE East. Reg. Meet., Society of Petroleum Engineers; 1991.

[88] Chen G, Zhang J, Lu S, Pervukhina M, Liu K, Xue Q, et al. Adsorption Behavior of Hydrocarbon on Illite. Energy and Fuels 2016;30:9114–21. https://doi.org/10.1021/acs.energyfuels.6b01777.

[89] Yang N, Liu S, Yang X. Molecular simulation of preferential adsorption of CO 2 over CH 4 in Na-montmorillonite clay material. Appl Surf Sci 2015;356:1262–71. https://doi.org/10.1016/j.apsusc.2015.08.101.

[90] Zhang J, Choi SK. Molecular dynamics simulation of methane in potassium montmorillonite clay hydrates. J Phys B At Mol Opt Phys 2006;39:3839–48.

https://doi.org/10.1088/0953-4075/39/18/013.

[91] Ji L, Zhang T, Milliken KL, Qu J, Zhang X. Experimental investigation of main controls to methane adsorption in clay-rich rocks. Appl Geochemistry 2012;27:2533–45.

[92] Herrle JO, Pross J, Friedrich O, Kößler P, Hemleben C. Forcing mechanisms for mid-Cretaceous black shale formation: evidence from the Upper Aptian and Lower Albian of the Vocontian Basin (SE France). Palaeogeogr Palaeoclimatol Palaeoecol 2003;190:399–426.

[93] Krooss BM, Van Bergen F, Gensterblum Y, Siemons N, Pagnier HJM, David P. High-pressure methane and carbon dioxide adsorption on dry and moisture-equilibrated Pennsylvanian coals. Int J Coal Geol 2002;51:69–92. https://doi.org/10.1016/S0166-5162(02)00078-2.

[94] Li J, Li X, Wu K, Wang X, Shi J, Yang L, et al. Water sorption and distribution characteristics in clay and shale: effect of surface force. Energy & Fuels 2016;30:8863–74.

[95] Li J, Li X, Wang X, Li Y, Wu K, Shi J, et al. Water distribution characteristic and effect on methane adsorption capacity in shale clay. Int J Coal Geol 2016;159:135–54. https://doi.org/10.1016/j.coal.2016.03.012.

[96] Zhang J, Clennell MB, Liu K, Pervukhina M, Chen G, Dewhurst DN. Methane and Carbon Dioxide Adsorption on Illite. Energy and Fuels 2016;30:10643–52. https://doi.org/10.1021/acs.energyfuels.6b01776.

[97] Chen G, Lu S, Zhang J, Xue Q, Han T, Xue H, et al. Keys to linking GCMC simulations

and shale gas adsorption experiments. Fuel 2017;199:14–21.

[98] Myers AL, Monson PA. Adsorption in porous materials at high pressure: Theory and experiment. Langmuir 2002;18:10261–73. https://doi.org/10.1021/la026399h.

[99] Do DD, Do HD, Fan C, Nicholson D. On the existence of negative excess isotherms for argon adsorption on graphite surfaces and in graphitic pores under supercritical conditions at pressures up to 10,000 atm. Langmuir 2010;26:4796–806. https://doi.org/10.1021/la903549f.

[100] Maggs FAP, Schwabe PH, Williams JH. Adsorption of helium on carbons: influence on measurement of density. Nature 1960;186:956.

[101] Suzuki I, Kakimoto K, Oki S. Volumetric determination of adsorption of helium over some zeolites with a temperature-compensated, differential tensimeter having symmetrical design. Rev Sci Instrum 1987;58:1226–30. https://doi.org/10.1063/1.1139659.

[102] Steele WA, Halsey GD. The interaction of rare gas atoms with surfaces. J Chem Phys 1954;22:979–84. https://doi.org/10.1063/1.1740318.

[103] Malbrunot P, Vidal D, Vermesse J, Chahine R, Bose TK. Adsorbent helium density measurement and its effect on adsorption isotherms at high pressure. Langmuir 1997;13:539–44.

[104] Keller JU, Dreisbach F, Rave H, Staudt R, Tomalla M. Measurement of gas mixture adsorption equilibria of natural gas compounds on microporous sorbents. Adsorption 1999;5:199–214.

[105] Keller JU, Staudt R. Gas adsorption equilibria: experimental methods and adsorptive isotherms. Springer Science & Business Media; 2005.

[106] Kini KA, Stacy WO. The adsorption of helium by carbonaceous solids. Carbon N Y 1963;1:17–24. https://doi.org/10.1016/0008-6223(63)90005-8.

[107] Robens E, Keller JU, Massen CH, Staudt R. Sources of error in sorption and density measurements. J Therm Anal Calorim 1999;55:383–7.

[108] Lorenz K, Wessling M. How to determine the correct sample volume by gravimetric sorption measurements. Adsorption 2013;19:1117–25. https://doi.org/10.1007/s10450-013-9537-0.

[109] Wu K, Chen Z, Li X, Guo C, Wei M. A model for multiple transport mechanisms through nanopores of shale gas reservoirs with real gas effect–adsorption-mechanic coupling. Int J Heat Mass Transf 2016;93:408–26.

[110] Malbrunot P, Vidal D, Vermesse J, Chahine R, Bose TK. Adsorbent helium density measurement and its effect on adsorption isotherms at high pressure. Langmuir 1997;13:539–44. https://doi.org/10.1021/la950969e.

[111] Kaneko K, Cracknell RF, Nicholson D. Nitrogen Adsorption in Slit Pores at Ambient Temperatures: Comparison of Simulation and Experiment. Langmuir 1994;10:4606–9. https://doi.org/10.1021/la00024a036.

[112] Neimark A V., Ravikovitch PI. Calibration of pore volume in adsorption experiments and theoretical models. Langmuir 1997;13:5148–59.

[113] Do DD, Do HD, Wongkoblap A, Nicholson D. Henry constant and isosteric heat at zero-loading for gas adsorption in carbon nanotubes. Phys Chem Chem Phys 2008;10:7293–303. https://doi.org/10.1039/b809022j.

[114] Prasetyo L, Do D., Nicholson D. A coherent definition of henry constant and isosteric heat at zero loading for adsorption in solids - an absolute accessible volume. Chem Eng J 2018;8. https://doi.org/10.22201/fq.18708404e.2004.3.66178.

[115] Vasanth Kumar K, Rodríguez-Reinoso F. Co-adsorption of N2 in the presence of CH4 within carbon nanospaces: Evidence from molecular simulations. Nanotechnology 2013;24. https://doi.org/10.1088/0957-4484/24/3/035401.

[116] Wang T, Tian S, Li G, Sheng M, Ren W, Liu Q, et al. Molecular Simulation of CO2/CH4Competitive Adsorption on Shale Kerogen for CO2Sequestration and Enhanced Gas Recovery. J Phys Chem C 2018;122:17009–18. https://doi.org/10.1021/acs.jpcc.8b02061.

[117] Sui H, Yao J. Effect of surface chemistry for CH4/CO2 adsorption in kerogen: A molecular simulation study. J Nat Gas Sci Eng 2016;31:738–46. https://doi.org/10.1016/j.jngse.2016.03.097.

[118] Pang Y, He Y, Chen S. An innovative method to characterize sorption-induced kerogen swelling in organic-rich shales. Fuel 2019;254:115629. https://doi.org/10.1016/j.fuel.2019.115629.

[119] Cui X, Bustin RM. Volumetric strain associated with methane desorption and its impact on

coalbed gas production from deep coal seams. Am Assoc Pet Geol Bull 2005;89:1181–202. https://doi.org/10.1306/05110504114.

[120] Bustin RM, Cui X, Chikatamarla L. Impacts of volumetric strain on CO2 sequestration in coals and enhanced CH4 recovery. Am Assoc Pet Geol Bull 2008;92:15–29. https://doi.org/10.1306/08220706113.

[121] Heller R, Zoback M. Adsorption of methane and carbon dioxide on gas shale and pure mineral samples. J Unconv Oil Gas Resour 2014;8:14–24. https://doi.org/10.1016/j.juogr.2014.06.001.

[122] Levine JR. Model study of the influence of matrix shrinkage on absolute permeability of coal bed reservoirs. n.d.

[123] Pan Z, Connell LD. A theoretical model for gas adsorption-induced coal swelling. Int J Coal Geol 2007;69:243–52. https://doi.org/10.1016/j.coal.2006.04.006.

[124] Liu S, Harpalani S. A new theoretical approach to model sorption-induced coal shrinkage or swelling. Am Assoc Pet Geol Bull 2013;97:1033–49. https://doi.org/10.1306/12181212061.

[125] Henry W. III. Experiments on the quantity of gases absorbed by water, at different temperatures, and under different pressures. Philos Trans R Soc London 1803:29–274.

[126] Langmuir I. The adsorption of gases on plane surfaces of glass, mica and platinum. J Am Chem Soc 1918;40:1361–403.

[127] Brunauer S, Emmett PH, Teller E. Adsorption of gases in multimolecular layers. J Am

Chem Soc 1938;60:309–19.

[128] Dubinin Mm. The potential theory of adsorption of gases and vapors for adsorbents with energetically nonuniform surfaces. Chem Rev 1960;60:235–41.

[129] Dubinin MM. Modern state of the theory of gas and vapour adsorption by microporous adsorbents. Pure Appl Chem 1965;10:309–22.

[130] Sakurovs R, Day S, Weir S, Duffy G. Application of a modified Dubinin− Radushkevich equation to adsorption of gases by coals under supercritical conditions. Energy & Fuels 2007;21:992–7.

[131] Graham D. The characterization of physical adsorption systems. I. The equilibrium function and standard free energy of adsorption. J Phys Chem 1953;57:665–9.

[132] Mertens FO. Determination of absolute adsorption in highly ordered porous media. Surf Sci 2009;603:1979–84.

[133] Kozłowska A, Kozłowski R. Analysis of water adsorption by wood using the Guggenheim-Anderson-de Boer equation. Eur J Wood Wood Prod 2012;70:445–51.

[134] Dent RW. A multilayer theory for gas sorption: Part I: sorption of a single gas. Text Res J 1977;47:145–52.

[135] Zhou Y, Zhou L. Fundamentals of high pressure adsorption. Langmuir 2009;25:13461–6.

[136] Reich R, Ziegler WT, Rogers KA. Adsorption of methane, ethane, and ethylene gases and their binary and ternary mixtures and carbon dioxide on activated carbon at 212-301 K and pressures to 35 atmospheres. Ind Eng Chem Process Des Dev 1980;19:336–44.

[137] Jian X, Xiangjun L, Lixi L. Improved Dubibin-Astakhov model for shale-gas supercritical adsorption. ACTA Pet Sin 2015;35:849–57.

[138] Tang X, Ripepi N, Stadie NP, Yu L, Hall MR. A dual-site Langmuir equation for accurate estimation of high pressure deep shale gas resources. Fuel 2016;185:10–7.

[139] Day S, Sakurovs R, Weir S. Supercritical gas sorption on moist coals. Int J Coal Geol 2008;74:203–14.

[140] Metropolis N, Rosenbluth AW, Rosenbluth MN, Teller AH, Teller E. Equation of state calculations by fast computing machines. J Chem Phys 1953;21:1087–92. https://doi.org/10.1063/1.1699114.

[141] Hastings WK. Monte Carlo sampling methods using Markov chains and their applications 1970.

[142] Nicholson D. Computer simulation and the statistical mechanics of adsorption. Academic Press; 1982.

[143] Konstantakou M, Gotzias A, Kainourgiakis M, Stubos AK, Steriotis TA. GCMC simulations of gas adsorption in carbon pore structures. Appl. Monte Carlo Method Sci. Eng., IntechOpen; 2011.

[144] Smit B. Understanding molecular simulation: from algorithms to applications. Academic Press; 1996.

[145] Thijssen J. Computational physics. Cambridge university press; 2007.

[146] Eastwood JW, Hockney RW, Lawrence DN. P3M3DP-The three-dimensional periodic

particle-particle/particle-mesh program. Comput Phys Commun 1984;35.

[147] Berendsen HJC, Postma JP. M; DiNola, A.; Van Gunsteren, WF; Haak. J Chem Phys 1984;181:3684–90.

[148] Nosé S. An extension of the canonical ensemble molecular dynamics method. Mol Phys 1986;57:187–91.

[149] Hoover WG. Canonical dynamics: Equilibrium phase-space distributions. Phys Rev A 1985;31:1695.

[150] Plimpton S. Fast parallel algorithms for short-range molecular dynamics. J Comput Phys 1995;117:1–19.

[151] Humphrey W, Dalke A, Schulten K. VMD: visual molecular dynamics. J Mol Graph 1996;14:33–8.

[152] Stukowski A. Visualization and analysis of atomistic simulation data with OVITO–the Open Visualization Tool. Model Simul Mater Sci Eng 2009;18:15012.

[153] Gu S, Gao B, Teng L, Li Y, Fan C, Iglauer S, et al. Monte Carlo Simulation of Supercritical Carbon Dioxide Adsorption in Carbon Slit Pores. Energy and Fuels 2017;31:9717–24. https://doi.org/10.1021/acs.energyfuels.7b01344.

[154] Lin K, Yuan Q, Zhao YP. Using graphene to simplify the adsorption of methane on shale in MD simulations. Comput Mater Sci 2017;133:99–107. https://doi.org/10.1016/j.commatsci.2017.03.010.

[155] Striolo A, Chialvo AA, Cummings PT, Gubbins KE. Water adsorption in carbon-slit

nanopores. Langmuir 2003;19:8583–91. https://doi.org/10.1021/la0347354.

[156] Yu X, Li J, Chen Z, Wu K, Zhang L, Yang S. Effects of helium adsorption in carbon nanopores on apparent void volumes and excess methane adsorption isotherms. Fuel 2020;270:117499. https://doi.org/10.1016/j.fuel.2020.117499.

[157] Zhang J, Liu K, Clennell MB, Dewhurst DN, Pervukhina M. Molecular simulation of CO2-CH4 competitive adsorption and induced coal swelling. Fuel 2015;160:309–17. https://doi.org/10.1016/j.fuel.2015.07.092.

[158] Stevar MSP, Böhm C, Notarki KT, Trusler JPM. Wettability of calcite under carbon storage conditions. Int J Greenh Gas Control 2019;84:180–9.

[159] Al-Yaseri AZ, Lebedev M, Barifcani A, Iglauer S. Receding and advancing (CO2+ brine+ quartz) contact angles as a function of pressure, temperature, surface roughness, salt type and salinity. J Chem Thermodyn 2016;93:416–23.

[160] Dauber-Osguthorpe P, Roberts VA, Osguthorpe DJ, Wolff J, Genest M, Hagler AT. Structure and energetics of ligand binding to proteins: Escherichia coli dihydrofolate reductase-trimethoprim, a drug-receptor system. Proteins Struct Funct Bioinforma 1988;4:31–47.

[161] Yuan Q, Zhu X, Lin K, Zhao YP. Molecular dynamics simulations of the enhanced recovery of confined methane with carbon dioxide. Phys Chem Chem Phys 2015;17:31887–93. https://doi.org/10.1039/c5cp06649b.

[162] De Lara LS, Rigo VA, Michelon MF, Metin CO, Nguyen QP, Miranda CR. Molecular

dynamics studies of aqueous silica nanoparticle dispersions: Salt effects on the double layer formation. J Phys Condens Matter 2015;27:325101.

[163] Iglauer S, Mathew MS, Bresme F. Molecular dynamics computations of brine-CO2 interfacial tensions and brine-CO2-quartz contact angles and their effects on structural and residual trapping mechanisms in carbon geo-sequestration. J Colloid Interface Sci 2012;386:405–14. https://doi.org/10.1016/j.jcis.2012.06.052.

[164] Boinovich L, Emelyanenko A. Wetting and surface forces. Adv Colloid Interface Sci 2011;165:60–9.

[165] Rafiee J, Mi X, Gullapalli H, Thomas A V, Yavari F, Shi Y, et al. Wetting transparency of graphene. Nat Mater 2012;11:217–22.

[166] Bresme F, Quirke N. Computer simulation study of the wetting behavior and line tensions of nanometer size particulates at a liquid-vapor interface. Phys Rev Lett 1998;80:3791–4. https://doi.org/10.1103/PhysRevLett.80.3791.

[167] Bresme F, Oettel M. Nanoparticles at fluid interfaces. J Phys Condens Matter 2007;19:413101.

[168] Bresme F, Quirke N. Computer simulation studies of liquid lenses at a liquid–liquid interface. J Chem Phys 2000;112:5985–90.

[169] Li H, Zeng XC. Wetting and interfacial properties of water nanodroplets in contact with graphene and monolayer boron–nitride sheets. ACS Nano 2012;6:2401–9.

[170] Shih C-J, Wang QH, Lin S, Park K-C, Jin Z, Strano MS, et al. Breakdown in the wetting

transparency of graphene. Phys Rev Lett 2012;109:176101.

[171] Taherian F, Marcon V, F. A. van der Vegt N, Leroy F. What Is the Contact Angle of Water on Graphene? Langmuir 2013;29:1457–65. https://doi.org/10.1021/la304645w.

[172] Fanchi JR. Principles of applied reservoir simulation. Elsevier; 2005.

[173] Li H, Cheng Zeng X. Wetting and Interfacial Properties of Water Nanodroplets in Contact with Graphene and Monolayer Boron–Nitride Sheets. ACS Nano 2012;6:2401–9. https://doi.org/10.1021/nn204661d.

[174] Yang D, Gu Y, Tontiwachwuthikul P. Wettability determination of the reservoir brine− reservoir rock system with dissolution of CO2 at high pressures and elevated temperatures. Energy & Fuels 2008;22:504–9.

[175] Hu Y, Devegowda D, Sigal R. A microscopic characterization of wettability in shale kerogen with varying maturity levels. J Nat Gas Sci Eng 2016;33:1078–86. https://doi.org/10.1016/J.JNGSE.2016.06.014.

[176] Saraji S, Goual L, Piri M, Plancher H. Wettability of supercritical carbon dioxide/water/quartz systems: Simultaneous measurement of contact angle and interfacial tension at reservoir conditions. Langmuir 2013;29:6856–66.

[177] Chiquet P, Broseta D, Thibeau S. Wettability alteration of caprock minerals by carbon dioxide. Geofluids 2007;7:112–22. https://doi.org/10.1111/j.1468-8123.2007.00168.x.

[178] Huang L, Ning Z, Wang Q, Zhang W, Cheng Z, Wu X, et al. Effect of organic type and moisture on CO2/CH4competitive adsorption in kerogen with implications for

CO2sequestration and enhanced CH4recovery. Appl Energy 2018;210:28–43. https://doi.org/10.1016/j.apenergy.2017.10.122.

[179] Jung J-W, Wan J. Supercritical CO2 and ionic strength effects on wettability of silica surfaces: Equilibrium contact angle measurements. Energy & Fuels 2012;26:6053–9.

[180] Espinoza DN, Santamarina JC. Water-CO2-mineral systems: Interfacial tension, contact angle, and diffusionImplications to CO2 geological storage. Water Resour Res 2010;46:1–10. https://doi.org/10.1029/2009WR008634.

[181] Vane LM, Zang GM. Effect of aqueous phase properties on clay particle zeta potential and electro-osmotic permeability: Implications for electro-kinetic soil remediation processes. J Hazard Mater 1997;55:1–22.

[182] Alroudhan A, Vinogradov J, Jackson MD. Zeta potential of intact natural limestone: Impact of potential-determining ions Ca, Mg and SO4. Colloids Surfaces A Physicochem Eng Asp 2016;493:83–98.

[183] Saraji S, Goual L, Piri M. Dynamic adsorption of asphaltenes on quartz and calcite packs in the presence of brine films. Colloids Surfaces A Physicochem Eng Asp 2013;434:260–7.

[184] Kasha A, Al-Hashim H, Abdallah W, Taherian R, Sauerer B. Effect of Ca2+, Mg2+ and SO42− ions on the zeta potential of calcite and dolomite particles aged with stearic acid. Colloids Surfaces A Physicochem Eng Asp 2015;482:290–9.

[185] Roshan H, Andersen MS, Rutlidge H, Marjo CE, Acworth RI. Investigation of the kinetics

of water uptake into partially saturated shales. Water Resour Res 2016;52:2420–38.

[186] Mugele F, Siretanu I, Kumar N, Bera B, Wang L, de Ruiter R, et al. Insights from ion adsorption and contact-angle alteration at mineral surfaces for low-salinity waterflooding. SPE J 2016;21:1–204.

[187] Arif M, Abu-Khamsin S, Iglauer S. Wettability of rock/CO2/brine and rock/oil/CO2-enriched-brine systems: Critical parametric analysis and future outlook. Adv Colloid Interface Sci 2019.

[188] Chen C, Chai Z, Shen W, Li W, Song Y. Wettability of supercritical CO2–brine–mineral: The effects of ion type and salinity. Energy & Fuels 2017;31:7317–24.

[189] d'Oliveira HD, Davoy X, Arche E, Malfreyt P, Ghoufi A. Test-area surface tension calculation of the graphene-methane interface: Fluctuations and commensurability. J Chem Phys 2017;146:214112.

[190] Arif M, Barifcani A, Lebedev M, Iglauer S. Impact of Solid Surface Energy on Wettability of CO2-brine-Mineral Systems as a Function of Pressure, Temperature and Salinity. Energy Procedia 2017;114:4832–42.

[191] Arif M, Barifcani A, Lebedev M, Iglauer S. CO2-wettability of low to high rank coal seams: Implications for carbon sequestration and enhanced methane recovery. Fuel 2016;181:680–9. https://doi.org/10.1016/j.fuel.2016.05.053.

[192] Guan C, Liu S, Li C, Wang Y, Zhao Y. The temperature effect on the methane and CO2 adsorption capacities of Illinois coal. Fuel 2018;211:241–50.

[193] Collell J, Galliero G, Vermorel R, Ungerer P, Yiannourakou M, Montel F, et al. Transport of multicomponent hydrocarbon mixtures in shale organic matter by molecular simulations. J Phys Chem C 2015;119:22587–95.

[194] Wu K, Li X, Wang C, Yu W, Chen Z. Model for surface diffusion of adsorbed gas in nanopores of shale gas reservoirs. Ind Eng Chem Res 2015;54:3225–36.

[195] Tian Y, Yan C, Jin Z. Characterization of methane excess and absolute adsorption in various clay nanopores from molecular simulation. Sci Rep 2017;7:12040.

[196] Zhang T, Ellis GS, Ruppel SC, Milliken K, Yang R. Effect of organic-matter type and thermal maturity on methane adsorption in shale-gas systems. Org Geochem 2012;47:120–31. https://doi.org/10.1016/j.orggeochem.2012.03.012.

[197] Sarkisov L, Harrison A. Computational structure characterisation tools in application to ordered and disordered porous materials. Mol Simul 2011;37:1248–57.

[198] Zhao D, Guo Y, Wang G, Mao X. Characterizing nanoscale pores and its structure in coal: Experimental investigation. Energy Explor Exploit 2019:0144598719831397.

[199] Jin Z, Firoozabadi A. Flow of methane in shale nanopores at low and high pressure by molecular dynamics simulations. J Chem Phys 2015;143. https://doi.org/10.1063/1.4930006.

[200] Hirschfelder JO, Curtiss CF, Bird RB, Mayer MG. Molecular theory of gases and liquids. vol. 26. Wiley New York; 1954.

[201] Chen G, Lu S, Zhang J, Xue Q, Han T, Xue H, et al. Keys to linking GCMC simulations

and shale gas adsorption experiments. Fuel 2017;199:14–21. https://doi.org/10.1016/j.fuel.2017.02.063.

[202] Kazemi M, Takbiri-Borujeni A. Flow of gases in slit shaped organic nanopores of shale: A boundary-driven molecular simulation study. SPE Low Perm Symp., Society of Petroleum Engineers; 2016.

[203] Pan H, Ritter JA, Balbuena PB. Examination of the approximations used in determining the isosteric heat of adsorption from the Clausius− Clapeyron equation. Langmuir 1998;14:6323–7.

[204] Abraham FF, Singh Y. The structure of a hard-sphere fluid in contact with a soft repulsive wall. J Chem Phys 1977;67:2384–5.

[205] Steele WA. The interaction of rare gas atoms with graphitized carbon black. J Phys Chem 1978;82:817–21.

[206] Sarkisov L, Harrison A. Computational structure characterisation tools in application to ordered and disordered porous materials. Mol Simul 2011;37:1248–57. https://doi.org/10.1080/08927022.2011.592832.

[207] Li J, Li X, Wu K, Feng D, Zhang T, Zhang Y. Thickness and stability of water film confined inside nanoslits and nanocapillaries of shale and clay. Int J Coal Geol 2017;179:253–68. https://doi.org/10.1016/j.coal.2017.06.008.

[208] Bu H, Ju Y, Tan J, Wang G, Li X. Fractal characteristics of pores in non-marine shales from the Huainan coalfield, eastern China. J Nat Gas Sci Eng 2015;24:166–77.

https://doi.org/10.1016/j.jngse.2015.03.021.

[209] Song X, Chen JK. A comparative study on poiseuille flow of simple fluids through cylindrical and slit-like nanochannels. Int J Heat Mass Transf 2008;51:1770–9. https://doi.org/10.1016/j.ijheatmasstransfer.2007.07.019.

[210] Mosher K, He J, Liu Y, Rupp E, Wilcox J. Molecular simulation of methane adsorption in micro- and mesoporous carbons with applications to coal and gas shale systems. Int J Coal Geol 2013;109–110:36–44. https://doi.org/10.1016/j.coal.2013.01.001.

[211] Ottiger S, Pini R, Storti G, Mazzotti M, Bencini R, Quattrocchi F, et al. Adsorption of pure carbon dioxide and methane on dry coal from the Sulcis Coal Province (SW Sardinia, Italy). Environ Prog 2006;25:355–64.

[212] Ungerer P, Collell J, Yiannourakou M. Molecular Modeling of the Volumetric and Thermodynamic Properties of Kerogen: Influence of Organic Type and Maturity. Energy & Fuels 2014;29:91–105. https://doi.org/10.1021/ef502154k.

[213] R. Kelemen S, Afeworki M, L. Gorbaty M, Sansone M, J. Kwiatek P, C. Walters C, et al. Direct Characterization of Kerogen by X-ray and Solid-State 13C Nuclear Magnetic Resonance Methods. Energy & Fuels 2007;21:1548–61. https://doi.org/10.1021/ef060321h.

[214] Stankiewicz A, Ionkina N, Motherwell B, Bennett B, Wint O, Mastalerz M. Kerogen Density Revisited—Lessons From the Duvernay Shale. Proc. 3rd Unconv. Resour. Technol. Conf., Tulsa, OK, USA: American Association of Petroleum Geologists; 2015.

https://doi.org/10.15530/urtec-2015-2157904.

[215] Pisarev V V., Zakharov SA. Comparison of forcefields for molecular dynamics simulations of hydrocarbon phase diagrams. J Phys Conf Ser 2018;946:0–6. https://doi.org/10.1088/1742-6596/946/1/012100.

[216] G. Martin M, Ilja Siepmann J. Transferable Potentials for Phase Equilibria. 1. United-Atom Description of n-Alkanes. J Phys Chem B 1998;102:2569–77. https://doi.org/10.1021/jp972543+.

[217] Chen B, Siepmann JI. Transferable Potentials for Phase Equilibria. 3. Explicit-Hydrogen Description of Normal Alkanes. J Phys Chem B 2002;103:5370–9. https://doi.org/10.1021/jp990822m.

[218] Potoff JJ, Siepmann JI. Vapor-liquid equilibria of mixtures containing alkanes, carbon dioxide, and nitrogen. AIChE J 2001;47:1676–82. https://doi.org/10.1002/aic.690470719.

[219] Yu X, Li J, Chen Z, Wu K, Zhang L. Effects of an adsorbent accessible volume on methane adsorption on shale. Comput Methods Appl Mech Eng 2020;370:113222. https://doi.org/10.1016/j.cma.2020.113222.

[220] Do DD, Do HD, Fan C, Nicholson D. On the existence of negative excess isotherms for argon adsorption on graphite surfaces and in graphitic pores under supercritical conditions at pressures up to 10,000 atm. Langmuir 2010;26:4796–806.

[221] Herrera L, Do DD, Nicholson D. A Monte Carlo integration method to determine accessible volume, accessible surface area and its fractal dimension. J Colloid Interface Sci

2010;348:529–36. https://doi.org/10.1016/j.jcis.2010.05.001.

[222] Barnett M, Units D, Chalmers GR, Bustin RM, Power IM, Sciences O. Characterization of gas shale pore systems by porosimetry, pycnometry, surface area, and field emission scanning electron microscopy/transmission electron microscopy image analyses: Examples from the. Am Assoc Pet Geol Bull 2012;96:1099. https://doi.org/10.1306/10171111052.

[223] Ho TA, Criscenti LJ, Wang Y. Nanostructural control of methane release in kerogen and its implications to wellbore production decline. Sci Rep 2016;6:1–9. https://doi.org/10.1038/srep28053.

[224] Wang S, Feng Q, Javadpour F, Hu Q, Wu K. Competitive adsorption of methane and ethane in montmorillonite nanopores of shale at supercritical conditions: A grand canonical Monte Carlo simulation study. Chem Eng J 2019;355:76–90. https://doi.org/10.1016/j.cej.2018.08.067.

[225] Collell J, Galliero G, Gouth F, Montel F, Pujol M, Ungerer P, et al. Molecular simulation and modelisation of methane/ethane mixtures adsorption onto a microporous molecular model of kerogen under typical reservoir conditions. Microporous Mesoporous Mater 2014;197:194–203. https://doi.org/10.1016/j.micromeso.2014.06.016.

[226] Battistutta E, van Hemert P, Lutynski M, Bruining H, Wolf KH. Swelling and sorption experiments on methane, nitrogen and carbon dioxide on dry Selar Cornish coal. Int J Coal Geol 2010;84:39–48. https://doi.org/10.1016/j.coal.2010.08.002.

[227] Brochard L, Vandamme M, Pellenq RJM, Fen-Chong T. Adsorption-induced deformation

of microporous materials: Coal swelling induced by CO 2-CH 4 competitive adsorption. Langmuir 2012;28:2659–70. https://doi.org/10.1021/la204072d.

[228] Wang GX, Wei XR, Wang K, Massarotto P, Rudolph V. Sorption-induced swelling/shrinkage and permeability of coal under stressed adsorption/desorption conditions. Int J Coal Geol 2010;83:46–54.

[229] Siriwardane HJ, Gondle RK, Smith DH. Shrinkage and swelling of coal induced by desorption and sorption of fluids: Theoretical model and interpretation of a field project. Int J Coal Geol 2009;77:188–202.

[230] Pekot LJ, Reeves SR. Matrix shrinkage and permeability reduction with carbon dioxide injection. Coal-Seq II Forum, Washingt. D. C, 2003.

[231] Liu S, Harpalani S. Compressibility of sorptive porous media: Part 2. Experimental study on coalCompressibility of Sorptive Material, Experimental Study. Am Assoc Pet Geol Bull 2014;98:1773–88.

[232] Kang SM, Fathi E, Ambrose RJ, Akkutlu IY, Sigal RF. Carbon dioxide storage capacity of organic-rich shales. Spe J 2011;16:842–55.

Appendix A. Model validation for gas adsorption in kerogens

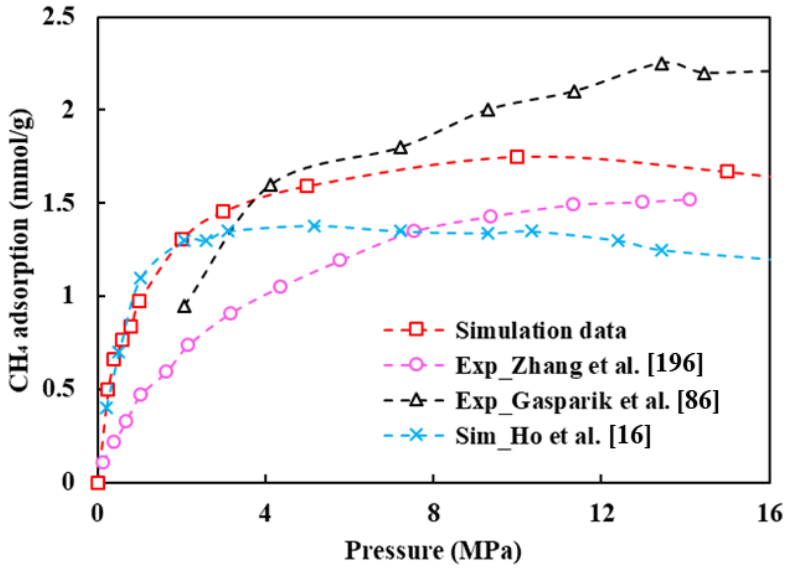

Figure A 1 Comparison of CH_4 excess adsorption isotherms with data from the literature [16,86,196]**.**

The experimental data used for comparing our simulation data is CH_4 adsorption isotherms for the organic-rich Barnett shale measured by Zhang et al. and Gasparik et al., which is normalized by TOC [86,196]. The simulation data used for model validation was obtained by Ho et al. [16] for CH_4 adsorption on kerogen at 338 K. Overall, our simulation data is of great reasonability compared with experimental and simulation data from the literature.

Appendix B. Pore size distribution of the initial kerogen model

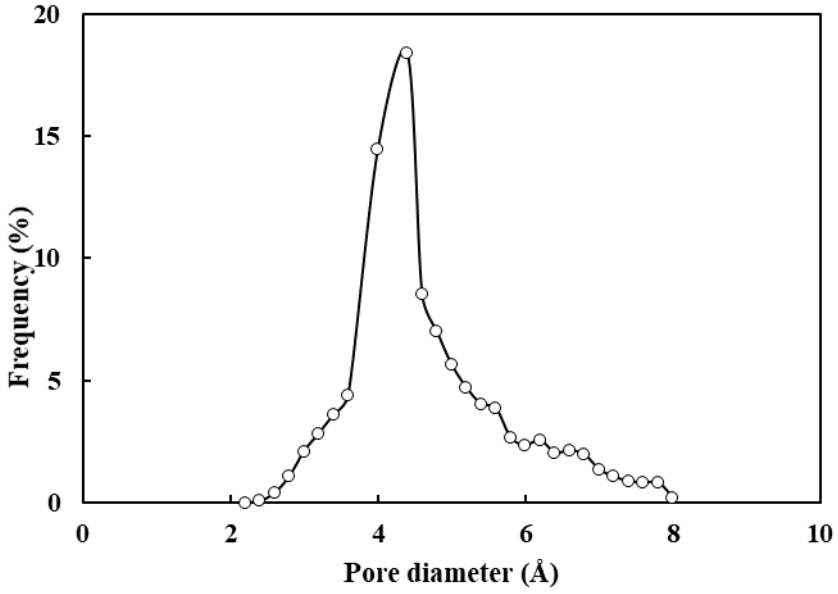

Figure B 1 Pore size distribution of the initial kerogen model.

Figure B1 displays a pore size distribution of the initial kerogen model determined by a helium probe. The pore size ranges from 2 to 8 Å and the highest frequency can be observed for pores with a diameter of around 4.3 Å. As pores in the built kerogen model are extremely small, the total loading amount of an adsorbent in the kerogen model can be regarded as an absolute adsorbed amount.

Appendix C. Normalization of a linear relationship between bulk volumetric strain and absolute adsorption amount

The coefficient α is associated with the size of gas molecules and it can be written as a function of a kinetic diameter of a molecule:

$$\alpha = kD^n \tag{C1}$$

where k is only dependent on the adsorbent and n is a constant. These two parameters can be determined by plotting lnα against ln$D$ **(Figure C1)**.

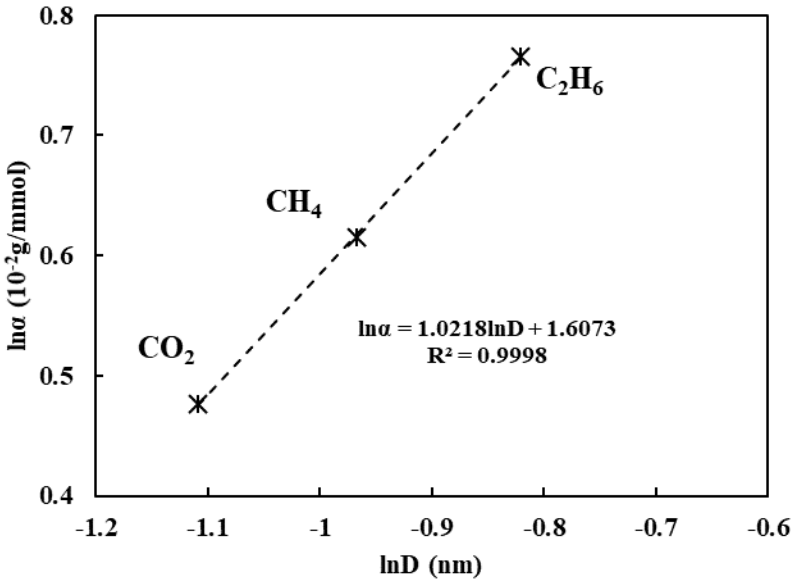

Figure C 1 Plot of coefficient and kinetic diameter of different adsorbates for determination of *n* and *k* (*n*=1.02, *k*=4.9).

Then equation (8.5) can be written as

$$\varepsilon_b = kD^n N_{ab} \tag{C2}$$

To normalize the linear relationships for different adsorbates between the bulk volumetric strain and the absolute adsorption amount, we divide both sides of equation (C2) by D^n and a unified model can be obtained:

$$\frac{\varepsilon_b}{D^n} = kN_{ab} \tag{C3}$$